DECLARATION

The author hereby declares that this thesis represents work which has been carried out by her and that it has not been submitted to any other University or Institution for the award of any Degree, Diploma, Associateship, Fellowship or any other such title.

Place: Talcigao Plateau.
Date : April 27, 2007

Ms. Preeti A. Bhobe

CERTIFICATE

We hereby certify that the above Declaration of the candidate Ms. Preeti A. Bhobe is true and that this thesis represents her independent work.

Professor P. R. Sarode
Department of Physics
Goa University, Goa

Dr. K. R. Priolkar
Department of Physics
Goa University, Goa

EXAMINED

27/11/07

S. K. Kulkarni
27/11/07

27/11/2007

.....To my Parents

Acknowledgements

It is indeed a privilege to thank all those involved directly or indirectly and contributed to the success of this work.

I wish to express my sincere thanks to my supervisors: I thank Professor P. R. Sarode, Department of Physics, Goa University for the guidance and the freedom to work in my own way.

I am very indebted to Dr. Kaustubh R. S. Priolkar for bringing the best in me. For giving me the encouragement and vision and teaching me the finer nuances of academia and research. A fine teacher and a great friend like him are indeed rare to find.

Financial assistance from UGC-DAE Consortium for Scientific Research (formerly IUC-DAEF) Mumbai centre through Project Assistantship and Council for Scientific and Industrial Research (CSIR), New Delhi, through Senior Research Fellowship is gratefully acknowledged.

Role of Department of Science and Technology (DST) New Delhi, and ICTP in making available Synchrotron facility at ELETTRA, Trieste Italy and financial assistance for travel and stay at Italy are gratefully acknowledged.

Grazie mille to Professor G. Vliac and Dr. Luca Olivi, ELETTRA, Italy, for their kind suggestions in carrying out the EXAFS measurements.

I am grateful to Professor N. Gajbhiye, Department of Chemistry, Indian Institute of Technology (IIT), Kanpur, for extending the facility for magnetization studies. My special thanks go to Mr. Sachil Sharma for carrying out the measurements.

I acknowledge Soild State and Structural Chemistry Unit, Indian Institute of Science (SSCU-IISc), Bangalore, for carrying out the EDX experiments.

Muito Obrigada to Professor S. K. Mendiratta and his group at the University of Averio, Averio, Portugal, for making available a.c. susceptibility, optical microscopy and SEM facility.

Profuse thanks are due to Professor J. A. E. Desa, Dr. Ramesh Pai and the other members of teaching faculty at Department of Physics, Goa University for their valuable feedback throughout my research work. I am also grateful to my colleagues, Dr. J. B. C. Efrem D'Sa, Dr. Aditi Gandhe, Ms. Miskil Naik, Ms. Swati Pawar and Mr. Ramu Murthy for their company and support.

A note of thanks to the technical and administrative staff of Physics Department, Goa University and Mr. Dayanand Shettigar for their cooperation during the tenure of my research

It is indeed a pleasure to mention my friends, Anwesha, Joly, Qureshi, Srikiran, Raksha, Meena and Ajay whose support is deeply appreciated. My hostel friends Rama, Prapti, Beena, Radhika, Rachel, Deepti and Reshma who have entertained over the years at the University hostel and whose company will always bring pleasant memories.

I owe a debt of gratitude to my parents whose love, motivation and support has helped me thrive in thought and action and to my sister who has always been there for me.

27 April 2007 Preeti Bhobe

Contents

List of Tables

List of Figures

Chapter 1

Shape Memory Alloys

Shape Memory Alloys (SMAs, also known as memory metal) are a unique class of metallic materials that "remembers" its geometry and has the ability to return to some previously defined shape or size when subjected to the appropriate thermal procedure. Generally, these materials can be plastically deformed at some relatively low temperature, and upon exposure to some higher temperature will return to their shape prior to the deformation. Materials that exhibit shape memory only upon heating are referred to as having a one-way shape memory. Some materials also undergo a change in shape upon re-cooling. These materials are said to have a two-way shape memory. The key effects of SMAs are *pseudoelasticity* and *shape memory effect.*

These extraordinary properties are due to a temperature-dependent phase transformation from a highly symmetric crystallographic structure to a low-symmetry structure. These crystal structures are known as *Austenite* and *Martensite* respectively, and the solid state phase change that occurs through the molecular rearrangement is known as *Martensitic Transformation.*

1.1 Overview

A general understanding and simplistic description of the phenomena related to SMAs is presented here. More detailed information is available at [1] and [2, 3, 4]. The first recorded observation of the shape memory transformation was by Chang and Read in 1932 [5]. They noted the reversibility of the transformation in AuCd by metallographic observations and resistivity changes, and in 1951 the shape memory effect (SME) was observed in a bent bar of AuCd. In 1938, the transformation was seen in brass (CuZn). However, it was not until 1962, when Buehler and co-workers [6] discovered the effect in equiatomic nickel-titanium (NiTi), that research into both the metallurgy and potential practical uses began in earnest.

As the shape memory effect became better understood, a number of other alloy systems that exhibited shape memory were investigated. Of all the systems discovered, the NiTi alloys and a few of the copper-base alloys (like CuZnAl, CuAlNi) have received the most development effort and commercial exploitation.

Exactly what makes these metals "remember" their original shape is the structural change at the atomic level which occurs between the two crystallographic phases upon heating/cooling. The molecular rearrangement that occurs through a solid-solid phase change is the key effect associated with the unique properties these SMA possess.

The two phases which occur in shape memory alloys are **Austenite** and **Martensite**. Austenite, the stronger phase of shape memory alloys, occurs at higher temperatures. The shape of the Austenite structure is cubic, schematics of the structure is shown in Fig. 1.1(a). Martensite, is the relatively soft and easily deformed phase of shape memory alloys, which exists at lower temperatures. The molecular structure in this phase is twinned which is the

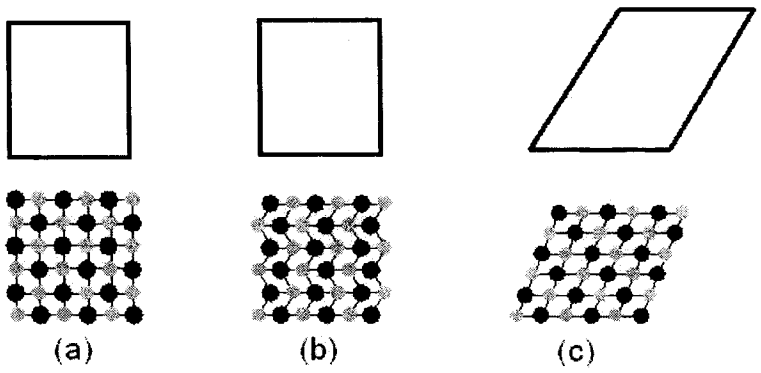

Figure 1.1: Schematics of different structural phases of a shape memory alloy.

configuration shown in Fig. 1.1(b). Upon deformation, this phase takes on the second form shown at Fig. 1.1(c). The un-deformed Martensite phase is the same size and shape as the cubic Austenite phase on a macroscopic scale, so that no change in size or shape is visible in shape memory alloys until the Martensite is deformed. The temperatures at which each of these phases begin and finish forming are represented as M_s - martensitic start, M_f - martensitic finish, A_s - austenitic start, and A_f - austenitic finish. The shape memory effect is observed when the temperature of a piece of shape memory alloy is cooled to below the temperature M_f. At this stage the alloy is completely composed of Martensite, which can be easily deformed. The original shape can be recovered simply by heating the sample above the temperature A_f. The deformed Martensite is now transformed to the cubic Austenite phase, which is configured to its original shape. The heat transferred to the sample is the power driving the molecular rearrangement of the alloy, similar to heat melting ice into water, but the alloy remains solid. This effect is shown in Fig. 1.2.

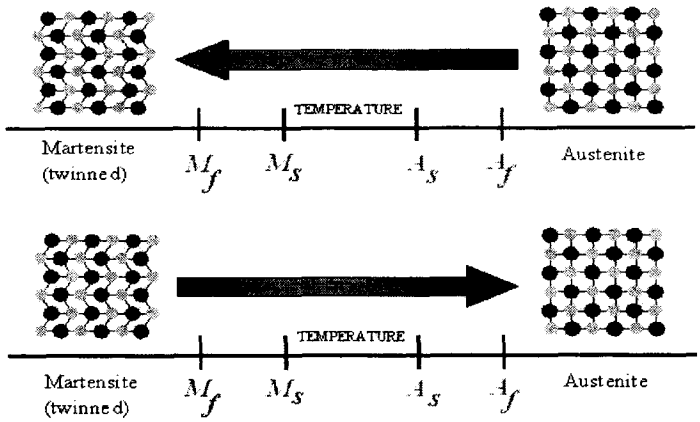

Figure 1.2: Temperature-induced phase transformation of an SMA without mechanical loading.

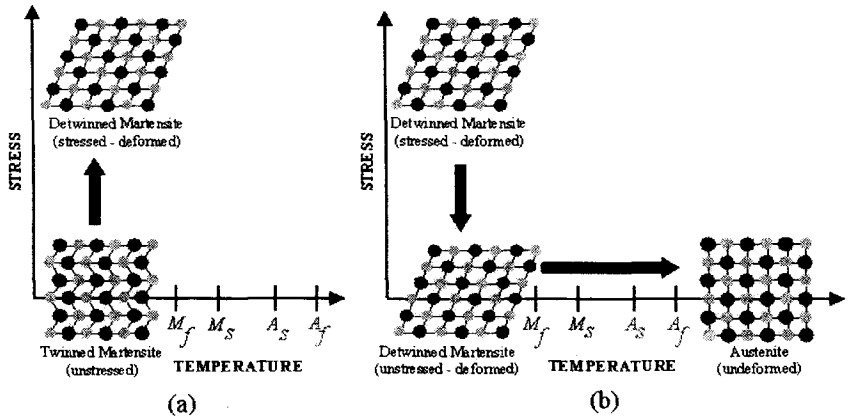

Figure 1.3: Shape Memory Effect of an SMA.

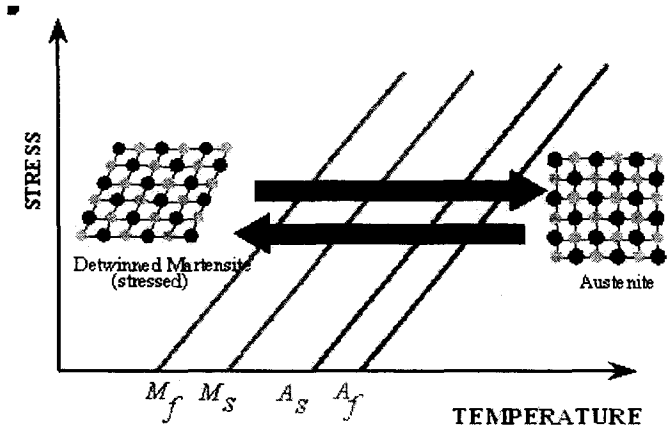

Figure 1.4: Temperature-induced phase transformation with applied load.

1.1.1 Shape Memory Effect

If mechanical load is applied to the material in the state of twinned martensite (at low temperature) it is possible to detwin the martensite. Upon releasing of the load, the material remains deformed. A subsequent heating of the material to a temperature above A_f will result in reverse phase transformation (martensite to austenite) and will lead to complete shape recovery, as shown in Fig. 1.3. The above described process results in manifestation of the *Shape Memory Effect (SME).*

It is also possible to induce a martensitic transformation which would lead directly to detwinned martensite. If load is applied in the austenitic phase and the material is cooled, the phase transformation will result in detwinned martensite. Thus, very large strains (on the order of 5 - 8%) will be observed. Reheating the material will result in complete shape recovery. The above-described loading path is shown in Fig. 1.4. The transformation temperatures in this case strongly depend on the magnitude of the applied load. Higher values of the applied load will lead to higher values of the transformation temperatures. Usually a linear relationship between the applied load and the transformation temperatures is assumed, as shown in Fig. 1.4.

1.1.2 Pseudoelastic Effect

It is also possible to induce a phase transformation by applying a pure mechanical load. The result of this load application is fully detwinned martensite with very large strains. If the temperature of the material is above A_f, a complete shape recovery is observed upon unloading, thus, the material behaviour resembles elasticity. Hence, the above-described effect is known under the name of *Pseudoelastic Effect.* A loading path demonstrating the

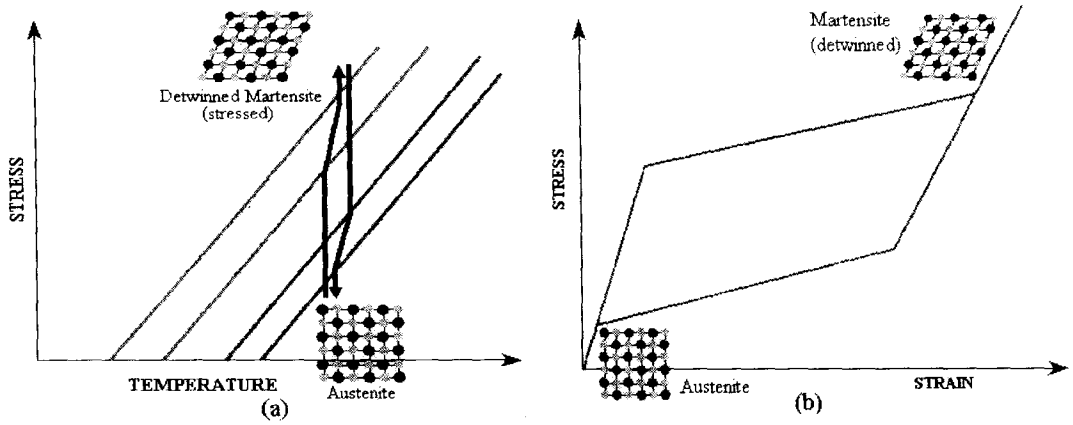

Figure 1.5: (a) Pseudoelastic loading path. (b)Pseudoelastic stress-strain diagram.

pseudoelastic effect is schematically shown in Fig. 1.5(a), while the resulting stress-strain diagram is shown in Fig. 1.5(b)

A shape memory alloy may be further defined as one that yields a thermoelastic martensite. In this case, the alloy undergoes a martensitic transformation of a type that allows the alloy to be deformed by a twinning mechanism below the transformation temperature. The deformation is then reversed when the twinned structure reverts upon heating to the parent phase. Thus, shape memory alloys are a special class of adaptive materials that can convert thermal energy directly into mechanical work and recover apparent permanent strains when heated above a certain temperature.

1.1.3 The Martensitic Transformation

The word "martensite" stands for the microstructure component in steel, developed upon quenching. It comes from the famous German metallurgist Adolf MARTENS and illustrates an interesting historic aspect associated with it.

As it is well known in today's world, when the steel is subjected to a quenching from

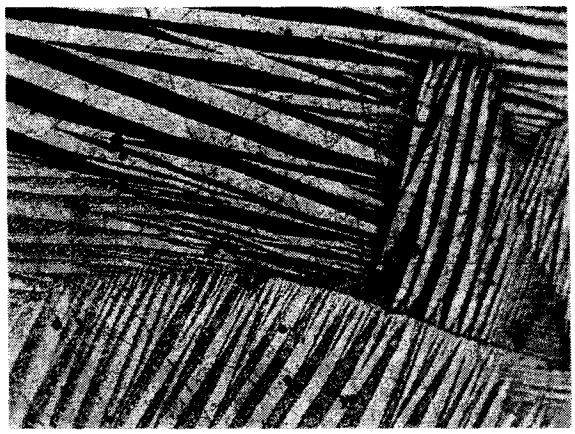

Figure 1.6: Variety of patterns developed on the surface of an alloy due to the microstructure formed upon martensitic phase change.

the high temperature phase (austenite), it traps carbon atoms within the cubic iron matrix distorting it into a body centered tetragonal structure and its hardness increases. However, during the early periods of civilization, a vast and drastic change occurred when steel replaced bronze. Yet, it was entirely unknown what gave steel its valuable properties, and for centuries the techniques for making high quality steel were closely held. Clearly, iron was its major component, but a myriad of other minor additions were found empirically, and mysterious treatments were evolved for cooling the red hot object to room temperature. In the 19th century there were great advances in chemical analysis, and it was conjectured that the reasons why steels were different would soon be known through determination of differences in chemical composition. However, it was often found that various steel alloys with very similar compositions could have vastly dissimilar mechanical properties. Over the same period, Adolf Martens examined the microstructure of steel under a microscope and found many varieties of patterns at the micron scale (see Fig. 1.6). In particular, hard steels were found to have banded regions of differently oriented, fascinating microcrystalline phases,

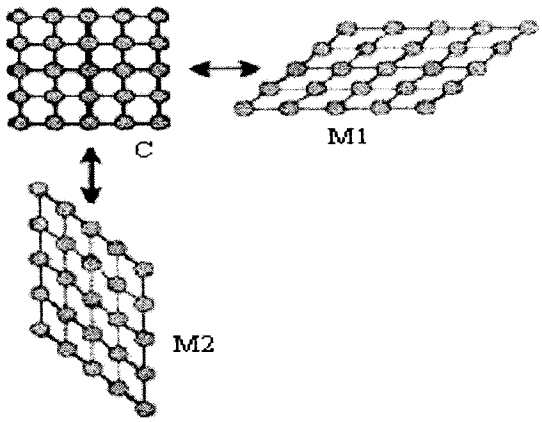

Figure 1.7: A sketch of martensitic transformation from a square lattice C to two variants $M1$ and $M2$ which differ only in orientation.

whereas inferior steels had little coherent pattering. The characteristic patterned regions became known as after their discoverer.

While metallurgists have a precise definition of a martensitic transformation (MT), physicists use the term more loosely to define many first-order transitions with acoustic anomalies. Both disciplines generally agree that they are purely structural, solid-solid phase transformation without any diffusion (the atoms do not move). Thus there is no change in the chemical formation of the material. There is a coordinated displacement of the atoms over distances much less than the atomic spacing, thus the transformation is displacive in nature. The process implies a bending of the crystalline network that leads to a macroscopic change. What this means, is illustrated by a simple sketch.

Consider in Fig. 1.7 a quadratic array of atoms C. For some reason this array becomes unstable and distorts to the lattice $M1$. The distortion shown is large, but the area of the array can remain the same. It is a homogeneous distortion of the original lattice in which an atom does not change its position with respect to its neighbors, it only alters their distances.

This is characteristic of diffusionless transformations with large shape changes. Because the original lattice of Fig. 1.7 has quadratic symmetry, an equivalent distortion leads to $M2$ in the figure, the only difference being the orientation in space. Suppose now that the stability of the lattices depends on a thermodynamic variable, for example the temperature: at the higher temperature the square lattice may be stable but on cooling it flips over to the new structure at a critical temperature. But since, in our case, two different variants of the same structure are possible, the resulting configuration consists of a mixture of both.

In a large piece of lattice it is not possible to have all material transformed simultaneously, instead the new structure nucleates first locally in some region in the interior of the array and then grows. It starts at a temperature M_s, called the martensitic start temperature. Since the two variants $M1$ and $M2$ of the Fig. 1.7 are equivalent energetically, they form with the same probability and start to present obstacles mutually for further growth. This results in a twinned structure on a mesoscopic scale. In order to continue growing the driving force has to be increased, which means a further cooling. For this reason the fraction that has transformed increases only with decreasing temperature, and is completed at the finish temperature M_f. On reheating the retransformation occurs, starting at A_s and being completed at A_f. Generally there is a displacement with respect to the cooling curve. This hysteresis can be quite large. Since no atom redistributions occur, diffusional processes that are time dependent are absent. Therefore the martensitic transformation is temperature, but not time dependent.

It seems reasonable to expect that the change from C to $M1$ in Fig. 1.7 can be aided by applying a force which helps to stretch the initial lattice in diagonal direction from the

lower left to the upper right. This force can be applied at a temperature above A_f, at which the lattice does not yet transform spontaneously. But in this way only the variant $M1$ is favored, but not $M2$. A minimum force is required before the transformation starts. But since only one variant is induced, the interference between the variants on cooling is absent and the transformation can go to completion at a practically constant force. On unloading, the original lattice is restored since it is the most stable one without load. This is called superelasticity. It is clear that the force necessary to transform the lattice increases with temperature, if the stability of the square lattice with respect to the transformed one increases with the deviation from the M_s temperature.

The shape memory effect can be understood with reference to Fig. 1.7. On cooling without a stress all possible variants are formed, leading to a zero net shape change. If in this state a force is applied, the most favorable variant will grow at the expense of the other less favored ones, provided the interfaces between the different variants are mobile. This finally can lead to the same configuration as that which is obtained when the force is applied above M_s. The variant growth is associated with a shape change. On heating, this deformed material transforms back to the original shape of the high temperature phase. Thus the crystal has remembered its shape even after deformation in the martensitic state.

This simple picture of Fig. 1.7 can easily be extended to real three-dimensional crystals. There is a large group of metals and alloys which have a close-packed face centered (fcc) structure at elevated temperatures. This structure consists of close-packed planes in which each atom is surrounded by six neighbors, as shown in Fig. 1.8

On cooling this structure becomes unstable and transforms to a body-centered cubic

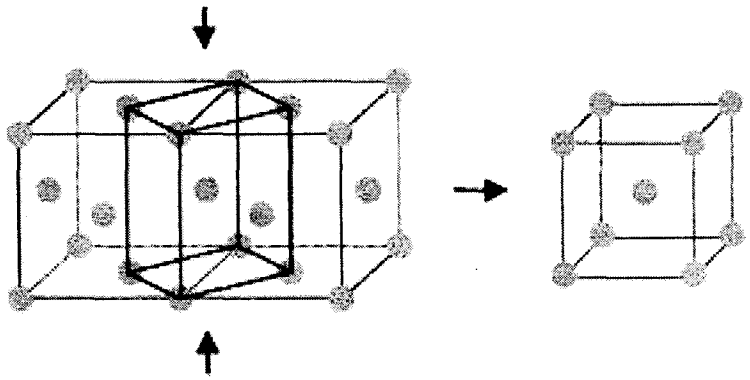

Figure 1.8: Two unit fcc cells with a smaller body centered tetragonal cell marked in the center (left). By a homogeneous compression in the direction of the arrows and an expansion in the plane normal to it the bcc structure (right) is obtained.

(bcc) lattice. The elementary bcc cell is a cube with the atoms on the corners and with an additional atom in the center. The transformation from fcc to bcc can be considered as a homogeneous distortion, like that in Fig. 1.7. This can be made clear by Fig. 1.8. In this figure are drawn two fcc cubic cells, and within them a smaller cell containing an atom in the center. This is a body centered tetragonal (bct) cell. By a homogeneous compression in the vertical direction, indicated by the arrows, and an expansion in the plane normal to it, a cubic bcc lattice is created without the need to change the volume of the bct cell.

1.2 Applications

The technological and medical applications of SMAs are numerous. The foremost application of SMAs are as actuators which are materials that change shape, stiffness, position, natural frequency, and other mechanical characteristics in response to temperature or electromagnetic fields. The diverse applications of these metals have made them increasingly important

and visible to the world.

To list a few potential commercial uses:

- Couplers: pipe couplings, electric connectors, package clamps.
- Temperature control devices: air conditioning controllers, shower head scald protection, overheat monitors, fire control safety valves and releases, radiator fan clutches, gas shut-off valves, water sprinklers.
- Medical Devices: Orthodontic wire (braces), orthopedic implants, Harrington rods, aneurysm clips, dental drill bit regulator, prosthetic limbs, steerable catheters, surgical anchors, clot filters.
- Separation mechanisms: manipulator release, buoy or tether release, ballast system release, launch-locking, payload jettison, protective shielding detachment, quick connect/disconnect joints, ejection seats, fin lock/unlock release.
- Miscellaneous: heat engines, mechanical muscles (robotics), toys, eyeglass frames, brassiere wire, connectors, fog lamp louvers, latching devices, motor protectors, valves, circuit breakers, retractable headlights.

Shape-memory alloys provide large displacements or forces within a small actuator design. However, the SMAs have slow dynamic response because the actuation is temperature controlled. In recent years, an alternative approach to (faster) actuation has emerged through the use of SMAs that are ferromagnetic in nature [7, 8]. In ferromagnetic shape memory alloys (FSMAs) a structural (martensitic) transition occurs in the ferromagnetically ordered state, in which case the Curie temperature T_C is higher than the martensitic transformation

temperature T_M. FSMAs offer an ability to cause actuation by an applied magnetic field rather than the slow process of shape change by temperature, thereby combining high strains with fast reaction times. The ferromagnetic Weiss domains in FSMAs are magneto-elastically coupled to and superimposed on the martensite structure. Due to this coupling, when the geometrical configuration of the magnetic domains is altered by an applied magnetic field, it also leads to a change in the relative volume fraction of the martensite twins, [9, 10, 11] thereby enabling field-induced shape change. This is illustrated in Fig.1.9.

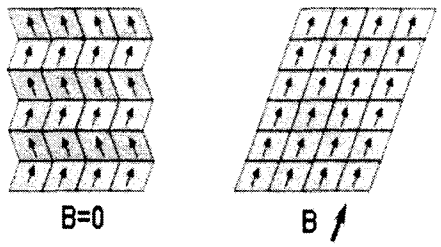

Figure 1.9: Reorientation of magneto-elastically coupled domains on application of magnetic field giving rise to a ferromagnetic shape memory effect.

Practical applications require large strains at low switching fields. The magnitude of the switching field, in turn, depends on the magnetoelastic coupling, which governs the magnitude of the applied field either to cause a structural transformation or change the relative volume fraction of martensite twins. The FSMAs are complex correlated systems whose physical properties are governed by interactions across different energy regimes (thermal, magnetic, and elastic). These interactions produce a rich variety of phenomena, such as, the magneto-elastic shape memory effect [7, 8], thermo-elastic shape memory effect, [12] and the magneto-caloric effect [13, 14]. A large magnetoresistance is also seen in some FSMAs

[15, 16, 17, 18]. Examples of FSMAs include the Fe-Pd, Fe-Pt, Fe-Ni, Fe-Ni Co-Ti, Co-Ni-Ga systems, and the family of Ni-Mn based Heusler alloys such as the Ni-Mn-Al, Ni-Mn-Ga, Ni-Mn-In, Ni-Mn-Sn, and Ni-Mn-Sb.

1.3 Ni-Mn Based Heusler Alloys

Heusler alloys are ternary, magnetic, intermetallic compounds, with a $L2_1$ crystal structure and are defined by the generic formula X_2YZ. The term is named after a German mining engineer and chemist Friedrich Heusler [19], who studied such an alloy (Cu_2MnSn) in 1903. For the Mn based alloys, Y-element is usually Mn, the X-element can be a transition metal like Co, Ni, Cu, Pd etc. and Z-element can belong to the Group III-V, viz. Al, Ga, Si, Sn, In, Sb, etc. Magnetism in such intermetallic alloys have been very early subjects of extensive first principle calculations with ever increasing interests [20, 21, 22, 23, 24, 25, 26, 27].

In the Heusler composition X_2YZ, when the X and Z elements are nonmagnetic, the magnetization is essentially confined to the Mn sublattice. When the element X is Co or Ni an additional magnetization appears at the Co or Ni sites [28]. These alloys offer an unique possibility to study manganese compounds where the Mn atom has only other transition metals (X) as the nearest neighbours and non-transition elements (Z) in the second coordination sphere. They are traditionally considered as the local moment systems and the ordering of the moments is through the indirect exchange interaction of the Ruderman-Kittel-Kasuya-Yosida (RKKY) -type mediated by the free electrons of the system [29, 30]. First principle band-structure calculations for these alloys have shown that the $3d$ majority-spin states of Mn are occupied and hybridize with the X-atom $3d$ states while the minority-spin $3d$ states of Mn lie above the Fermi level. These calculations also showed that, in addition

to the long range Mn-Mn interactions, the magnetic short-range X-Mn interaction is very important for systems with sizable magnetic moments on the X atoms such as Co and Ni [23, 25, 26, 27]. These interactions not only mediate the Mn-Mn interactions but they also participate in the formation of the magnetic state. The local nature of the Mn magnetic moments has been demonstrated by spectroscopic investigations reported in Ref. [24].

More recently, a comprehensive study of Mn based Heusler alloys with X = Ni has been attracting strong interests worldwide [31]. This is because of the discovery of structural phase transformation of martensitic type in a ferromagnetic matrix in Ni_2MnGa , thus giving rise to a fascinating field of "magnetic shape memory technology". Even though this FSMA research field is rather young, some good reviews have already appeared [32, 33, 34, 35, 36, 37].

Ni_2MnGa Heusler alloy is one of a very rare magnetic materials that undergoes a martensitic transformation below the Curie temperature, whereby the combination of magnetic and structural features is responsible for its unique magneto-mechanical properties that broaden the spectrum of many scientific fields. The stoichiometric composition, ferromagnetic Ni_2MnGa undergoes a martensitic transformation from a $L2_1$ cubic structure to an orthorhombic state at $T_M \approx 220$ K. From the technological point of view, Ni_2MnGa is much promising than other FSMAs presently in commercial use. For example, the well-known material Tb-Dy-Fe (Terfenol-D) exhibits magnetostrictive strains of about 0.1%, whereas, shear deformations up to 10% have been induced by magnetic field less than 1 T [38, 39] in Ni_2MnGa. Besides, in the off-stoichiometric Ni-Mn-Ga alloys, a giant magnetocaloric effect of the order of - 20 J/kg K with the application of relatively low magnetic field (maximum of 1.6 T) [14] and a large negative magnetoresistance (5% at 8 T), a highest reported value

for a SMA at room temperature [17], have been observed. These features together make Ni-Mn-Ga alloys very efficient for magnetic-shape-memory technology. However, due to the expensive constituent element Ga, the cost of large scale production is not very feasible for technological applications. The low martensitic and magnetic transformation temperatures could be altered to meet the technological standards by changing the stoichiometry but the brittle nature of this alloy further restricts its applicability. Therefore, the development of Ga-free FSMAs with high phase transformation temperatures and better mechanical strength is underway.

In this respect the alloy that is being most actively investigated is Ni_2MnAl. This ternary system is isoelectronic to Ni_2MnGa at equal compositions and exhibits similar thermoelastic transformation upon cooling [40, 41, 42, 43]. However, it was observed that, the magnetically induced strains in Ni-Mn-Al samples amounted to only 0.1% at the field value up to 7 T [44]. The type of magnetic ordering in the Ni-Mn-Al alloys strongly depends on the chemical ordering of the high-temperature phase, which changes under thermal treatment. Quenched samples have a B2 structure of the austenitic phase, and they exhibit either antiferromagnetism or a spin glass state. Aging the samples after quenching leads to the formation of the $L2_1$ structure of the austenitic phase, which has a ferromagnetic ordering with Curie temperature $T_C \sim 330$ K [45]. The advantage of Ni_2MnAl, over Ni_2MnGa is the higher ductility and the high structural transition temperature.

Other representatives of the Ni-Mn based Heusler family includes Ni_2MnZ with Z = In, Sn, Sb. These alloys are ferromagnetic and have Curie temperature values similar to that of Ni_2MnGa but do not undergo any structural transition. Martensitic transformation has been

observed in alloys with off-stoichiometric compositions: $Ni_{50}Mn_{50-x}Z_x$ (Z = In, Sn, Sb) with concentrations upto $\sim$ 16 at% Z-element [46]. Especially, the Sn and In alloy series have been in focus [47, 48, 49, 50, 51] and are known to exhibit exotic properties that promise various innovative applications. A giant inverse magnetocaloric effect has been reported in Ni-Mn-Sn alloys (18 J/kg K at 5 T) where the application of the magnetic field adiabatically cools the sample [47]. While large magnetoresistance at moderate field values has been observed in Ni-Mn-In alloys at temperatures very close to room temperature [18].

Among all these various FSMAs, the Ni-Mn-Ga system is widely studied and serves to be prototype for the design of new FSMAs. Hence most of the discussion that follows, with respect to Ni-Mn based FSMAs, will essentially focus the properties exhibited by Ni-Mn-Ga system. Before we discuss the physical properties of these alloys any further, a remark concerning the chemical composition of Ni-Mn based Heusler alloy would be in order. Almost all parameters of these Ni-Mn based alloys have proven to be very sensitive to the chemical composition of the samples. The sample's composition strongly affects the temperatures of phase transformations and the formation of superstructures in the austenitic and martensitic states. In the following, several investigations are described which have helped to clarify some phenomena related to the martensitic transformation.

1.3.1 Crystal Structure

Heusler alloys are categorized into two distinct groups by their crystalline structures; half Heusler alloys with the form of XYZ in the $C1_b$ structure and full Heusler alloys with the form of X_2YZ in the $L2_1$ structure as schematically drawn in Fig. 1.10.

The unit cell of the $L2_1$ structure consists of four face-centered cubic(fcc) sublattices,

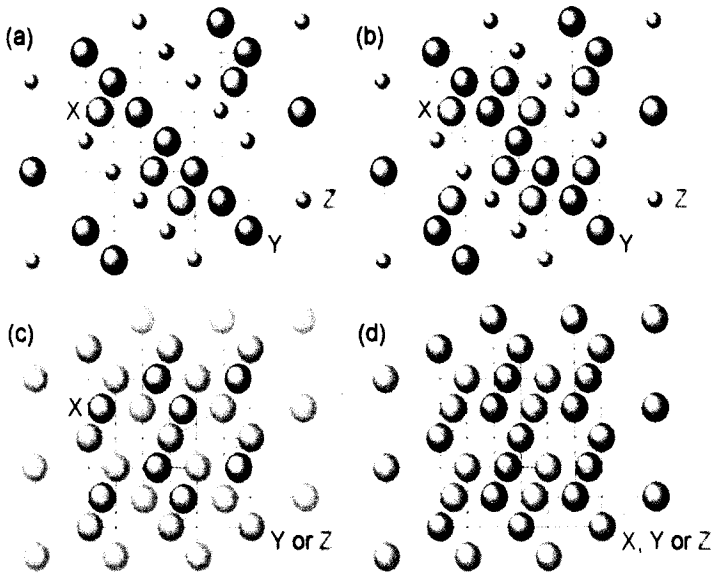

Figure 1.10: Crystalline structures of (a) half and (b) full Heusler alloys; $C1_b$ and $L2_1$ structures respectively. Disordered structures, (c) B2 and (d) A2, are also shown.

while that of the $C1_b$ structure is formed by removing one of the X sites. For the $L2_1$ structure, when the Y and Z atoms replace their sites (Y-Z disorder) and eventually occupy their sites absolutely at random, the alloy transforms into the B2 structure. In addition, X-Y and X-Z disorder finally forms the A2 structure.

In the past, it has been shown through neutron diffraction studies that Ni_2MnGa has the $L2_1$ structure at room temperature with space group $Fm\bar{3}m$. The cubic lattice constant a of Ni_2MnGa is 5.825 Å and the unit cell volume $V_{cub} \sim 198$ Å^3 [52]. In studies of the crystal structure of the non-stoichiometric Ni-Mn-Ga alloys by the x-ray (or electron) diffraction method no reflections corresponding to the $L2_1$ structure have been observed because the atomic scattering factors of the constituent elements are close to each other. Although the reflections observed in x-ray diffraction patterns represent only the short-range order corresponding to the B2 structure, traditionally the crystal structure of the cubic phase of

the family of $Ni_{2+x+y}Mn_{1-x}Ga_{1-y}$ alloys is considered as $L2_1$ structure. On the other hand, depending upon the stoichiometry, some Ni-Mn-In alloy compositions are known to have a B2 structure.

In the stoichiometric alloy, which is ferromagnetic below $T_C \approx 380$ K [53], two thermally induced phase transitions have been observed. From the high-temperature cubic Heusler structure, a premartensitic phase transformation to a modulated cubic structure occurs below $T_P \approx 260$ K [54] followed by the martensitic transformation to a modulated tetragonal structure below $T_M \approx 220$ K [52]. In other words, the parent $L2_1$ structure transforms to the martensite structure through the premartensitic phase. Occurrence of various "pretransitional" phenomena prior to the structural transformations of the martensitic type have been observed in a broad class of materials. Among these are the formation of soft modes in the lattice, anomalous broadening of the reflections in the x-ray spectrum, the emergence of a tweed structure, etc. Pretransitional phenomena are observed in superconductors with an A15 structure and in ferroelectrics with a perovskite structure [55] and in a broad class of shape memory alloys [56, 57]. What sets the Heusler alloy Ni_2MnGa apart from all other compounds that experience martensitic transformations is that, in addition to pretransitional phenomena [58, 59], there can be a premartensitic phase transition.

Many reports claimed the crystal structure to be tetragonal in the martensitic phase until recently, detailed analysis of the high resolution neutron powder diffraction pattern [60] revealed the exact sequence of phase transitions in Ni_2MnGa. It is seen that, as the temperature is lowered, and the system approaches T_P, a periodic shear of the $(110)_{cubic}$ planes along $[1\bar{1}0]_{cubic}$ direction occurs with a propagation vector $\frac{\pi}{a}[\frac{1}{3}, \frac{1}{3}, 0]$. The structure

is said to be modulated with a period of three lattice spacings (or six atomic planes) in the $[110]_{cubic}$ direction. This modulated structure can be described in space group *Pnnm* with modulations along the *b*-axis. However, the superstructure that develops below T_P, co-exists with the parent cubic structure. With further lowering of the temperature, martensitic transformation occurs at $T_M \approx 220$ K and the structure can be described as an orthorhombic lattice are $a = 4.2152$ Å , $b = 29.3016$ Å and $c = 5.5570$Å with modulations over 7 unit cells ($b/7$) along the *b*-axis - known as the *7M* modulated structure [60]. The martensitic phase accommodates the lattice distortion connected with transformation by formation of three twin variants twinned usually on $\langle 110 \rangle$ planes and having the orientation of the tetragonal symmetry axes nearly to three possible [100] directions.

With the deviation in stoichiometry, the Ni-Mn-Ga alloys exhibit three well-known martensitic phases, traditionally referred to as *5M* (five-layered martensite) , *7M* (seven-layered martensite) and *NM* (non-modulated martensite) phases [61]. This nomenclature, as explained above, refers to the periodic shear of the $(110)_{cubic}$ planes along $[1\bar{1}0]_{cubic}$ direction with modulation period of five (for *5M*) or seven (for *7M*) lattice spacings. A non-modulated martensitic phase, *NM* refers to the tetragonal $L1_0$ cell. The cubic lattice is said to be tetragonally distorted with $c/a < 1$ in the *5M* phase [52, 62], orthorhombically in the *7M* phase [60], and tetragonally with $c/a > 1$ for the *NM* phase [63].

Apart from these, martensitic phase transformation in the $Ni_{50}Mn_{50-x}Z_x$ (Z = In, Sn, Sb) Heusler alloys is a two- or three-step process [46]. The orthorhombic four layered structure, *4O*, with modulations over four lattice spacings formed upon structural transition in $Ni_2Mn_{1.44}Sn_{0.56}$ [64] has not been observed in Ni-Mn-Ga. This does not exhaust the

sequence of phase transitions in Ni-Mn based Heusler systems, since these alloys can experience a martensite-martensite transition known as "intermartensitic" transformations. An intermartensitic transition from the five-layered to seven-layered martensitic structure (*5M* → *7M*) is observed at $T_I = 283$ K during cooling of $Ni_{2.16}Mn_{0.84}Ga$ whereas the martensite-martensite transformation is absent upon heating [65].

It is important to mention at this point that, not all the Ni-Mn-Ga alloys undergo the premartensitic phase change. Only those alloy compositions which have a $T_M < 260$ K are known to exhibit this phenomenon. In particular, for the Ni excess alloys of the type $Ni_{2+X}Mn_{1-x}Ga$, the premartensitic transition is essentially independent of the composition x, with the value $T_P \sim 260$ K, and disappears for $x = 0.09$ in $Ni_{2.09}Mn_{0.91}Ga$ [66]. Furthermore, premartensitic phase change, has not been hitherto reported in similar systems like Ni-Mn-Al, Ni-Mn-Sn etc. that have transformation temperatures below 260 K.

1.3.2 Lattice Dynamics

Martensitic transformation is a purely structural, diffusionless, displacive solid-solid phase transitions [67]. Early attempts to understand these transformations suggested that a phonon mode would become unstable at a particular temperature, at which point the lattice would displace spontaneously to a finite amplitude [68, 69].

Ni_2MnGa undergoing a two-step martensitic phase transformation was studied by inelastic neutron scattering and neutron diffraction. Several anomalies in the phonon dispersion curves were observed in the parent cubic phase. It has been suggested that the premartensitic phase occurs as a result of anharmonic coupling between the $[\zeta, \zeta, 0]$ TA_2 phonon mode with homogeneous deformations associated with the Zener elastic constant $c' = (c_{11} - c_{12})/2$

[70]. The softening of the TA_2 phonon mode, observed in the inelastic neutron scattering measurements [59], starts well above the transition temperature T_M. For the sample with $T_M \approx 220$ K the squared frequency of the mode with $\zeta = 0.325$ has a linear dependence on the temperature $\nu^2 = a(T - T_\theta)$ as expected for the soft mode behaviour. However, the intercept $T_\theta \approx 250$ K is significantly higher than the T_M and the softening is incomplete with a reversal below 260 K. Thus in the region $T_\theta > T > T_M$ the $L2_1$structure is unstable to the formation of a premartensitic phase characterized by a $(\frac{1}{3}, \frac{1}{3}, 0)$ propagation vector. Ultrasonic measurements [71, 72, 73, 74] reveal that the magnitude of c', is anomalously low, namely 0.045 x 10^{11} N m^{-2} with a temperature variation which mirrors that of the soft mode frequency. Between 240 and 260 K, c' decreases by $\approx 50\%$ and on further cooling to T_M it increases by $\approx 30\%$. Thus some clues to the direction of modulation of the martensite structure are provided in the premartensitic phase by the softening of particular phonons and elastic constants. The TA_2 phonon dispersion curves of Ni-Mn-Ga alloys with different compositions which transform to different martensitic structures have been measured over a broad temperature range covering both paramagnetic and ferromagnetic phases. Softening of these anomalous phonons depends on particular martensitic structure. This softening is enhanced below the Curie point, as a consequence of spin-phonon coupling. This effect is stronger for systems with higher electronic concentration [75].

It is generally agreed that the true origin of the phonon anomalies lies in the strong coupling of certain phonons to the electrons (phonon softening), due to particular features in the Fermi surface [76, 77, 78, 79, 80]. Screening due to electron-phonon coupling involving electronic states near the Fermi level in metals can give rise to anomalous dips in the phonon

dispersion, called Kohn anomalies. The occurrence of these anomalies depends mainly on the geometry of the Fermi surface, as well as on the wave vector dependence of electron-phonon matrix elements. While anharmonic effects are thought to be responsible for the MT [81], it is Kohn anomalies [82] driven by nest-able regions on the Fermi surface impacting on the electronic screening (and hence on the electron-phonon coupling) that are suggested as the origin of the premartensitic phenomena [76]. It is well established that the Fermi surface nesting effect can be a driving force for the phonon softening preceding a MT. The geometry of the Fermi surface of Ni_2MnGa has been investigated by Refs. [80, 83, 84] and a comprehensive investigation including other Ni-Mn based Heusler alloys has been carried out by [85]. In cubic Ni_2MnGa, the Fermi level crosses both minority and majority-spin bands. Of the two bands at Fermi surface, only the one for the minority-spin bands shows obvious nesting features. In particular, they exhibit nesting features which are consistent with the anomaly in phonon dispersion observed experimentally [80]. Fermi surface nesting has been experimentally demonstrated for the case of shape-memory alloy $Ni_{0.62}Al_{0.38}$, using Compton scattering. This observation is compelling evidence that phonon anomalies are driven by the enhanced electron-lattice coupling due to the Fermi surface nesting [86].

The nesting considerably affects the transport properties of a metal due to the condensation of electrons in the nesting parts of the Fermi surface. It is conceivable that the various martensitic phases forming in Ni-Mn-Ga alloys are driven by the geometry of the Fermi surface that has a nesting vector corresponding to the modulation of martensite [84]. This implies that martensitic phases with different nesting vectors have different fractions of nested Fermi surface. Therefore, change in modulations in the crystal structure can af-

fect the number of conduction electrons due to the change of the Fermi surface available for conduction. This has been observed experimentally for intermartensitic transition in $Ni_{2.16}Mn_{0.84}Ga$ alloy [65].

1.3.3 Electronic Structure

Heusler alloys are very unusual metallic systems and the band structure calculations rightly reflect the same. The hybridization features and the resulting binding mechanisms for various Heusler alloys have been discussed to a large extent by Kübler *et.al.* in [23]. These calculations have shown that the $3d$ majority-spin states of Mn are occupied and hybridize with the X-atom $3d$ states while the minority-spin $3d$ states of Mn lie above the Fermi level. Further, the p electrons from the Z-element hybridize with the d electrons of the transition metals forming partially filled bands near the Fermi level [25]. Electronic structure calculations for Ni_2MnGa [87] show a peak in the DOS at the Fermi level, E_F. It was argued that it is the redistribution of the electrons around the Fermi level which drives the phase transition. The reduction in symmetry lifts the degeneracy of the electron bands at the Fermi level, allowing the peak in the DOS to split. The reduction of free energy resulting from the re-population of these bands may exceed that required to create the lattice distortion, in which case such a transformation is energetically favourable. However, the composition of the bands that are active at the Fermi surface are not identified in the DOS curves presented in this calculation.

The exact character of this peak at E_F was determined by the site projected DOS evaluated by Ayuela in [88]. It was found that the Fermi level E_F, lies just above a peak in the local DOS of the minority-spin Ni e_g band whereas, for the Mn band the E_F lies at a position

where there is almost equal local DOS of majority and minority t_{2g} states. Upon structural distortion, the peak in the minority Ni e_g band is split whereas little change is seen in the Mn bands near Fermi surface. Due to proximity of the Ni and Ga atoms, there is a hybridization of Ni atoms with Ga p states. Thus the peak at E_F comprises of the partially filled bands that results from the $p-d$ hybridization. The Ga atoms, contributing the p electrons, form energetically favourable hybrid states with d electrons of Ni. These states give rise to a peak in the spin-down electronic DOS right at the Fermi level. It is believed that the $p-d$ linkage is covalent in nature. The distortion of the crystal structure results in the polarizability of the electron cloud between Ga $4p$ and Ni $3d$ states resulting in the covalent interactions between them. Thus, the issue of electronic hybridization in Ni_2MnGa is analysed using a simple model. Here, the $L2_1$ state of Ni_2MnGa can be described as four interpenetrating face centered cubic lattices with Ni atoms sitting at the body centered (CsCl-type) environment. This causes the Ni $3d$ states to arrange themselves with the corresponding crystal field. The Fermi level of Ni_2MnGa thus lies in the valley of antibonding minority spin $3d$ states of Ni, which is a highly unstable situation. The system avoids this by undergoing a martensitic transformation with modulated structures [37].

Concerning the magnetic aspects, the experimentally observed total magnetic moment is 4.17 μ_B for the $L2_1$ cubic structure [89]. The polarized neutron scattering [90] gives the magnetic moments per site as Ni = 0.24 μ_B, Mn = 2.74 μ_B, and Ga = -0.013 μ_B in the cubic phase and Ni = 0.36 μ_B, Mn = 2.83 μ_B, and Ga = -0.016 μ_B in the martensitic phase. These findings suggest that the Ni contribution to the total change in magnetic moments is larger with respect to Mn, with a small redistribution of moments. The change in symmetry

of the magnetization distribution is consistent with a band Jahn-Teller mechanism wherein the unpaired electrons get redistributed between $3d$ sub-bands of different symmetries resulting from lattice distortion. In the cubic phase, the unpaired electrons have an overall e_g symmetry. In the tetragonal phase change, the degeneracy of the e_g and t_{2g} bands is raised and the unpaired electrons are redistributed in such a way that it can cross the Fermi level thereby lowering the band energy. In other words, the structural transition is driven by the band Jahn-Teller mechanism.

1.3.4 e/a Factor

It has long been known that in Hume-Rothery alloys, the valence electron concentration per atom (e/a) is extremely important in determining which crystal structure is stable [91]. It is calculated as the concentration weighted sum of the number of $3d$ and $4s$ electrons of X- and Y-element and the $4s$ and $4p$ electrons of Z-element. In the case of Ni_2MnGa, Ni offers 10 valence electrons, Mn offers 7 valence electrons and Ga offers 3 valence electrons. Putting this together, e/a works out to be,

$$\frac{\mathbf{2} \times 10 + \mathbf{1} \times 7 + \mathbf{1} \times 3}{4} = \frac{30}{4} = 7.5$$

In general, for the non-magnetic Hume-Rothery alloys, the martensitic transition takes place when the Fermi surface reaches the Brillouin zone boundary [52]. This implies that the change in the number of valence electrons and the alteration of the Brillouin zone boundary can be considered as the primary driving forces for the occurrence of structural instabilities in the Heusler FSMAs too. As mentioned earlier in the text, almost all parameters of Ni-Mn based alloys have proven to be very sensitive to the chemical composition of the samples.

In $Ni_{2+x}Mn_{1-x}Ga$ alloys, as the Ni concentration is increased, the T_M increases sharply with a corresponding decrease in T_C until for the composition $Ni_{2.19}Mn_{0.81}Ga$, T_M and T_C coincide with each other [92]. The increase of T_M with increasing x in the $Ni_{2+x}Mn_{1-x}Ga$ alloy systems is attributed to the increase in the valence electron concentration, e/a. Such empirical dependence of the electron concentration and martensitic transition temperature was found to hold for a large number of compositions, suggesting good applicability [94]. The temperatures of phase transformations and the formation of superstructures in the austenitic and martensitic states of Ni-Mn-Ga was also associated with this factor of e/a [95]. The relationship between tetragonal distortion c/a and e/a has been investigated [96, 97]. It was pointed out that e/a = 7.7 corresponds to the crossing of lines T_C versus e/a and T_M versus e/a for Ni-Mn-Ga alloys. In other words, for compositions which approximately follow the e/a value of $\approx$ 7.7, have $T_M = T_C$, while transformation takes place in the ferromagnetic regime for e/a $<$ 7.67 and in the paramagnetic regime for e/a $>$ 7.7. Particularly in the e/a range from 7.61 to 7.72, different crystal structures (*5M, 7M, or NM*) are observed as a result of martensitic transformation [95].

It is important to note that almost all the experimental results from the literature so far deals only with Ni-Mn-Ga systems. Hence any investigations of the variation in e/a becomes system specific. Further, with the changing composition, the change in T_C does not show a empirical dependence on e/a. The parameter e/a however, is of rather qualitative nature and can be useful in the development of the conceptual macroscopic view on the stability of Heusler structures. However, we cannot address the following question - can a Heusler alloy with some given value of e/a undergo a martensitic transformation or not?

1.4 Aim of the thesis

The aim of this thesis is to contribute to the study of the mechanism for the martensitic phase transformation seen in Ni-Mn based Heusler alloys. For a deeper understanding of the magnetic shape-memory mechanism in these alloys, a microscopic explanation for the origin of the martensitic transformation is necessary. This thesis describes in detail the local structural analysis of the $Ni_{2+x}Mn_{1-x}Ga$ and $Ni_{50}Mn_{35}Sn_{15-x}In_x$ alloys through their magnetic and martensitic structural transitions using X-ray Absorption Fine Structure as the major technique. This work presents new evidence for the crucial hybridization component that influences and leads to structural transitions in the Ni-Mn based Heusler alloys.

At the time of beginning of this thesis work, the general ideas about martensitic transformations and the superstructures related to the specific mechanical behaviour of the Ni-Mn-Ga alloys were not fully understood. Systematic studies of the ferromagnetic shape memory alloy Ni_2MnGa showed that the magnetic and structural transformations occur not only in the stoichiometric alloy but also in the cases with significant deviations from the stoichiometry [12]. Finding the composition dependencies of the main physical properties was an important step towards the understanding of this alloy-class. Hence it was planned to study the off-stoichiometric compositions of Ni_2MnGa with some systematic variation. The most familiar parameter then, was the e/a ratio that could be used as a reference to describe the deviation in stoichiometry for the Ni-Mn-Ga alloys. In Ni_2MnGa, e/a can be changed in two ways: substituting Ni for Ga without changing the Mn content or by substituting Ni for Mn without changing the Ga content. Obviously, replacing Ni (10 valence electrons) for Ga (3 valence electrons) would lead to larger change in electron concentration, but a better control

of c/a variation is achieved by replacing Mn with Ni.

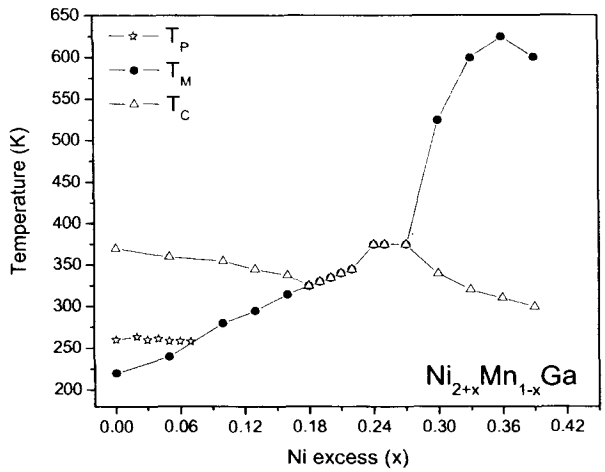

Figure 1.11: The dependence of pre-martensitic(T_P), martensitic (T_M) and ferromagnetic (T_C) transition temperatures on the Ni concentration x in $Ni_{2+x}Mn_{1-x}Ga$ alloys (adapted from [92, 93]).

The phase diagram that emerges for the composition $Ni_{2+x}Mn_{1-x}Ga$ is presented in Fig. 1.11. For the stoichiometric Ni_2MnGa, martensitic transition occurs at $T_M \approx 220$ K while the ferromagnetic ordering takes place at $T_C \approx 380$ K. It has been well-established that in $Ni_{2+x}Mn_{1-x}Ga$, increasing Ni content raises the martensitic transformation temperature and lowers the ferromagnetic transformation temperature until they coincide in the narrow composition range $x = 0.18$ - 0.27 [92, 93]. The changes in T_M are accompanied by appearance of differently modulated martensitic structures viz. *5M, 7M, NM-tetragonal*, in the crystal lattice. It has been argued that the lattice distortion breaks the degeneracy of the bands in the vicinity of the Fermi level causing a redistribution of the electrons in these bands and reduction in free energy - a band Jahn-Teller distortion [87, 90]. Thus understanding the variation in the density of states (DOS) at the Fermi level with changing concentration would

be interesting. We have studied this change in DOS of the $Ni_{2+x}Mn_{1-x}Ga$ alloys employing the temperature dependent Thermoelectric power (TEP) measurements.

Further, the nature of modulations forming the super-structures and the driving force for the martensitic transformation in these alloys was not fully understood. Theoretical calculations by [98, 99] indicated the importance of modulated structure and the shuffling of atomic planes in stabilizing the martensitic structure in stoichiometric and non-stoichiometric alloys. As per their calculations, the stability of the structure is associated with a dip in the minority-spin density of states (DOS) at the Fermi level, related to the formation of hybrid states of Ni *d* and Ga *p* minority-spin orbitals [85]. The results of ab-initio calculations by Zayak *et. al* [99] reported that the tetragonal phase is stabilized through the shuffling of atoms that gives rise to wave-like pattern of atomic displacements with well-defined period - modulations with the amplitude of modulations being different for Mn-Ga and Ni planes [98]. The tetrahedral distortions within the crystal lattice were speculated to be the reason for the shuffles in these alloys. Therefore a precise knowledge of the changes occurring in the local structure of constituent atoms was fundamental in understanding the mechanism involved in martensitic transformation. EXAFS is an ideal tool to study such transformations by making a comparative study of the local structure in austenitic and martensitic phases. It is with this objective that the XAFS investigation of the $Ni_{2+x}Mn_{1-x}Ga$ alloys was undertaken.

Having identified the hybridization features responsible for martensitic transition in the Ni-Mn-Ga alloys from the XAFS studies, it is important to test the inferences drawn, on alloys other than Ni-Mn-Ga. The key questions to be addressed here are: whether the hybridization component identified through the XAFS study of Ni-Mn-Ga, also applies to

other alloys of the Ni-Mn family? and to what extent does the magnetic ordering influence the hybridization features?

Towards this goal, we have investigated the alloy series $Ni_{50}Mn_{35}Sn_{15-x}In_x$ for the origin of the martensitic transformation. As mentioned earlier, the off-stoichiometric compositions: $Ni_{50}Mn_{50-x}Z_x$ (Z = In, Sn, Sb) with concentrations upto 16 at% Z-element are known to phase transform to martensitic structures. Interestingly, neither of the three alloys in their stoichiometric ratios are known to undergo a structural transformation. Infact, Ni_2MnIn has the same c/a (= 7.5) as Ni_2MnGa and the calculated phonon dispersions for this composition shows the anomalous behaviour similar to that seen in Ni_2MnGa [85]. Hence it would be challenging to identify the component that leads to structural phase change in the off stoichiometric Ni-Mn-In alloy and compare it with the features responsible for MT in the Ni-Mn-Ga alloys. Thus we planned to study the local structure of $Ni_{50}Mn_{35}In_{15}$ alloy composition that has an c/a value of 7.9 and a $T_M \sim 290$ K.

Further, Ni-Mn-Sn alloy with the similar composition ratio, $Ni_{50}Mn_{35}Sn_{15}$ is also known to undergo structural phase change. Electronically, Sn has one electron in excess to In, hence the c/a for this composition works out to be 8.05. Following the empirical dependence of martensitic transition temperature on the c/a value, the T_M for Ni-Mn-Sn should be higher than that of Ni-Mn-In. However, it is seen that $Ni_{50}Mn_{35}Sn_{15}$ undergoes MT at temperature close to that of Ni_2MnGa (T_M = 220 K). It is clear that the c/a parameter is certainly not the only factor influencing the phase transformations temperatures in such alloys. It becomes necessary to identify the feature that causes an electronic re-distribution at Fermi level driving the system to phase transformation. To resolve this issue of discrepancy in

the c/a dependence, it would be interesting to progressively replace In by Sn in the solid solution of the form $Ni_{50}Mn_{35}In_{15-x}Sn_x$ with $0 \leq x \leq 15$ and study the evolution of T_M and the martensitic structure with changing c/a.

Other aspect that adds to the complexity of such materials is the structural and magnetic ordering that may be different from Ni-Mn-Ga alloys. Compared to the stoichiometric Heusler configuration, the two systems, Ni-Mn-In and Ni-Mn-Sn contain excess Mn. Thus the crystal structure that forms upon the interpenetration of the of four fcc sublattices, may result in ordered structures different from basic $L2_1$. A different crystal structure ordering might give rise to additional magnetic interactions and affect the overall band occupation at the E_F. Thus, a local structure study of the Ni-Mn-In-Sn solid solution becomes important.

References

[1] The website of Texas A & M Smart Lab at http://smart.tamu.edu

[2] K. Otusuka and C. M. Wayman, Eds. *Shape Memory Materials*, Cambridge Univ. Press (1998).

[3] Z. Nishiyama, *Martensitic Transformation*, Academic Press, (1978).

[4] Manfred Ahlers, Revista Matéria **9** No: 3, (2004).

[5] L. C. Chang and T. A. Read, Trans. AIME. **191**, 47 (1951).

[6] W. J. Buehler, J. V. Gilfrich and R. C. Wiley, J. Appl. Phys. **134**, 1475 (1963).

[7] K. Ullakko, J. K. Huang, C. Kantner, R. C. O'Handley and V. V. Kokorin, Appl. Phys. Lett. **69**, 1966 (1996).

[8] R. D. James and M. Wuttig, Philos. Mag. A **77**, 1273 (1998).

[9] H. D. Chopra, C. Ji and V. V. Kokorin, Phys. Rev. B **61**, R14913 (2000).

[10] M. R. Sullivan and H. D. Chopra, Phys. Rev. B **70**, 094427 (2004).

[11] A. A. Cherechukin, I. E. Dikshtein, D. I. Ermakov, A. V. Koledov, D. A. Kosolapov, V. G. Shavrov, A. A. Tulaikova, E. P. Krasnoperov and T. Takagi, Phys. Lett. A **291**, 175 (2001).

[12] V. A. Chernenko, E. Cesari, V. V. Kokorin and I. N. Vitenko, Scr. Metall. Mater. **33**, 1239 (1995).

[13] F-X. Hu, B. G. Shen and J-R. Sun, Appl. Phys. Lett. **76**, 3460 (2000).

[14] L. Pareti, M. Solzi, F. Albertini and A. Paoluzi, Eur. Phys. J. B **32**, 303-307 (2003).

[15] T. Kakeshita and K. Ullakko, MRS Bulletin, **27(2)**, 105 (2002).

[16] Z. H. Liu, H. Liu, X. X. Zhang, X. K. Zhang and J. Q. Xiao, Appl. Phys. Lett. **86**, 182507 (2005).

[17] C. Biswas, R. Rawat and S. R. Barman, Appl. Phys. Lett. **86**, 202508 (2005).

[18] S. Y. Yu, Z. H. Liu, G. D. Liu, J. L. Chen, Z. X. Cao, G. H. Wu, B. Zhang and X. X. Zhang, Appl. Phys. Lett. **89**, 162503 (2006).

[19] F. Heusler, Verh. Dtsch. Phys. Ges. **5**, 219 (1903).

[20] S. Ishida, J. Ishida, S. Asano and J. Yamashita, J. Phys. Soc. Japan **45**, 1239 (1978).

[21] S. Ishida, Y. Kubo, J. Ishida and S. Asano, J. Phys. Soc. Japan **48**, 811 (1980).

[22] S. Ishida, S. Akazawa, Y. Kubo and J. Ishida, J. Phys.F: Met. Phys. **12**, 1111 (1982).

[23] J. Kübler, A. R. Williams and C. B. Sommers, Phys. Rev. B **28**, 1745 (1983).

[24] S. Plogmann, T. Schlathölter, J. Braun, M. Neumann, Yu. M. Yarmoshenko, M. V. Yablonskikh, E. I. Shreder, E. Z. Kurmaev, A. Worna and A. Ślebarski, Phys. Rev. B **60**, 6428 (1999).

[25] I. Galanakis, P. H. Dederichs and N. Papanikolaus, Phys. Rev. B **66**, 174429 (2002).

[26] J. Enkovaara, A. Ayuela, J. Jalkanen, L. Nordström and R. M. Nieminen, Phys. Rev. B **65**, 134422 (2002).

[27] E. Şaşioğlu, L. M. Sandratskii and P. Bruno, Phys. Rev. B **70**, 024427 (2004).

[28] P. J. Webster, J. Phys. Chem. Solids **32**, 1221 (1971).

[29] B. Caroli and A. Blandin, J. Phys. Chem. Solids **27**, 503 (1966).

[30] D. C. Price, J. Phys. F **8**, 933 (1978).

[31] I. Takeuchi, O. O. Famodu, J. C. Read, M. A. Aronova, K.-S. Chang, C. Craciunescu, S. E. Lofland. M. Wutting, F. C. Wellstood, L. Knauss and A. Orozco, Nat. Mater **2**, 180 (2003).

[32] R. C. O'Handley and S. M. Allen, *Encyclopedia of Smart Materials* edited by M. Schwartz, New York: Wiley, 931 (2001).

[33] A. N. Vasil'ev, V. D. Buchel'nikov, T. Takagi, V. V.Kholvailo and E. I. Estrin, Usp. Fiz. Nauk. **173**, 577 (2003) and references therein.

[34] B. Jiang, W. Zhou, W. Liu, and X. Qi, Mater. Sci. Forum **426-432**, 2285 (2003).

[35] O. Heczko, J. Magn. Magn. Mater. **290-291**, 787 (2005).

[36] O. Söderberg, Y. Ge, A. Sozinov, S-P. Hannula and V. K. Lindroos, Smart Mater. Struct. **14**, S223 (2005).

[37] P. Entel, V. D. Buchelnikov, V. V. Khovailo, A. T. Zayak, W. A. Adeagbo, M. E. Gruner, H. C. Herper and E. F. Wassermann, J. Phys. D: Appl. Phys. **39**, 865 (2006).

[38] S. J. Murray, M. A. Marioni, A. M. Kukla, J. Robinson, R. C. O'Handley and S. M. Allen, J. Appl. Phys. **87**, 5774 (2000).

[39] A. Sozinov, A. A. Likhachev, N. Lanska, K. Ullakko and V. K. Lindroos, J. Phys. IV **112**, 955 (2003).

[40] R. Kainuma, H. Nakano and K. Ishida, Metall. Mater. Trans. A **27**, 4135 (1996).

[41] K. Otsuka and S. Morito, Mater. Sci. Eng. A **208**, 47 (1996).

[42] Y. Sutou, I Ohnuma, R. Kainuma and K. Ishida, Metall. Mater. Trans. A. **29**, 2225 (1998).

[43] T. Inoue, S. Morito, Y. Murakami, K. Oda and K. Otsuka, Mater. Lett. **19**, 33 (1994).

[44] A. Fujita, K. Fukamichi, F. Gejima, R. Kainuma and K. Ishida, Appl. Phys. Lett. **77**, 3054 (2000).

[45] F. Gejima, Y. Sutou, R. Kainuma and K. Ishida, Mater. Trans. A. **30**, 2721 (1999).

[46] Y. Sutou, Y. Imano, N. Koeda, T. Omori, R. Kainuma, K. Ishida and K. Oikawa, Appl. Phys. Lett. **85**, 4358-4360 (2004).

[47] T. Krenke, E. Duman, M. Acet, E. Wassermann, X. Moya, L. Manosa and A. Planes, Nat. Mater. **4**, 450 (2005).

[48] T. Krenke, M. Acet, E. Wassermann, X. Moya, L. Manosa and A. Planes, Phys. Rev. B **72**, 014412 (2005).

[49] T. Krenke, M. Acet, E. Wassermann, X. Moya, L. Manosa and A. Planes, Phys. Rev. B **73**, 174413 (2006).

[50] K. Koyama, K. Watanabe, T. Kanomata, R. Kainuma, K Oikawa and K Ishida, Appl. Phys. Lett. **88**, 132505 (2006).

[51] K. Koyama, H. Okada, K. Watanabe, T. Kanomata, R. Kainuma, W. Ito, K Oikawa and K Ishida, Appl. Phys. Lett. **89**, 182510 (2006).

[52] P. J. Webster, K. R. A. Ziebeck, S. L. Town and M. S. Peak, Philos. Mag. **49**, 295 (1984).

[53] P. J. Webster and K. R. A. Ziebeck in *Alloys and Compounds of d-Elements with Main Group Elements*, Part 2, edited by H. R. J. Wijn, Landolt-Börnstein, New Series, Group III, **19/c**, Springer Berlin, (1988).

[54] A. Zheludev, S. M. Shapiro, P. Wochner and L. E. Tanner, Phys. Rev. B **54**, 15045 (1996).

[55] M. Nakanisi, A. Nagasawa and Y. Murakami, J. Phys. (Paris) **43**, C4-35 (1982).

[56] V. V. Kondrat'ev and V. G. Pushin, Fiz. Met. Metalloved. **60**, 629 (1985).

[57] A. Planes and L. Mañosa in *Solid State Physics*, **55** Academic Press, 159 (2001).

[58] G. Fritsch, V. V. Kokorin and A. Kempf, J. Phys.: Condens. Matter **6**, L107 (1994).

[59] A. Zheludev, S. M. Shapiro, P. Wochner, A. Schwartz, M. Wall and L. E. Tanner, Phys. Rev. B **51**, 11310 (1995).

[60] P. J. Brown, J. Crangle, T. Kanomata, M. Matsumoto, K-U. Neumann, B. Ouladdiaf and K. R. A. Ziebeck, J. Phys.:Condens. Matter. **14**, 10159 (2002).

[61] J. Pons, V. A. Chernenko, R. Santamarta and E. Cesari, Acta. Mater. **48**, 3027 (2000) and references therein.

[62] V. V. Martynov and V. V. Kokorin, J. Phys. III **2**, 739 (1992).

[63] B .Wedel, M. Suzuki, Y. Murakami, C. Wedel, T. Suzuki, D. Shindo, and K. Itagaki, J. Alloys. Compd. **290**, 137 (1999).

[64] P. J. Brown, A. P. Grandy, K. Ishida, R. Kainuma, T. Kanomata, K-U. Neumann, K. Oikawa, B. Ouladdiaf and K. R. A. Ziebeck, J. Phys.:Condens. Mater. **18**, 2249-2259 (2006).

[65] V. V. Khovailo, K. Oikawa, C. Wedel, T. Takagi, T. Abe and K. Sugiyama, J. Phys.: Condens. Matter **16**, 1951 (2004).

[66] V. V. Khovailo, T. Takagi, A. D. Bozhko, M. Matsumoto, J. Tani and V. G. Shavrov, J. Phys.: Condens. Matter **13**, 9655 (2001).

[67] S. M. Shapiro, B. X. Yang, Y. Noda, L. E. Tanner and D. Schryvers, Phys. Rev. B **44**, 9301 (1991).

[68] W. Cochran, Adv. Phys. **9**, 387 (1960).

[69] P.W. Anderson, *Fizika Dielectrikov*, edited by G. I. Skanavi, Acad. Nauk. SSR, Moscow, (1960).

[70] A. Planes, L. Mañosa and E. Vives, Phys. Rev. B **53**, 3039 (1996).

[71] J. Worgull, E. Petti and J. Trivisonno, Phys. Rev. B **54**, 15695 (1996).

[72] T. E. Stenger and J. Trivisonno, Phys. Rev. B **57**, 2735 (1998).

[73] L. Mañosa, A. González-Comas, E. Obradó, A. Planes, V. A. Chernenko, V. V. Kokorin and E. Cesari, Phys. Rev. B **55**, 11068 (1997).

[74] A. González-Comas, E. Obradó, L. Mañosa, A. Planes, V. A. Chernenko, B. J. Hattink and A. Labarta, Phys. Rev. B **60**, 7085 (1999).

[75] L. Mañosa, A. Planes, J. Zarestky, T. Lograsso, D. L. Schlagel and C. Stassis, Phys. Rev. B **64** 024305 (2001).

[76] G. L. Zhao and B. N. Harmon, Phys. Rev. B **45**, 2818 (1992).

[77] X. Huang, G. J. Ackland and K. M. Rabe, Nat. Mater. **2**, 307 (2003).

[78] I. I. Naumov and O. I. Velikokhatniy, J. Phys. Condens. Matter **9**, 10 339 (1997).

[79] X. Y. Huang, I. I. Naumov and K. M. Rabe, Phys. Rev. B **70**, 064301 (2004).

[80] C. Bungaro, K. M. Rabe and A. DalCorso, Phys. Rev. B **68**, 134104 (2003).

[81] Y.-Y. Ye, Y. Chen, K.-M. Ho, B. N. Harmon and P. A. Lindgard, Phys. Rev. Lett. **58**, 1769 (1987).

[82] W. Kohn, Phys. Rev. Lett. **2**, 393 (1959).

[83] Y. Lee, J.Y. Rhee and B.N. Harmon, Phys. Rev. B **66**, 054424 (2002).

[84] O. I. Velikokhatnyi and I. I. Naumov, Phys. Solid State **41**, 617 (1999).

[85] A. T. Zayak, P. Entel, K. M. Rabe, W. A. Adeagbo and M. Acet, Phys. Rev. B. **72**, 054113 (2005).

[86] S. B. Dugdale, R. J. Watts, J. Laverock, Zs. Major, M. A. Alam, M. Samsel-Czekala, G. Kontrym-Sznajd, Y. Sakurai, M. Itou and D. Fort, Phys. Rev. Lett. **96**, 046406 (2006).

[87] S. Fujii, S. Ishida and S. Asano, J. Phys. Soc. Japan. **58**, 3657 (1987).

[88] A. Ayuela, J. Enkovaara and R. M. Nieminen, J. Phys.:Condens. Matter. **14**, 5325 (2002).

[89] P. J. Webster, Contemp. Phys. **10**, 559 (1969).

[90] P. J. Brown, A. Y. Bargawi, J. Crangle, K-U. Neumann and K. R. Ziebeck, J. Phys. Condens. Matter. **11**, 4715 (1999).

[91] W. Hume-Rothery, Adv. in Physics **3**, 149 (1954).

[92] A. N. Vasil'ev, A. D. Bozhko, V. V. Kholvailo, I. E. Dikshtein, V. G. Shavrov, V. D. Buchelnikov, M. Matsumoto, S. Suzuki, T. Takagi and J. Tani, Phys. Rev. B **59**, 1113 (1999).

[93] V. V. Kholvaylo, V. D. Buchelnikov, R. Kainuma, V. V. Koledov, M. Ohtsuka, V. G. Shavrov, T. Takagi, S. V. Taskaev and A. N. Vasil'ev, Phys. Rev. B **72**, 224408 (2005).

[94] V. A. Chernenko, Scripta Mater. **40**, 523 (1999).

[95] N. Lanska, O. Söderberg, A. Sozinov, Y. Lee, K. Ullako and V. K. Lindroos, J. Appl. Phys. **95**, 8074 (2004).

[96] K. Tsuchiya, H. Nakamura, D. Ohtoyo, H. Nakayama, H. Ohtsuka and M. Umemoto, in *Proceedings of ISAEM 2000: 2nd International Symposium on Designing, Processing, and Properties of Advanced Engineering Materials*, Guilin, China, 20-21 October 2000: Interscience Enterprises Ltd. Switzerland, pp. 409-414 (2001).

[97] V. Chernenko, V. L'vov, E. Cesari, J. Pons, R. Portier and S. Zagorodnyuk, Mater. Trans., JIM **43**, 856 (2002).

[98] A. T. Zayak, P. Entel, J. Enkovaara, A. Ayuela and R. M. Nieminen J. Phys.:Condens. Matter. **15**, 159 (2003).

[99] A. T. Zayak and P. Entel, Mater. Sci. Eng. A. **378**, 419 (2004).

Chapter 2

Experimental Techniques: Basic Principle and Instrumentation

2.1 Introduction

In this chapter we shall discuss all the experimental work carried out in this thesis. Along with the sample preparation technique, the method adopted for measurements, basic principle involved, and the instruments used for all the experiments, are discussed below. In particular, to study the crystal structure and microstructure, techniques like X-ray Diffraction (XRD), Scanning Electron Microscopy (SEM) and Optical Microscopy were employed. The transport and magnetic properties were investigated using four-probe resistivity, thermoelectric power, a.c. magnetic susceptibility and magnetization as a function of temperature and magnetic field. In order to gain insight into the changes occurring in the local structure of constituent atoms undergoing martensitic transformation, X-ray absorption fine structure (XAFS) study has been undertaken. By making a comparative study of the local structure in austenitic and martensitic phases, changes in the atom coordination and bond distances can be determined. The difference in the local structure in the $L2_1$ state and the tetragonal phase provide evidence for the cause of modulations.

2.2 Sample Preparation Technique

Arc-melting the starting metals in an inert gas atmosphere is a conventional method adopted for the synthesis of alloys. In the present study the *Centorr* Tri-Arc Furnace has been employed for the preparation of various Heusler alloys. In the simplest form, this instrument comprises of a water cooled/ air cooled copper hearth and tungsten electrodes. Due to the high voltage difference maintained between the electrodes and the copper hearth, an arc can be generated when the electrodes strike the hearth. Appropriate quantities of the constituent elements forming the alloy are held in one of the cups of the copper hearth. Along with these starting elements, a small piece of pure titanium metal is placed in the other cup of the hearth. It is important to have an oxygen-free, inert atmosphere for melting to avoid any loss in the sample composition due to formation of metal-oxides. To generate an inert atmosphere in the melting zone, the atmospheric air is evacuated and the melting zone is flushed repeatedly with high purity argon gas. A small but positive pressure of Ar gas is always maintained in the melting zone. Inorder to further remove any trace amount of oxygen, an arc is strike-out and focused on the Ti piece which acts as an oxygen getter. The elements of interest are then repeatedly melted and a fairly homogeneous polycrystalline bead is formed giving an alloy of desired composition. Modifications in the basic design of the instrument can be made to obtain single crystals as well. However, in the present series, polycrystalline beads of the Heusler alloys were prepared with compositions as given below:

- $Ni_{2+x}Mn_{1-x}Ga$ with x = 0, 0.05, 0.10, 0.13, 0.16, 0.19
- $Ni_{50}Mn_{35}Sn_{15-x}In_x$ with x = 0, 3.75, 7.5, 11.25, 15

The stoichiometric amounts of starting elements with 4N purity were melted in the water-cooled, tri-arc furnace under argon atmosphere. The metallic beads so formed were sealed under vacuum ($\approx 10^{-5}$ mm of Hg) in quartz ampoule and annealed for 48 hours at high temperature followed by quenching in ice-cold water. To be precise, Ni-Mn-Ga alloys were annealed at 1000 K and Ni-Mn-Sn-In alloys were annealed at 750 K. Using a low speed diamond saw, these beads were cut into pieces of desired shapes and sizes as per the requirement of different experiments.

2.3 X-ray Diffraction

X-ray diffraction is a widely used technique to determine the crystalline phase in the bulk materials. The wavelength of X-ray is comparable to the distance (d) between the crystal planes. Diffraction occurs when the Bragg condition which states that, the x-rays reflected from the two neighbouring planes of atoms must coherently interfere, is satisfied. This condition is fulfilled when the extra distance traveled by the x-rays to the farther plane of atoms is equal to the multiple of the X-ray wavelength, i.e. $2d\sin\theta = n\lambda$, where n is an integer, (as illustrated in the Fig. 2.1) giving rise to diffraction in solids [1, 2].

An X-ray diffraction can be carried out on the polycrystalline (powder) samples or single crystals. The XRD pattern is a plot of intensity of diffracted rays versus Bragg angle and contains information about the structure and the composition of the basis. This information needs to be extracted from the pattern by employing a proper analysis procedure.

In the present study, the sample beads were crushed to fine powder in an agate pestle and mortar. The fine powder so obtained was sealed under vacuum in quartz ampoule and further annealed at 1000K for 24 hours in an evacuated quartz tube in order to remove

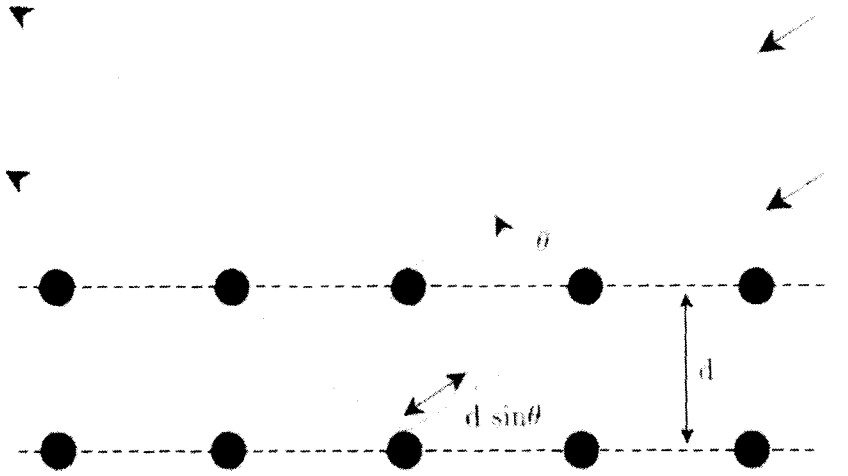

Figure 2.1: The Bragg condition, $2d\sin\theta = n\lambda$, where n is an integer, the extra distance traveled by the x-rays to the farther plane of atoms is equal to the multiple of the X-ray wavelength.

any internal stress. Room temperature X-ray diffraction patterns of powdered samples were recorded on the Rigaku D-MAX IIC diffractometer with Cu Kα (λ = 1.5418Å) radiation source. The Kβ lines were filtered out using a single crystal graphite (002) monochromator. This monochromator was critically adjusted so as to allow only the diffracted beam from the Kα lines. The patterns were recorded in continuous mode in the the 2θ range of 20° to 100° with a step size of 0.02 and at a speed of 1°/min.

2.4 Microscopy

Electron and optical microscopic techniques have been used to study the elemental concentration in prepared materials to check their compositions as well as the surface morphology in austenitic and martensitic phases.

The scanning electron microscopy (SEM) is a type of electron microscopy capable of producing high resolution images of a sample surface. Due to the manner in which the image is created, SEM images have a characteristic three-dimensional appearance and are useful for

judging the surface structure of the sample. In a typical scanning electron microscope, electrons are thermionically emitted from a tungsten or lanthanum hexaboride (LaB_6) cathode and are accelerated towards an anode. The electron beam, which typically has an energy ranging from a few hundred eV to 50 KeV, is focused by one or two condenser lenses into a beam with a very fine focal spot sized 1 nm to 5 nm. The beam passes through pairs of scanning coils in the objective lens, which deflect the beam over a rectangular area of the sample surface. Through these scattering events, the primary electron beam effectively spreads and fills a teardrop-shaped volume, known as the interaction volume, extending from less than 100 nm to around 5 μm into the surface. Interactions in this region lead to the subsequent emission of electrons which are then detected to produce an image. The various interactions that can occur as the energetic electrons in the microscope strike the sample are shown schematically in Fig. 2.2 and are described below.

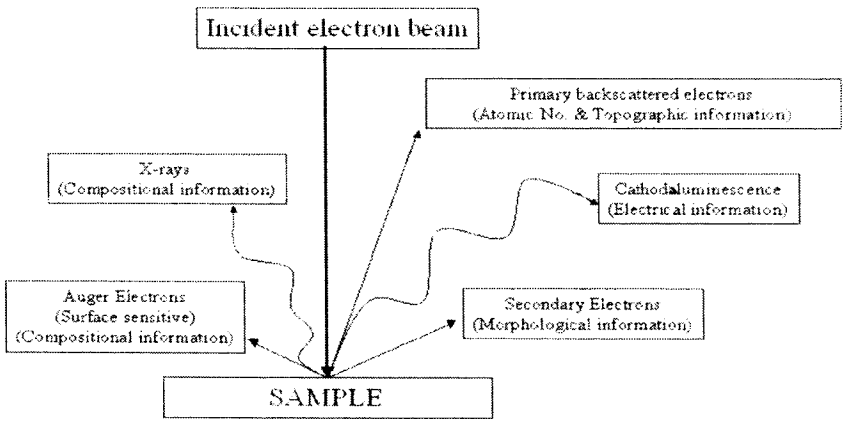

Figure 2.2: Schematics of the interaction of incident electron beam with the sample under investigation.

The primary backscattered electrons can be used to form an electron backscatter diffraction image and used to determine the crystallographic structure of the specimen. Secondary

electrons are monitored and the resulting signal is rendered into a two-dimensional intensity distribution that can be viewed as a digital image. Thus morphology of the sample surface such as the shape and size of the particles making up the object can be obtained. Associated with the formation of secondary electrons are the Auger electrons and x-rays. These have a characteristic energy, unique to each element from which it was emitted. This information is utilized to differentiate parts of the specimen that have different average atomic number and hence compositional information about the sample can be obtained.

The specimen for microstructural study has to be a highly polished surface. For this, slices of thickness $\sim$ 1 mm were cut from the original sample bead using a low speed diamond saw. These pieces were mounted in a wax mold (caldofix), baked in oven for 2 hours at 65°C and wet sand-grit ground using silicon abrasive papers of different roughness (800, 1200 and 2500 grade). These samples were then mounted on a polishing machine and the surfaces mirror finished using 1 micron base. The samples were then washed in alcohol using an ultra sonic bath. These were then mounted on a metal base using a carbon glue for earth contact and were analysed for compositional information using Energy dispersive X-rays (EDX). Later the surface of the same samples were etched for 10 minutes in the Oberhoffer solution made by mixing 1gm $CuCl_2$, 30g $FeCl_3$, 0.5gm $SnCl_2$, 42ml HCl, 500ml H_20 and 500ml C_2H_5OH. The microstructure of the samples so obtained were examined by SEM and optical microscopy.

2.5 Four Probe Resistivity

Temperature dependent electrical resistivity measurements on all the samples were made using the in-house conventional d.c. four probe setup. This resistivity insert has a sample

holder with four equidistant copper contacts. The sample is mounted on this holder using G-varnish that electrically isolates the sample from rest of the insert while maintaining a good thermal contact. A manganin heater radially wound just above the sample holder serves to control the temperature of the sample. Here the desired current through the sample is passed through the outer two contacts using a Keithley 224 programmable constant current source and potential developed across inner two contacts made on the sample is measured using a Keithley 2182A nanovoltmeter. The entire system is evacuated and cooled in a liquid Nitrogen dewar and the temperature is measured with a calibrated Platinum resistor (Pt-100) having an accuracy of 0.1 K using Keithley 2010 multimeter. Using this set-up measurements in the temperature range 77 K to 350 K can be made.

Rectangular bars with dimensions $\approx$ (2mm$\times$5mm$\times$1mm) were cut from the sample bead and used for the measurements. The data acquisition was carried in the cooling, warming and subsequent cooling cycles in the temperature range: 77 K to 350 K.

2.6 Thermoelectric Power

If two different conductors are joined together at the two ends to form a pair of junctions and these junctions are kept at different temperatures, a thermo emf ΔV is set up between the two junctions, which is proportional to the temperature difference ΔT i.e. $\Delta V \propto \Delta T$ provided ΔT is small. This is also known as Seebeck effect. The ratio of the emf to the temperature difference is called the thermoelectric power or thermopower **S** of the combination which depends on the temperature T. i.e

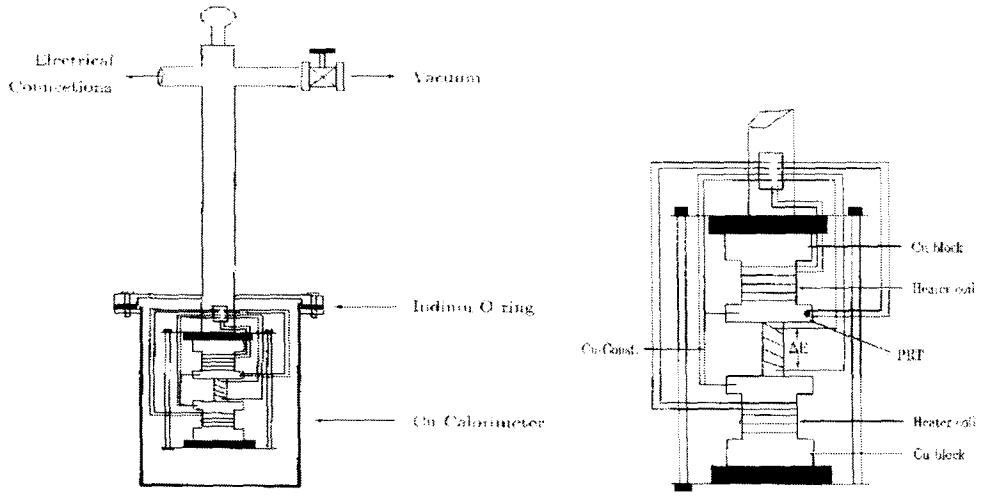

Figure 2.3: A layout of the thermopower setup and the sample holder assembly.

$$\mathbf{S} = \left|\frac{\Delta V}{\Delta T}\right|_{\Delta T small} \Delta T \ll T \tag{2.1}$$

For the measurement of thermopower a standard differential method was used. These measurements were carried out using the setup developed at the Physics Department, Goa University [3]. The experimental set-up and the sample holder are shown in Fig.2.3. Here, the sample is kept between two highly polished copper plates, electrically insulated from the rest of the sample holder. Two heater coils, one on the bottom and the other on the top copper plate, serve to raise the overall temperature of the sample and to maintain a temperature gradient across the length of the sample respectively. The overall temperature of the sample is measured by a Platinum Resistance thermometer (PT-100) while the gradient is monitored by a copper-constantan thermocouple operating in the differential mode. The system is cooled in a liquid Nitrogen dewar. The emf developed across the thermocouple,

the voltage across the sample and the temperature is measured using Keithley 2010 digital multimeter equipped with a multiple data scanner card.

To measure the thermopower **S** at a particular temperature say T, the temperature difference across the sample is first adjusted to nearly 0 K or $\sim 1\mu V$ (for the copper-constantan thermocouple $\sim 40\mu V \equiv 1$ K at 300 K) by passing current through the two heater coils. The top copper plate of the sample holder is then heated resulting in a thermo emf V_s across the sample. The voltages V_s and that developed across the thermocouple V_{th} are measured for different temperature gradients between the two plates. A graph of V_s versus V_{th} is plotted and its slope $(\Delta V_s/\Delta V_{th})$ is measured. Knowing the slope and the thermopower, S_{th} of the thermocouple at T, thermopower **S** is obtained.

In the present study, the sample beads were placed between the copper plates and the measurements were carried out in the temperature range 100 K to 400 K in the warming/cooling cycles similar to that of resistivity measurements.

2.7 a.c. Magnetic Susceptibility

The magnetic susceptibility is the degree of magnetization of a material in response to an applied magnetic field. The dimensionless volume magnetic susceptibility, represented by the symbol χ_v, is defined by the relationship

$$M = \chi_v H \tag{2.2}$$

where M is the magnetization of the material (the magnetic moment per unit volume or **m**/V), measured in amperes per meter, and H is the applied field, also measured in amperes per meter.

Unlike the d.c. susceptibility measurement technique where the actual values for the magnetic moment are measured, the slope of the magnetization curve with respect to the applied field is determined in an a.c. susceptibility measurement. This aspect of the a.c. measurements is extremely useful for studying unknown systems and the magnetic transitions. It is also a powerful technique to study ferromagnetic materials where the magnetic susceptibility is not linear i.e. the response is dependent upon the state of sample and can occur in directions other than that of the applied field.

In an a.c. susceptibility measurement the applied field has the form, $H_{ac} = h_0 \cos(\omega t)$. The resultant magnetization due to this a.c. term is given by $M_{ac} = m_0 \cos(\omega t - \theta)$ where θ is the phase difference between the applied field and the magnetization. The expression for M can be rewritten as,

$$M_{ac} = \chi' h_0 \cos(\omega t) + \chi'' h_0 \sin(\omega t) \tag{2.3}$$

where $\chi' = m_0 \cos(\theta)/h_0$ is the real or in-phase susceptibility component and $\chi'' = m_0 \sin(\theta)/h_0$ is the imaginary or out-of-phase component. These combine to form the complex susceptibility: $\chi_{ac} = \chi' - i\chi''$.

The basis of a.c. susceptibility technique is the a.c. mutual inductance bridge. A typical a.c. susceptometer is comprised of a set of co-axial mutual inductance coils: a primary coil and a pair of counter-wound identical secondary coils. The sample is placed in one of the secondary coils and an induced voltage signal proportional to the dynamic susceptibility, is detected. An overall schematic view of the a.c. susceptometer used in the present study is shown in Fig. 2.4.

The drawing of the coil arrangement and the positioning of the sample are also shown.

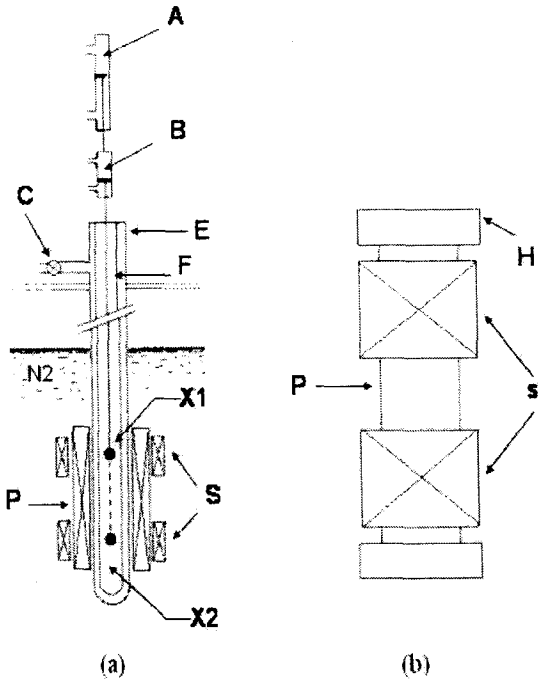

Figure 2.4: (a) Schematic diagram of the susceptometer. A - electrical connections, B - exchange of samples, C - vacuum valve, E, F - glass tube and the sample holder rod, P - primary coil, [S1 S2] - secondary coils, [X1 X2] - sample positions in the two secondary coils. (b) Placement of the primary and secondary coils on the hylam cylinder.

Details of the coil system are provided in Table 2.1. To ensure high precision measurements with a good resolution and to avoid any off-balance signal, a high degree of symmetry is maintained in the arrangement of the coils with respect to each other. The primary coil is wound directly on a hylam cylinder and covered by a few layers of Teflon tape, on which the secondary coils are wound. These coils are wound in opposite directions, using single copper wire without soldering the joints. The coil system is immersed in the liquid nitrogen bath. The sample rod is made of stainless steel held through an O-ring and attached to the system with a threaded screw type of adjustment. This assembly is placed in a quartz glass tube (Fig. 2.4). The lowest part of the sample rod consists of a heater and a temperature sensor

Table 2.1: Details of the coil design.

	Primary Coil	Secondary Coils
Turns	3000	5000
Resistance	680 Ohms	1300 ohms
Length	100 mm	20 mm with 30 mm spacing between the two coils

(Pt-100 resistor). The heater consists of resistance wires glued to the sample holder stage in the direction parallel to the sample rod, thus preventing an inductive coupling with the coil system.

To ensure the precision of the measurement, the system is checked for any offset voltage without any sample. The offset is compensated by passing a sinusoidal voltage of suitable amplitude through one of the secondary coils. This set-up has a facility to move the sample linearly such that it can be placed exactly at the centre of either of the secondary coils. During the measurements, the sample is first placed in one of the secondary coils and a set of induced voltages is recorded by a lock-in amplifier. It is then moved into the second coil and another set of measurement is taken. Susceptibility of the sample is calculated by averaging over both the sets recorded at the same temperature. The temperature control of better than 1% is achieved using a Lakeshore temperature controller.

We have carried out measurements in the temperature range 150 K - 400 K at a primary excitation frequency of 119.5 Hz and an amplitude of 2.5 Volts. Prior to the actual sample measurement, the set-up was calibrated using the known sample of gadolinium sulphate.

2.8 d.c. Magnetization (VSM)

Many different magnetometers have been devised to measure and characterize magnetic materials. Of these, the Vibrating Sample Magnetometer (VSM) is an elegant instrument with widespread usage for direct experimental determination of the properties of ferromagnetic materials. The VSM comprises two principle components, the sample vibrator mechanism and the induction signal detection coils, the latter being situated in close proximity to the sample which is also positioned in an external magnetic field. The VSM, shown schematically in Fig. 2.5, employs an electromagnet which provides the DC magnetizing field, a vibrator mechanism to vibrate the sample in the magnetic field, and detection coils which generate the signal voltage due to the changing flux emanating from the vibrating sample. The output measurement displays the magnetic moment M as a function of the field H. If extremely high magnetic fields are required, the electromagnet is replaced by a superconducting solenoid.

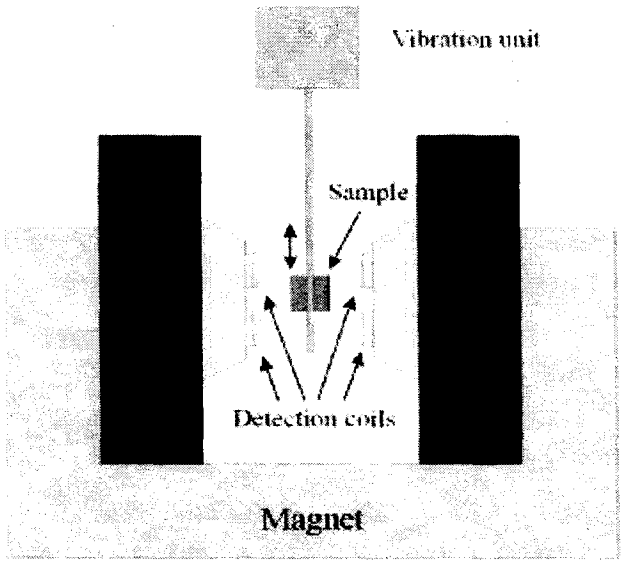

Figure 2.5: A schematic layout of the Vibrating Sample Magnetometer.

The basis of Vibrating Sample Magnetometer technique is to measure the rate of change of magnetic flux by the mechanical vibration of a magnetized sample, which produces an *emf* in a detection coil system (in first derivative configuration). The sample, which is magnetized by a *homogeneous* (assumed to be) DC magnetic field, oscillates sinusoidally with a small fixed amplitude w.r.t. the stationary pick-up coils. The relationship between the sample magnetization M and the induced *emf* ε is obtained from the time derivative of the Eqn, *viz.*,

$$\varepsilon = -\partial\Phi/\partial t = -\partial\Phi/\partial z \times \partial z/\partial t. \tag{2.4}$$

where $z = z_0 + a\cos(wt)$, w is the frequency of vibration, and the sample is considered as a magnetic dipole.

However, if the sample is not uniformly magnetized, then higher order magnetic moments (*viz.*, quadrupole, octupole, *etc.*) may come into consideration. We have used an Oxford Instruments 3001 Vibrating Sample Magnetometer (VSM) with a 12 T superconducting magnet for the dc magnetization measurements, where the sample is placed at such a z value, that the response from the dipole moment is maximum and the contribution from higher moments is absent. We have also assumed that the sample is small and the external dc field is approximately homogeneous across the scan length. The sample under investigation can be mounted in a sample holder at the end of a carbon fibre rod and inserted into an Oxford Instruments CF1200 continuous flow Helium Cryostat. The tail of the cryostat lies inside a conventional NbSn superconducting magnet whose 10 V - 120 A power supply can achieve fields up to 12 T. Once a DC field is applied, the sample is vibrated at a constant frequency of 66 Hz with an amplitude of about 1.5 mm along the vertical axis in a uniform applied field.

Two pickup coils, placed above and below the sample, experience a change of the magnetic flux due to the motion of the sample and, according to Faraday's law, an emf, proportional to the rate of that change of flux, is therefore induced in the two pickup coils. The induced emf, also proportional to the magnetic susceptibility of the sample, passes through a two-stage amplification process and is monitored by the VSM electronics and recorded on a computer via a standard RS232 connection. The sample temperature is measured by a AuFe/Chromel thermocouple in direct contact with a copper heat exchanger situated below the sample. The temperature control (temperature range : 3.6 - 320 K) is achieved by an Oxford Instruments ITC4 temperature controller.

2.9 X-ray Absorption Fine Structure Spectroscopy

X-Ray Absorption Fine Structure commonly known as XAFS is a technique employed to study the chemical environment of the atoms in a crystal. When a high energy X-ray photon is absorbed, a core level electron is emitted if the incident energy of the photons exceeds its binding energy. This causes a sharp dip in the transmitted intensity which is called as "absorption edge". The outgoing photo-electron can be thought of as a spherical wave expanding in all directions. When such a wave reaches the neighbouring atoms, it will be partially back-scattered. The back-scattered wave interferes with the outgoing electron wave causing a constructive or a destructive interference. The net effect is the modulation of the transmitted x-rays through the absorber upto about 1000 eV from the absorption edge. The interference pattern depends mainly on the number, nature and distance of the surrounding atoms from the absorbing atom. Thus XAFS proves to be a useful tool for study the local environment of the atoms in a solid.

The XAFS experiment can be divided into three parts, the experimental set-up, the sample preparation and the data analysis procedure. The first two parts will be discussed below while the actual procedure for data analysis is discussed with Ni-metal XAFS as an example and presented in the next Chapter.

2.9.1 Experimental Setup

The X-ray absorption experiment can be carried out in the transmission as well as fluorescence mode. All the experiments presented in this thesis were carried out in transmission mode at the EXAFS-1 beamline at the ELETTRA synchrotron source, Trieste, Italy. The X-ray source here is the bending magnet type with 1.2 T field and the energy ranges from 2 - 2.4 GeV with injection current of 300 mA (@ 2 GeV) and 130 mA (@ 2.4 GeV).

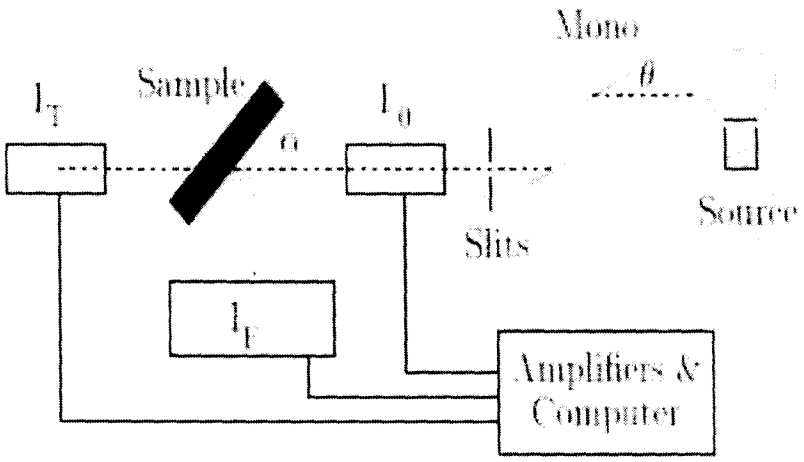

Figure 2.6: Schematic of the XAFS experiment.The setup for both the transmission and fluorescence geometries is depicted.

Figure 2.6 shows the schematic of a typical XAFS experiment for both, transmission and fluorescence geometries. The main components are: the monochromator used to select the X-ray energy, the slits, and the ion chambers used to sample the incident and transmitted

X-ray intensities. Polychromatic x-rays are produced by the synchrotron radiation source or by bremsstrahlung from a conventional laboratory source and a desired energy band of approximately 1 eV bandwidth is then selected by diffraction from monochromator. The monochromator consists of two channel-cut silicon crystals held parallel to each other. Only those X-ray photons that are of the correct wavelength λ ($\lambda = hc/E$, where h is the Planck's constant and c is the speed of light) to satisfy the Bragg condition $n\lambda = 2d \sin\theta$ at the selected angle θ will be reflected from the first crystal. The parallel second crystal is used as a mirror to restore the beam to its original direction. However, alongwith the fundamental edge energy E, the monochromator crystals can pass higher order harmonics (like $2E$, $3E$, etc) into the experimental beam. Making the two crystals slightly non-parallel by detuning the second crystal eliminates the higher order harmonics that would interfere with the fundamental reflections. The harmonics rejection is further achieved by using X-ray mirrors made of metals with high atomic number viz. Rh or Pt.

The slits placed after the monochromator define the size of the beam that strikes the sample. The dimensions of the slits are so chosen as to strike a balance between two contrasting aspects: maximizing the throughput and maximizing the energy resolution. The throughput is increased by opening the slits as more photons pass through. However, due to the angular divergence of the X-ray source and the geometry of the monochromator, there is a spread of energies compromising the energy resolution. The slit window at EXAFS-1 beamline at ELETTRA has a rectangular geometry and all four sides can be adjusted to attain a critical size of the beam incident on the sample. The incident and transmitted X-ray fluxes are monitored usually with gas ionization chambers. The ion chambers are ba-

sically, parallel plate capacitors with high voltage maintained across the plates. The region in between the plates is filled with gas that gets ionized when x-rays travel through it. The associated electronics measures the current produced and hence determines the proportional X-ray intensity. The choice of a particular gas or mixture of gases that fills the ion chambers is made on the basis of the X-ray edge energy to be measured. Finally, the sample is affixed onto a motorized sample stage with micrometric movement to facilitate the movement of the sample into the beam. For the XAFS measurements at ambient conditions, sample is in direct contact with the surroundings. XAFS can also be carried out in wide range of sample environment conditions with suitable modifications at the sample holder stage. In the present work, in addition to room temperature, low temperature measurements have been carried out. For this, a liquid nitrogen dewar attached with a copper based sample holder with multiple sample mounting facility has been used. The samples under investigation being in thermal contact with the liquid nitrogen, measurements were carried out after sufficient cooling.

2.9.2 Sample Preparation

The form of the sample for XAFS experiment is just as important as the technique of measurement and needs to be prepared in much the same way with due consideration to absorption of X-ray photons. The most important characteristics of an XAFS sample are its thickness, homogeneity and purity. The sample thickness is determined by optimizing the signal to noise ratio. This corresponds to an edge step absorption coefficient of about 1.0 while total absorption coefficient does not exceed 2.5. The homogeneity of the sample is important because the XAFS signal gets attenuated if part of the x-rays do not pass through

Atoms	K-edge Energy[a]
Mn	6.54 KeV
Ni	8.33 KeV
Ga	10.37 KeV

[a] see reference [4]

the sample. The particle size of the powder sample should be fairly uniform.

Taking into consideration all these factors, absorbers for the XAFS experiments were made by spreading very fine powder of the sample on a scotch tape avoiding any sort of sample inhomogeneity and pin holes. Small strips of the sample coated tape were cut and were held one on top of other. This assembly of the sample coated tape was sandwiched in between the scotch tape and held onto the sample holder plate. Enough number of such strips were adjusted to give absorption edge jump, $\Delta\mu x \leq 1$. XAFS at Mn, Ni and Ga K-edges were recorded in the transmission mode using Si(111) as monochromator. The K-edge energies of Mn, Ni and Ga are given in the table above.

The measurements were carried out at room temperature and liquid Nitrogen temperature. The incident and transmitted photon intensities were simultaneously recorded using gas-ionization chambers filled with mixtures of He-N_2 for Mn and Ni edge and Ar-N_2 for Ga edge. Measurements were carried out from 300 eV below the edge energy to 1000 eV above it with a 5 eV step in the pre-edge region and 2.5 eV step in the EXAFS region. At each edge, three scans were collected for each sample.

Data analysis was carried out using IFEFFIT [5] in ATHENA and ARTEMIS programs [6]. Here theoretical fitting standards were computed with ATOMS and FEFF6 programs [7, 8]. The brief theory for XAFS and basic principle for XAFS experiment is presented in the following Chapter.

References

[1] B. D. Cullity, *Elements of X-ray Diffraction*, Addison Wesley Publishing Co. USA (1956).

[2] A. J. Dekker, *Solid State Physics*, Prentice Hall Edition (1957).

[3] K. R. Priolkar, P. R. Sarode and N. Y. Vasanthacharya, CSIR Project Report, (2003).

[4] W. H. Macmaster, N. Kerr Del Grande, J. H. Mallet and J. H. Hubbell in *Compilation of X-ray Cross Sections*, Springfield, Virginia: National Technical Information Services, section II, revision 1 (1969).

[5] M. Newville, J. Synchrotron Rad. **8**, 322 (2001).

[6] B. Ravel and M. Newville, J. Synchrotron Rad. **12**, 537 (2005).

[7] B. Ravel, J.Synchrotron Rad. **8**, 314 (2001).

[8] S. I. Zabinsky, J. J. Rehr, A. Ankudinov, R. C. Albers and M. J. Eller, Phys. Rev. B **52(4)**, 2995 (1995).

Chapter 3

Fundamentals of X-ray Absorption Fine Structure

3.1 Introduction

X-ray absorption fine structure (XAFS) refers to the modulation of an atom's X-ray absorption probability due to the chemical and physical state of the atom. XAFS spectra are especially sensitive to the formal oxidation state, coordination chemistry and the distances, coordination number and the species of the atoms immediately surrounding the selected atom species. Because of this dependence, XAFS provides a practical and relatively simple way to determine the chemical state and local atomic structure for selected atomic species.

XAFS involves total absorption of an X-ray by an atom in condensed state. There is a dramatic increase in the probability for the absorption of an X-ray photon whose energy is equal to the binding energy of an electron compared to the absorption probability for an X-ray photon with slightly less energy. This increase in the absorption probability is referred to as an absorption edge. Every atomic electron has an associated absorption edge. To distinguish between the edges due to the excitation of an electron from the most tightly bound n = 1 shell and the next most tightly bound n = 2 shell, they are called the K-edge

and L-edge, respectively. Therefore every atom with at least three electrons has a K- and L-edge. These are the most commonly studied XAFS edges.

X-rays that are absorbed with energy greater than the binding energy of the electron may result in a photoelectron with some kinetic energy. If the kinetic energy of the electron is large compared to its interaction energy with the neighbouring atoms, the photoelectron is freed from the absorbing atom to the conduction band. Since this interaction energy is about 3 eV, the X-ray energy needs to be at least 15 eV above the edge energy to completely free the electron. The distinction between a photoelectron with energy greater than or less than 15 eV is important in determining the main source of XAFS. For this reason XAFS has been historically split into two regions: X-ray absorption near-edge structure (XANES) and the extended X-ray absorption fine structure (EXAFS). However, there is no clear demarkation between end of XANES region and beginning of EXAFS. Normally near edge structure extends upto 50 eV beyond the edge energy while, with recent theoretical advances, structure from 15 to 100's of eV beyond the edge energy can be considered as EXAFS [1]. Though both have the same physical origin, this distinction is convenient for the interpretation. XANES is strongly sensitive to the formal oxidation state and coordination geometry (e.g. octahedral, tetrahedral coordination) of the absorbing atom, while the EXAFS is used to determine bond distances, coordination number, and atomic species of neighbours of the absorbing atom.

Although XAFS phenomenon had been known since 1930's, the technique gained appreciation only after advent of synchrotron radiation and intense efforts in development of the theory for EXAFS with introduction of the Fourier transforms by Sayers *et.al* [2]. Since then, XAFS measurements have been extensively used to extract structural information.

Significant progress has been made in providing the analytical tools for EXAFS in the past decade which extends application of this technique to wide range of scientific fields including biology, environmental science, catalysts research and material science. Importantly, crystallinity is not required for XAFS and measurements can be made on elements of minority or trace abundance making the technique applicable to variety of systems. Several reviews and scholarly articles related to XAFS are found in literature (see for example, reference [3]).

3.2 The XAFS Phenomenon

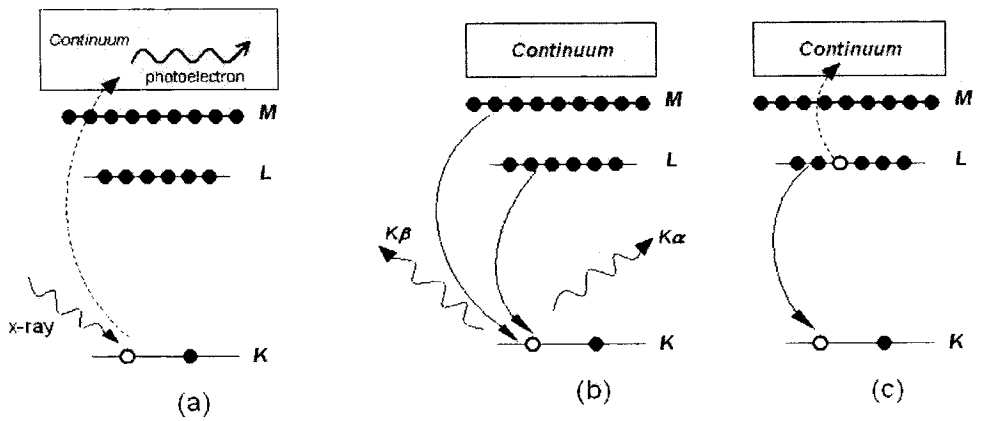

Figure 3.1: (a) The photoelectric effect in which an X-ray is absorbed and a core-level electron is promoted out of the atom. The decay of the excited state following an absorption event: (b) X-ray fluorescence and (c) Auger electron emission.

X-rays are light with energies ranging from $\sim$ 500 eV to 500 keV. At this regime, light is absorbed by all matter through the *photoelectric effect*. An X-ray photon is absorbed by an electron in a tightly bound quantum core level of an atom. If the energy of the incident X-ray photon is less than the binding energy, the electron does not get perturbed from its quantum state and no absorption takes place. If the X-ray photon energy exceeds the binding energy, the electron may be removed from its quantum level. In such a process, the X-ray is

said to be absorbed and any energy in excess of the electronic binding energy is given to a photoelectron that is ejected from the atom. This process is demonstrated schematically in Fig. 3.1(a).

The probability that the X-rays will be absorbed by the sample depends on the *absorption coefficient* μ, sample thickness t, and given by Beer's law as,

$$I = I_0 e^{-\mu t} \tag{3.1}$$

where I_0 and I are the X-ray intensities incident on, and transmitted through the sample respectively.

An XAFS measurement is simply a measure of the energy dependence of μ at and above the binding energy of the known core-level of the known atomic species. Since every atom has core-level electrons with well-defined binding energies, we can select the element to be probed by tuning the X-ray energy to an appropriate absorption edge. These absorption edge energies are well-known and vary with atomic number approximately as Z^2. With the development of synchrotron radiation beamlines almost all elements can be probed with X-ray energies ranging from the soft X-ray (photon energy 300 eV) to hard X-ray region (300 keV). Because the element of interest is chosen in the experiment, XAFS is *element specific*.

Following an absorption event, the atom is left in an excited state with a core-hole and any excess energy from the X-ray is given to the ejected photoelectron. The excited state eventually decays typically within 10^{-15} seconds of the absorption event. There are two mechanisms for decay of the excited state: X-ray fluorescence and Auger electron emission. In X-ray fluorescence, the excited core-hole will relax back to a ground state of the atom when a higher energy level (L or M shell) core electron drops into the core-hole, ejecting an X-ray

of well-defined energy. Such an emission occurs at discrete energies that are characteristic of the absorbing atom, and can be used to identify the absorbing atom. In the second process for de-excitation of the core-hole, the Auger effect, an electron drops from higher electron level and a second electron is emitted into the continuum. Both the processes of decay are presented in Fig. 3.1(b) and (c) respectively.

XAFS can be measured either in transmission or fluorescence geometry. The energy dependence of the absorption coefficient $\mu(E)$ for transmission mode can be

$$\mu(E) = ln(I_0/I) \tag{3.2}$$

or for X-ray fluorescence mode,

$$\mu(E) \propto I_f/I_0 \tag{3.3}$$

where I_0 refers to the incident intensity and I_f is the intensity of the fluorescence line.

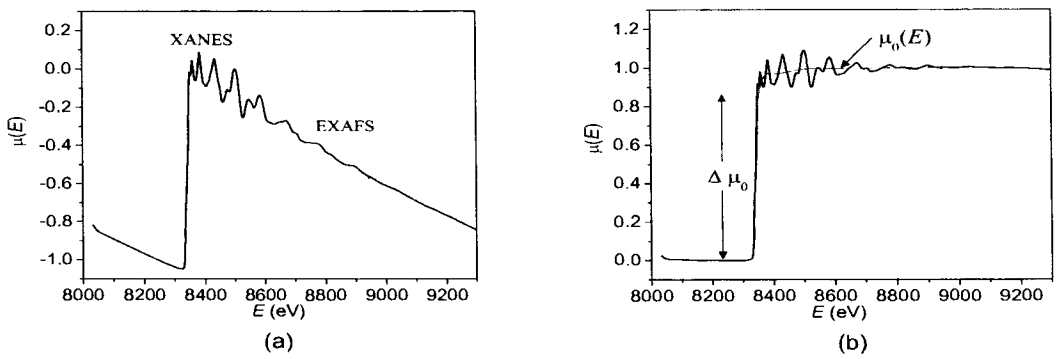

Figure 3.2: (a) The experimentally measured XAFS $\mu(E)$ for Ni metal. The XANES and the EXAFS regions are identified. (b) The normalized $\mu(E)$ with smooth background function $\mu_0(E)$ and the edge step $\Delta\mu_0$.

A typical XAFS spectrum is shown in Fig. 3.2. The sharp rise in $\mu(E)$ at the absorption edge is clearly visible in the spectra, as are the oscillations in $\mu(E)$ that represents the XAFS.

The two distinct regimes viz. XANES and EXAFS are identified in the figure. As EXAFS comprises of the oscillations well above the absorption edge, fine structure function $\chi(E)$ can be defined as,

$$\chi(E) = \frac{\mu(E) - \mu_0(E)}{\Delta\mu_0(E)} \tag{3.4}$$

where $\mu(E)$ is the measured absorption coefficient, $\mu_0(E)$ is a smooth background function representing the absorption of an isolated atom, and $\Delta\mu_0$ is the measured jump in the absorption $\mu(E)$ at the threshold energy E_0.

It is common to convert the X-ray energy to k, the wave number of the photo-electron, which has dimensions of 1/distance and is defined as

$$k = \sqrt{\frac{2m(E - E_0)}{\hbar^2}} \tag{3.5}$$

where E_0 is the absorption edge energy and m is the electron mass. The primary quantity for EXAFS is then $\chi(k)$, the oscillations as a function of photo-electron wave number. $\chi(k)$ is often referred to simply as the " EXAFS". As can be seen from Fig. 3.3, EXAFS is oscillatory and decays quickly with k. To emphasize the oscillations, $\chi(k)$ is often weighted by the power of k typically k^2 or k^3.

The different frequencies apparent in the oscillations in $\chi(k)$ correspond to different near-neighbour coordination shells which can be described and modeled according to the EXAFS Equation,

$$\chi(k) = \sum_j \frac{N_j e^{-2k^2{\sigma_j}^2} e^{-2R_j/\lambda(k)} f_j(k)}{k{R_j}^2} sin\left[2kR_j + \delta_j(k)\right] \tag{3.6}$$

where $f(k)$ and $\delta(k)$ are scattering properties of the atoms neighbouring the excited atom, N is the number of the neighbouring atoms present at distance R, and σ^2 is the disorder in

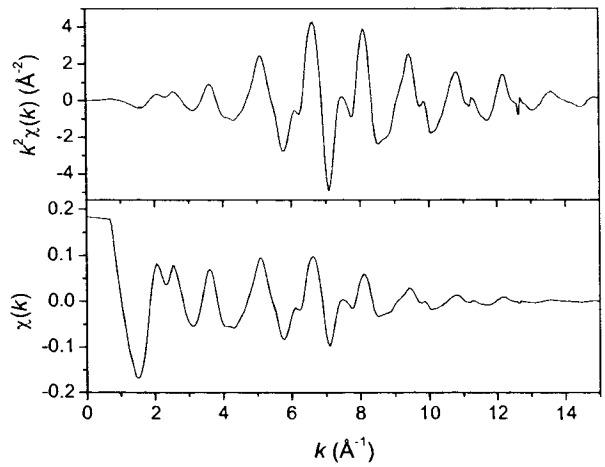

Figure 3.3: EXAFS extracted from $\mu(E)$ data for Ni metal, weighted by different powers of k. The figure illustrates how different powers of k emphasize the oscillations in different ranges of k.

the neighbour distance. The EXAFS equation allows us to determine N, R, and σ^2 knowing the scattering amplitude $f(k)$ and the phase-shift $\delta(k)$. Furthermore, since these scattering factors depend on the Z - atomic number of the neighbouring atoms, EXAFS is also sensitive to the atomic species of the neighbouring atoms.

3.3 A simple theoretical description of XAFS

The derivation of the XAFS equation presented below is very simple and can be understood intuitively. The idea of this heuristic approach has been described previously in [4, 5, 6, 7]. This section is meant to provide a feel of the XAFS process, the correlation to the physically measured quantity and the parameters obtained from the data analysis hence detailed mathematical treatment has been skipped. More general and sophisticated approaches can be found else where [1, 8, 9, 10, 11, 12, 13]. Besides a detail treatment of the theory of XAFS is beyond the scope of this thesis.

As mentioned in the previous section, XAFS is due to the photoelectric effect, in which an X-ray with energy equal to the binding energy is absorbed by the core-level electron, and a photoelectron with wave number k is created that propagates away from the atom. If the absorbing atom is isolated, for instance a monoatomic gas, the core electron is promoted to a continuum state. The absorption probability spectrum for this atom looks roughly like that shown in the Fig. 3.4. When neighbouring atoms are considered in this picture,

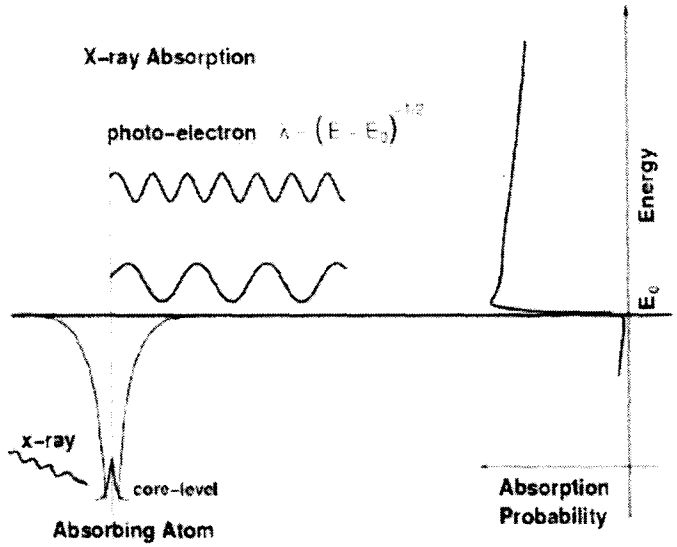

Figure 3.4: The absorption of X-ray with energy corresponding to the core level E_0, giving rise to a photoelectron that travels as a wave with wavenumber proportional to $\sqrt{E - E_0}$. The probability of absorption shows a sharp rise when the X-ray energy equals E_0.

the photoelectron can scatter from the neighbouring atom, and the scattered photoelectron returns to the absorbing atom. Considering the wave nature of the ejected photoelectron and regarding the atoms as point scatterers a simple picture can be formed in which the backscattered waves interfere with the forward wave to produce either peaks or troughs. A pictorial representation of such a process is shown in Fig. 3.5.

The interference between the outgoing and scattered part of the photoelectron at the

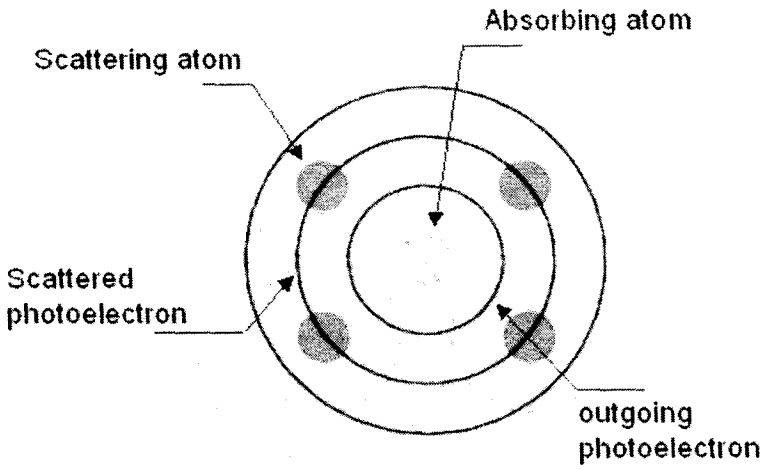

Figure 3.5: A schematic diagram of the radial portion of the photoelectron wave (solid lines) being backscattered by the neighbouring atoms (dotted lines).

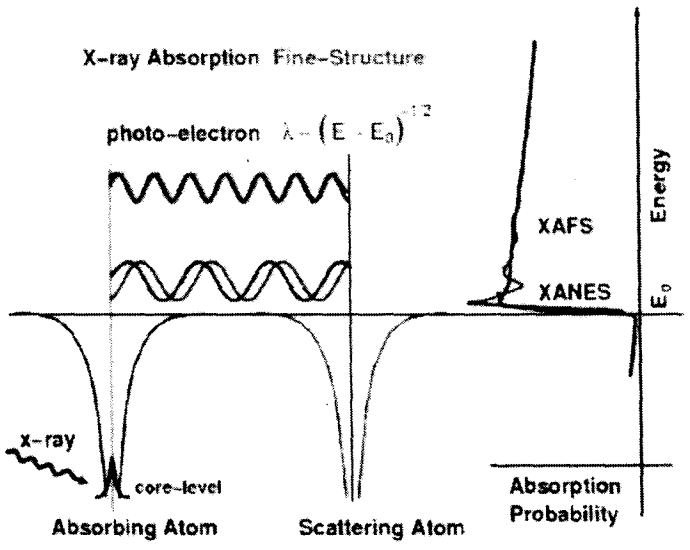

Figure 3.6: Modulation in the absorption coefficient $\mu(E)$ due to the scattering of photoelectron from neighbouring atoms. These modulations in the amplitude of photoelectron wave cause EXAFS.

absorbing atom modifies the photoelectron and hence the absorption probability profile. The smooth decaying function shown in Fig. 3.4 develops oscillatory fine structure as can be seen in Fig. 3.6.

This oscillatory structure can be isolated and analyzed to yield information about the local configurational environment within which the absorbing atom sits. This is the origin of XAFS.

The XAFS equation is developed using a slightly formal description of the simplistic picture described above. Since X-ray absorption is a transition between two quantum states, $\mu(E)$ can be described with *Fermi's Golden Rule*:

$$\mu(E) \propto |\langle i \mid \mathcal{H} \mid f \rangle|^2 \tag{3.7}$$

where $\langle i \mid$ represents the initial state , $\mid f\rangle$ is the final state and $\mathcal{H}$ is the interaction term. Since the core-level electron is tightly bound with the absorbing atom, the initial state will not be altered by the presence of the neighbouring atom. Whereas, the final state will be affected by the environment. Thus $\mid f\rangle$ can be expanded in two parts, one that is the "bare atom" portion ($\mid f_0\rangle$), and one that is the effect of the neighbouring atom ($\mid \Delta f\rangle$) as,

$$\mid f\rangle = \mid f_0\rangle + \mid \Delta f\rangle \tag{3.8}$$

We can expand Eq. 3.7 to

$$\mu(E) \propto |\langle i \mid \mathcal{H} \mid f_0\rangle|^2 \left[1 + |\langle i \mid \mathcal{H} \mid \Delta f\rangle \frac{\langle f_0 \mid \mathcal{H} \mid i\rangle^*}{|\langle i \mid \mathcal{H} \mid f_0\rangle|^2} + C.C.\right] \tag{3.9}$$

where $C.C.$ means complex conjugate. Recall the relationship between $\mu(E)$ and $\chi(E)$ given at Eq.3.4,

$$\mu(E) = \mu_0(E)[1 + \chi(E)] \tag{3.10}$$

We can now assign $\mu_0 = |\langle i \mid \mathcal{H} \mid f_0 \rangle|^2$ as the "bare atom absorption", which depends only on the absorbing atom - as if the atom was isolated. We can also see the the fine-structure χ can be written as

$$\chi(E) \propto |\langle i \mid \mathcal{H} \mid \Delta f \rangle \tag{3.11}$$

The interaction term $\mathcal{H}$ represents the process of changing between two energy or momentum states and can get tricky. For the purposes here, this reduces to a term that is proportional to $e^{ik\cdot r}$. The initial state is tightly bound core-level, which can approximate as delta function (a $1s$ level for atomic number Z extends to around a_0/Z, where $a_0 \sim 0.529$ Å is the Bohr radius). the change in final state is just the wave-function of the scattered photo-electron, $\psi_{scatt}(r)$. Putting all the terms together, we get a simple expression for the EXAFS:

$$\chi(E) \propto \int dr \delta(r) e^{ik\cdot r} \psi_{scatt}(r) = \psi_{scatt}(0) \tag{3.12}$$

In other words, this simply states that the EXAFS $\chi(E)$ is proportional to the amplitude of the scattered photo-electron at the absorbing atom.

We can further evaluate the amplitude of the scattered photo-electron at the absorbing atom, to get the EXAFS equation. The outgoing photoelectron wave-function $\psi(k, r)$ traveling as a spherical wave,

$$\psi(k, r) = \frac{e^{ik\cdot r}}{kr} \tag{3.13}$$

travels a distance R to the neighbouring atom, gets scattered from the neighbouring atom, and travels the same distance R back to the absorbing atom. We multiply all these factors together to get,

$$\chi(k) \propto \psi_{scatt}(k, r = 0) = \frac{e^{ik\cdot R}}{kR} \left[2kf(k)e^{i\delta(k)}\right] \frac{e^{ik\cdot R}}{kR} + C.C. \tag{3.14}$$

where $f(k)$ and $\delta(k)$ are scattering properties of the neighbouring atom. As mentioned before, these scattering factors depend on the Z of the neighbouring atom which makes EXAFS sensitive to the atomic species of the neighbouring atom. Combining these terms and including the complex conjugate, we get,

$$\chi(k) = \frac{f(k)}{kR^2} sin\,[2kR + \delta(r)] \tag{3.15}$$

The treatment here involved one pair of absorbing atom and scattering atom. For a real measurement, we need to average over a large number of atom pairs. Even for neighbouring atoms of the same type, the thermal and static disorder in the bond distances will give a range of distances that will affect XAFS. As a first approximation, this disorder will change the XAFS equation to

$$\chi(k) = \frac{Ne^{-2k^2\sigma^2} f(k)}{kR^2} sin\,[2kR + \delta(k)] \tag{3.16}$$

where N is the coordination number and σ^2 is the mean-square-displacement in the bond distance R. Most real systems have more than one type of neighbouring atoms around the absorbing atom. This is easily accommodated in the above expression by considering the sum of such contributions from each scattering atom type, often termed as - *coordination shell* or *coordination sphere* (the term *scattering path* is also used). Equation. 3.16 can now be written as,

$$\chi(k) = \sum_j \frac{N_j e^{-2k^2{\sigma_j}^2} f_j(k)}{k{R_j}^2} sin\,[2kR_j + \delta_j(k)] \tag{3.17}$$

where j represents the individual coordination shell of identical atoms at approximately the same distance from the central absorbing atom. In principle there could be many such shells, but shells of similar Z come close enough, making it difficult to distinguish one from another.

When we made the most important approximation that the outgoing photoelectron travels as a spherical wave (at Eq. 3.13), we neglected the fact that the photoelectron can also scatter inelastically. The conduction electrons, phonons etc can give rise to inelastic scattering. Because XAFS is a direct measure of the interference between the original photoelectron and the scattered part of the photoelectron wave, the degradation of the wave due to inelastic scattering destroys its coherence and therefore the XAFS signal. This is interpreted as a finite lifetime of the photoelectron. The lifetime of the core hole depends on the atomic species and the photoelectron shell. In general, the core hole exists for about 10^{-15} seconds before it is re-populated [14]. The net effect of the finite core hole lifetime and the finite lifetime of the photoelectron is an exponential decay of the XAFS signal. We therefore bring in the expression for a damped spherical wave,

$$\psi(k,r) = \frac{e^{ik\cdot r}e^{-2r/\lambda(k)}}{kr}, \tag{3.18}$$

as the photoelectron wave-function where λ is the mean-free-path of the photoelectron. The mean-free-path is typically 5 to 30 Å and has a significant but fairly universal dependence on k. Including the $\lambda(k)$, the EXAFS equation becomes

$$\chi(k) = \sum_j \frac{N_j e^{-2k^2{\sigma_j}^2} e^{-2R_j/\lambda(k)} f_j(k)}{k{R_j}^2} sin\left[2kR_j + \delta_j(k)\right] \tag{3.19}$$

Another important addition to the XAFS Eq. 3.19 is the ${S_0}^2$ term, usually called the passive electron reduction factor [18]. Many EXAFS analysis methodologies also refer to it as the amplitude reduction factor. Its value is completely determined by the absorbing atom. It essentially means the relaxation of the remaining electrons in the absorbing atom after the creation of the core hole. The net effect of these passive electrons is to attenuate

the XAFS signal. Values of ${S_0}^2$ therefore, range from 0.7 to 1.0 where 1.0 represents the fully screened potential.

In the final form, the XAFS equation is written as,

$$\chi(k) = \sum_j \frac{N_j {S_0}^2 e^{-2k^2{\sigma_j}^2} e^{-2R_j/\lambda(k)} f_j(k)}{k{R_j}^2} sin\left[2kR_j + \delta_j(k)\right] \tag{3.20}$$

From this equation, we can draw a few physical conclusions about XAFS. First, because of the $\lambda(k)$ term and the R^{-2} term, XAFS is seen to be inherently *local probe*, not able to see much further than 5Å or so from the absorbing atom. Second, the XAFS oscillations will consist of different frequencies that correspond to the different distances for each coordination shell. This will lead us to use Fourier transforms in the analysis. Finally, in order to extract the distances and coordination numbers, we need to have accurate values for the scattering amplitude and phase-shifts $f(k)$ and $\delta(k)$. This is a crucial issue in EXAFS analysis and needs to be evaluated accurately. Besides, many experimental systems also require consideration of atoms beyond the first shell. Here, the single scattering formulation of EXAFS is often insufficient and *multiple scattering* events gain due attention. Multiple scattering includes the scattering of the photoelectron from two or more of the surrounding atoms. In recent years there has been tremendous development in XAFS calculations and there are standard programs available viz. FEFF, GNXAS, EXCURVE that provide the calculated scattering factors for different absorbing atoms and also includes the code for multiple scattering events.

3.4 XAFS Data Handling

It is clear from all the above discussion that XAFS essentially requires a very good measure of $\mu(E)$. Any error in the measurement of $\mu(E)$ can degrade or even destroy the XAFS. Though the choice of the data collection mode (transmission /fluorescence) is highly dependent of the sample under study, the analysis is essentially the same for both the data collection strategies.

3.4.1 Data Reduction

The physically measured photon intensities are first converted to $\mu(E)$ by correcting for any systematic errors such as self-absorption and detector dead-time. A smooth pre-edge function is then subtracted from $\mu(E)$. The threshold energy E_0 is determined and $\mu(E)$ is normalized to go from 0 to 1. The post-edge background function is a smooth spline that is subtracted from the EXAFS region. From here on, the data-reduction procedure gets most error-prone. Background removal if not carried out judiciously, can destroy the EXAFS itself. It is important to mention that XAFS is a band-limited phenomenon, with a finite k- and R-range. Having isolated the EXAFS signal, the data is then Fourier transformed for analysis (refer Eqns. 3.4, 3.5) with very cautious selection of the range for transformation. The XAFS signal $\chi(k)$ is then k-weighted and Fourier transformed into R-space. The steps involved in data reduction are shown graphically in Fig. 3.2 and Fig. 3.3. These figures present the data for $7\mu m$ thick Ni-metal foil measured in transmission mode.

3.4.2 Data Modeling

Figure 3.7 presents a flowchart that outlines the entire procedure for data modeling and analysis of the XAFS experiment.

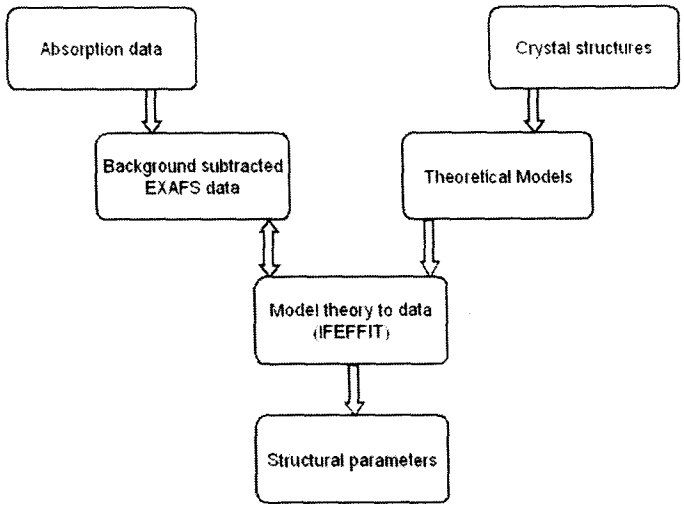

Figure 3.7: A flow-chart for XAFS data reduction and analysis.

In the present study, data analysis was carried out using ATHENA and ARTEMIS applets [15] that incorporates the IFEFFIT program [16] wherein theoretical fitting standards were computed with ATOMS and FEFF6 programs [10, 17] and fitting was done using FEFFIT program. The actual procedure for the data analysis adopted here is as follows.

The treatment to the measured $\mu(E)$ like normalization, background subtraction and changing to $\chi(k)$ form was carried out using the ATHENA applet which incorporates the AUTOBK program. The data in $\chi(k)$ v/s k form is then imported into the ARTEMIS applet that incorporates the programs like ATOMS, FEFF and FEFFIT. With the basic crystallographic information like space group, atoms type and their positions in the unit cell, and the lattice constants of a chosen structural model the ATOMS generates a input file for

FEFF calculations. FEFF program accurately calculates the effective scattering amplitudes $f(k)$ and phase shift $\delta(k)$ for different 'paths'. A Path is an abstract formalism for breaking the EXAFS into manageable pieces based on the scattering path that a photo-electron takes and conceptually it is very similar to actual scattering path or coordination sphere described in the earlier sections. The path formalism is a superior way to robustly analyze complex EXAFS data that includes the effects of multiple scattering.

Analysis in IFEFFIT consists of modeling $\chi(k)$ in terms of a sum of 'paths' with the XAFS contribution from each path being guided by calculation from FEFF. IFEFFIT relies on FEFF for basic information about all of its paths. This means that you need to run FEFF and sort through its results prior to defining paths with IFEFFIT. The outputs of FEFF that IFEFFIT needs is the set of feffnnnn.dat files, where each file represents the result for a single path. Once FEFF has run and a set of '`feffnnnn.dat`' files exists, they can be used within IFEFFIT. A special '`path()`' command is used to define paths within IFEFFIT. The `path()` command takes several optional arguments, known as '*path parameters*' that represent the parameters used to modify the EXAFS function for that path. The most important path parameters includes ${S_0}^2$, the amplitude reduction factor, δR, the change in path distance (and half-path-length for multiple scattering paths), σ^2- the mean-square displacement of the bond, and $e0$, the energy shift. Once defined, combining paths to give a $\chi(k)$ function is very easy. IFEFFIT allows to alter the paths through the *path parameters*, so that a sum of paths that best matches the data can be identified. The Fourier Transforms involved in the analysis procedure provides a flexibility of viewing the fit in R space and hence judge the quality of the fit. The Fourier transform parameters can be read from the program variables

viz. $kmin, kmax, kweight, dk1, dk2$. Like the Fourier transform parameters, the R-range can be set from program variables $(rmin, rmax)$. When analyzing the data in R space, the full complex XAFS $\chi(R)$ should be viewed and not just the magnitude $|\chi(R)|$. Using R space, helps in fitting one coordination shell at a time and ignore the others. When analyzing the data, however, it is instructive to also look at the "best-fit" in the k-space.

A fit is not very useful without some idea of the reliability of the fit and some estimate of the uncertainty in the fitted variables. The program automatically calculates the estimated uncertainties and goodness-of-fit parameters that help to judge whether a fit is taking far too many iterations, indicating a problem with the set up or starting model. The amount of information we can get out of XAFS measurements is given as $2\Delta k \Delta R/\pi + 1$, for fitting a k-range (Δk) and R-range (ΔR) and can be stored as N_{idp} - number of independent points in the fit. The '1' represents the constant term in the Fourier series expansion. The estimated uncertainty in the data itself is stored in the variables ε_r - for the uncertainty in the data $\chi(R)$ and ε_k - for the uncertainty in the data $\chi(k)$. The main goodness-of-fit statistics are $R - factor$, χ^2, and $\chi^2_{reduced}$, which are three different ways of scaling the sum-of-squares of the final misfit. $R - factor$ is the misfit scaled to the data itself, so it is a relative misfit, χ^2 is scaled to the estimated uncertainty in the data (ε_r for data fit in R-space). $\chi^2_{reduced}$ is χ^2 divided by the number of "free parameters in the fit", given by the difference of n_{idp} and n_{varys} (or number of variables). For each fitting variable, IFEFFIT creates a variable named $\Delta(VAR)$, and writes the estimated uncertainty for variable VAR to this variable. For example, $\Delta({S_0}^2)$, $\Delta(e0)$, $\Delta(\sigma^2)$, and $\Delta(\delta R)$.

To summarize the above analysis procedure in short, IFEFFIT has four basic require-

ments: $\chi(k)$ data to fit, a list of paths to sum over and make the model XAFS, Fourier transform and fit range parameters, and one or more variables defined that can be varied so as to affect the model XAFS.

Finally a carefully designed experiment with a good experimental practice for making sample absorbers and well constructed fitting models with a good physical intuition make for excellent EXAFS analysis.

3.5 Example: Ni-metal

Data Reduction to $\chi(k)$ form

$\mu(E)$ Vs. E was recorded in transmission mode for pure nickel metal foil of $7\mu m$ thickness. The raw data is presented in the Fig. 3.8. This data has to be reduced to standard $\chi(k)$ form as described in the previous sections. For this, pre-edge and the post-edge lines are subtracted from the the raw data (see Fig. 3.8). E_0, is identified as the first peak in the spectrum of derivative of $\mu(E)$ Vs. E. Normalized $\mu(E)$ alongwith estimated background

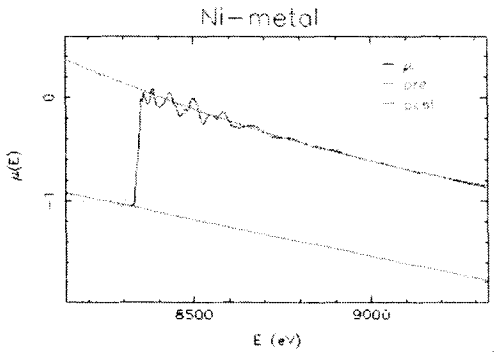

Figure 3.8: The raw $\mu(E)$ data recorded for Ni metal showing the pre-edge and the post-edge lines that are to be subtracted from the data.

function μ_0 are shown graphically in Fig. 3.9(a). The data is transformed to $\chi(k)$ form using the relationship between $\mu(E)$ and $\chi(E)$ given at Eq.3.4, 3.5. The EXAFS spectrum thus

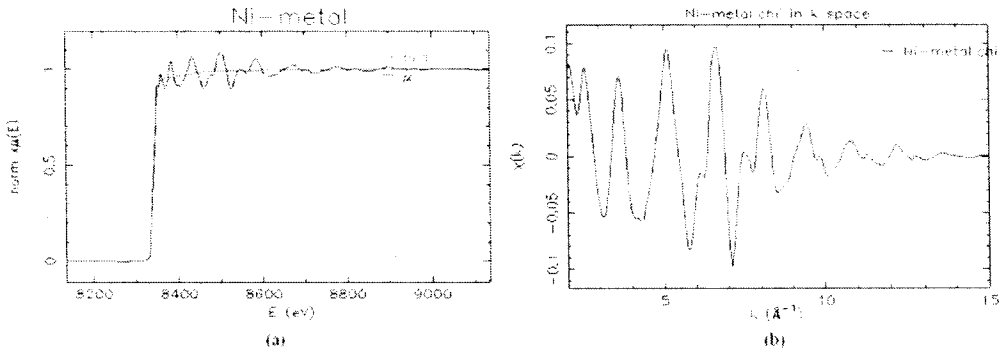

Figure 3.9: (a) The normalized $\mu(E)$ with background function $\mu_0(E)$. (b) Plot of corresponding EXAFS in $\chi(k)$ Vs. k form.

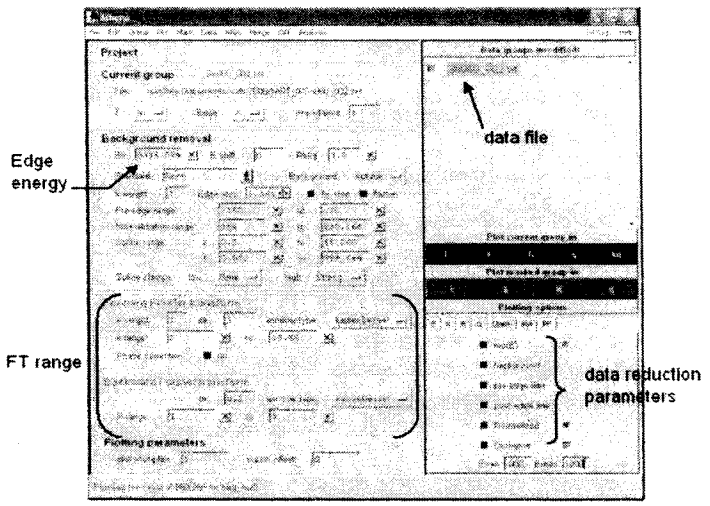

Figure 3.10: The ATHENA applet: incorporates the data reduction strategy to obtain data in $\chi(k)$ form.

obtained looks like as that shown in Fig. 3.9(b). All the above steps are achieved through the ATHENA applet, pictorial representation of this is shown in Fig.3.10.

Data Analysis and Fitting

Once the data is transformed to the desired form, $\chi(k)$, fitting is carried out through the ARTEMIS applet. The screen shot of ARTEMIS is shown in the Fig. 3.11. Before going ahead with the analysis, we need to revise the system under investigation and the possible outcomes from the XAFS data. This is a very important step in XAFS data analysis because

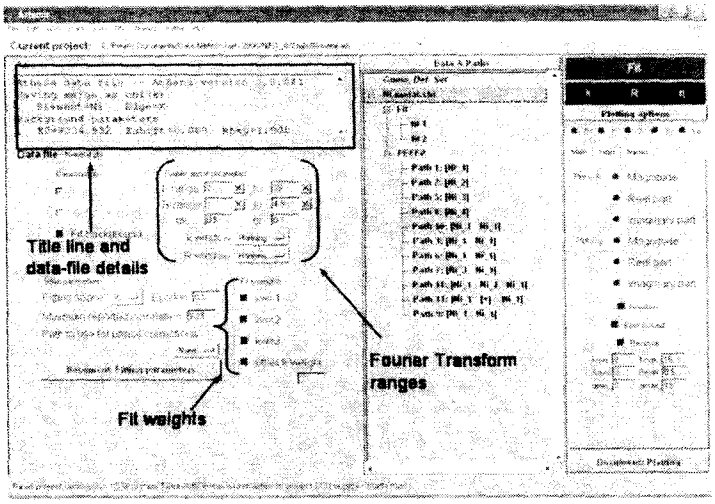

Figure 3.11: The ARTEMIS applet: incorporates the IFEFFIT program for XAFS data analysis.

a good physical intuition about the system is what decides the physical significance of the results of the final analysis. In the present case, we know that Ni has a face-centered cubic (FCC) structure with *Fm3m* space group and lattice parameter a= 3.58Å. Based on this information FEFF generates all possible scattering paths and their respective percentage contribute to the total XAFS for Ni metal. These include scattering paths which result due to interaction between the absorber atom and **one** back scattering atom (single scattering path - SS) and due to interaction between **more than one** back scattering atoms (multiple scattering path - MS). Usually, only those paths that provide a maximum contribution (> 10%) to the total XAFS are selected. This condition essentially includes all the SS paths. Amongst the MS paths, the non-linear ones have a weak contribution in comparison to the the linear MS paths. Infact, some linear MS are equally strong if not more in contribution to XAFS as compared to a SS path. With this condition as a guide for the proper choice of path selection, we once again look at the structural model for Ni metal. A schematic of one of the planes of cubic Ni is shown in Fig. 3.12. The paths that describe the backscattering

of photoelectron wave from the neighbouring atoms through SS and MS events are shown. Consider the atom marked '1' as the absorbing atom, a few scattering events can be listed as:

i) $1 \rightarrow 2 \rightarrow 1$ SS path,

ii) $1 \rightarrow 3 \rightarrow 1$ SS path,

iii) $1 \rightarrow 2 \rightarrow 3 \rightarrow 1$ MS path,

iv) $1 \rightarrow 2 \rightarrow 3 \rightarrow 2 \rightarrow 1$ MS path,

v) $1 \rightarrow 4 \rightarrow 1$ SS path,

vi) $1 \rightarrow 2 \rightarrow 4 \rightarrow 1$ MS path,

vii) $1 \rightarrow 2 \rightarrow 4 \rightarrow 2 \rightarrow 1$ MS path,

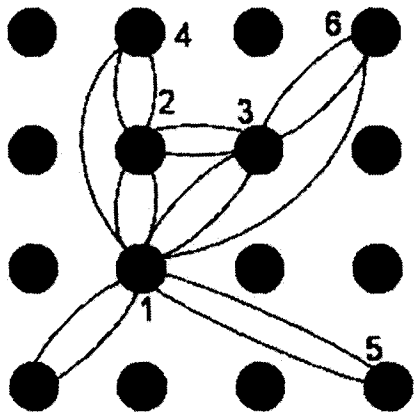

Figure 3.12: Schematics of the portion of plane of atoms in cubic Ni. The different SS and MS paths along which the photoelectron wave gets backscattered are depicted.

To further emphasize the contribution of each of such scattering paths to the total XAFS, we see Fig. 3.13 that shows how the sum of these chosen SS and MS form the total XAFS in R-space. It is seen that the contribution to the 1^{st} peak in R space is entirely from the

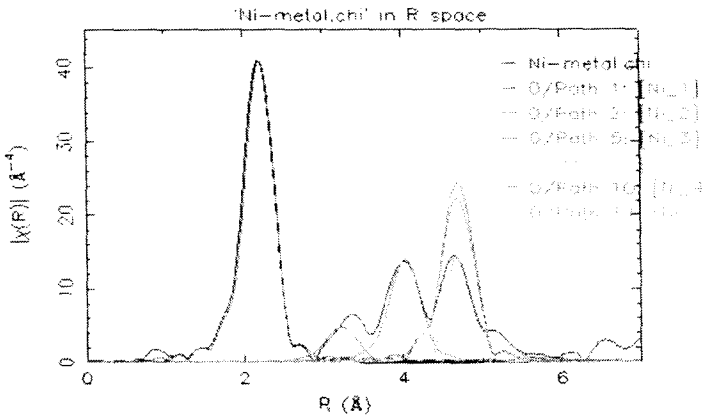

Figure 3.13: Ni XAFS in R space. The first three peaks are entirely due to the 1^{st}, 2^{nd} and 3^{rd} neighbour shells respectively, while, the 4^{th} peak has contributions from SS and MS paths.

Table 3.1: A list of typical path parameters described in XAFS analysis program.

keyword	symbol	Description	Status
`path`		The name of the particular path	
`id`		A text string describing the path	
`amp`	$S_0{}^2$	varied only once	set
`N`	N	Coordination No. ; varied rarely	set
`enot`	E_0	A shift of the energy reference;	
		varied only once	set
`dr`	ΔR	A change in the total path length;	
		constantly evaluated	guess/ set
`ss`	σ^2	constantly evaluated	guess/ set
`third`	C_3	A third cumulant about the path length	
`fourth`	C_4	A fourth cumulant about the path length	
`ei`	E_i	A change in the effective mean free path	

nearest neighbour scattering path ($1 \rightarrow 2$). The next-near neighbour shell ($1 \rightarrow 3$) gives rise to the 2^{nd} peak and so on. The 4^{th} peak in R space has several contributions and it is a sum of several MS paths contained in a SS path (for eg.$1 \rightarrow 6$, $1 \rightarrow 3 \rightarrow 6$). Thus it is demonstrated here that the total XAFS is a sum of all such paths and that the MS paths needs to be given equal importance in fitting the XAFS.

Once the choice of suitable paths is made, it can be incorporated in IFEFFIT by defining

Table 3.2: Results of the fit to the Ni metal data. The fittings were carried out in k range: (2-15)Å^{-1} with k-weight: 3 and R range: (1-5)Å. Figures in parentheses indicate uncertainty in the last digit. $\chi^2 = 0.027$; $Reduced\chi^2 = 0.0011$; $R - factor = 0.0177$

$S_0{}^2 = 0.82(5)$		$e_0 = 6.34(7)$
Atom and Coord. No.	Bond Length R (Å)	σ^2 (Å^2)
Ni2 × 12	2.486(3)	0.0063(4)
Ni3 × 6	3.515(3)	0.009(1)
Ni4 × 24	4.306(3)	0.0087(7)
Ni6 × 12	4.972(3)	0.0029(6)
MS[a] × 24	4.972(3)	0.0063(6)
MS[b] × 12	4.972(3)	0.0063(6)

[a] Ni1→Ni3→Ni6→Ni1
[b] Ni1→Ni3→Ni6→Ni3→Ni1

a set of certain path parameters for each path. The list of such parameters for the first path used in the present analysis is given in Table. 3.1. In the process of fitting, path parameters are varied and a suitable fit is obtained. However, some of the path parameters are varied only once at the beginning of the fit and kept fixed thereafter. In ARTEMIS, the commands like `guess, def, set` are used to assign such status to each parameter. The parameters that are varied only once and kept fixed thereafter are said to be `set`. The parameters whose value is constantly varied in the fit process can have status as `guess` when varied and `set` when kept fixed. There are certain parameters that are universal to all the paths and their status is given as `def` which means the value is 'defined'. Inclusion of such universal parameters depends highly on the model being fit. The path parameters for different paths can also be correlated to each other.

Figure 3.14 presents the fit for Ni analysis in the R space and back transformed k space. The varied parameters and the final values are listed in the Table 3.2. It is seen from the figure that the fit is quite satisfactory and the values presented in the table are realistic.

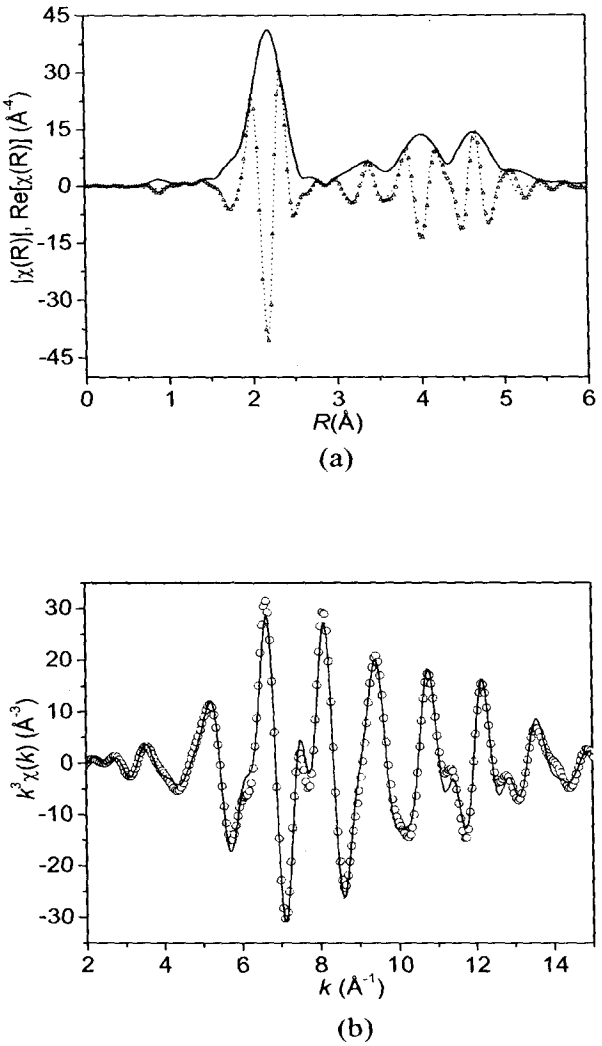

Figure 3.14: (a)k^3 weighted, FT EXAFS spectra in R space and (b) real component of FT in the back transformed k space for Ni metal.

References

[1] J. J. Rehr, R. C. Alber, C. R. Natoli and E. A. Stern, Phys. Rev. B. **34(6)**, 4350 (1986).

[2] D. E. Sayers, E. A. Stern and F. W. Lytle, Phys. Rev. Lett. **27**, 1204 (1971).

[3] D. C. Koningsberger and R. Prins Eds. *X-ray Absorption: Principles, Applications, Techniques of EXAFS, SEXAFS and XANES*, John Wiley and Sons, NY, (1989).

[4] E. A. Stern, Comp. Phys. Comm. **19(4)**, 289 (1978).

[5] Matthew Newville, *Fundamentals of XAFS* at `http://xafs.org`

[6] Bruce D. Ravel, Ph.D Thesis titled *Ferroelectric Phase Transitions in Oxide Perovskites Studied by XAFS*, University of Washington (1997).

[7] Shelly D. Kelly, Ph.D Thesis titled *XAFS study of the pressure induced B1 → B2 phase transition*, University of Washington (1999).

[8] C. A. Ashley and S. Doniach, Phys. Rev. B. **11(4)**, 1279 (1975).

[9] P. A. Lee and J. B. Pendry, Phys. Rev. B. **11(8)**, 2795 (1975).

[10] S. I. Zabinsky, J. J. Rehr, A. Ankudinov, R. C. Albers and M. J. Eller, Phys. Rev. B. **52(4)**, 2995 (1995).

[11] S. J. Gurman, N. Binstead and I. Ross, J. Phys. C: Solid State Phys. **17**, 143 (1984).

[12] S. J. Gurman, N. Binstead and I. Ross, J. Phys. C: Solid State Phys. **19**, 1845 (1986).

[13] A. Filliponi, A. Di. Cicco and C. R. Natoli, Phys. Rev. B. **52**, 15122 (1995).

[14] O. Keski-Rahkonen and M. O. Krause, *Atomic Data and Nuclear Data Tables*, **14** 139-146, (1974).

[15] B. Ravel and M. Newville, J. Synchrotron Rad. **12** 537 (2005).

[16] M. Newville, J. Synchrotron Rad. **8** 322 (2001).

[17] B. Ravel, J.Synchrotron Rad. **8**, 314 (2001).

[18] J. J. Rehr, E. A. Stern, R. L. Martin and E. R. Davidson, Phys. Rev. B. **17**, 560 (1978).

Chapter 4

Structural, Magnetic and Transport properties of $Ni_{2+x}Mn_{1-x}Ga$

4.1 Introduction

A Mn-based Heusler alloy, Ni_2MnGa, experiences martensitic transformation in the ferromagnetic state. The temperatures of ferromagnetic (T_C = 370 K) and martensitic ($T_M \sim$ 220 K) transitions differ significantly for the stoichiometric composition. Any deviation from the composition allows a change of these characteristic temperatures. The crystal structure at high temperature is the cubic $L2_1$ and transforms into a modulated tetragonal state at low temperature [1, 2].

In the present work, a study of physical properties of $Ni_{2+x}Mn_{1-x}Ga$ alloys in the range $0 \leq x \leq 0.19$ has been performed. With a partial substitution of Mn with Ni there is an increase in T_M and a systematic decrease in T_C until both the temperatures coincide in the narrow concentration range x = 0.18 - 0.20 [3]. A fall in T_C can be understood based on the argument that with reduction in Mn content, the spatial distance between Mn atoms increases leading to decrease in exchange integral and hence weakening the magnetic interactions. The enhancement of T_M with respect to Ni substitution for Mn can be understood

in terms of increase in the electronic energy of the system due to increase in the conduction electron concentration. The perplexing part of this class of alloys is the anomalies observed in the vicinity of martensitic transition. Differently modulated intermediate structures are known to exist in-between the initial and the final phase with the variation of temperature [4]. Further, the low temperature crystal structure in Ni-Mn-Ga alloys is highly composition dependent and classification based on crystal periodicity like 5M (five layered), 7M (seven layered) or non-modulated(NM) tetragonal has been made [5]. An incomplete softening of the TA_2 phonon mode with displacement along the [110] direction marks the occurrence of *premartensitic* transition ($\sim$ 260 K) as evidenced by inelastic neutron scattering measurements [6, 7, 8]. A large softening of certain elastic constants $C' = \frac{1}{2}(C_{11} - C_{12})$ takes place at this intermediate transition [9]. The dependence of C' on applied magnetic field proves the magnetoelastic origins of these interactions [10]. Such a phonon softening is believed to be due to contribution from electron-lattice coupling and nesting of the Fermi surface [11]. The premartensitic transition is independent of composition and occurs only for alloys with $T_M \leq 270$ K [12, 13].

Martensitic phase transition in Ni_2MnGa is known to be driven by the band Jahn-Teller effect [14]. Hence, it can be presumed that the structural and magnetic transitions in $Ni_{2+x}Mn_{1-x}Ga$ alloys are manifested by the changes in the vicinity of Fermi surface. From electronic models of solids, the thermoelectric power (TEP) of an alloy is known to be the function of the electron concentration, the effective mass of the electron, and the electronic scattering factor. All of these are influenced by the relative concentration of the constituent elements, lattice strain, microstructural changes, material processing and phase change. As

Table 4.1: Elemental distribution in $Ni_{2+x}Mn_{1-x}Ga$ series as determined from EDX analysis, the valence electron concentration and the average value for T_M, T_C obtained from various measurements.

x	c/a	Ni	Mn	Ga	T_M	T_C	Crystal Structure
0	7.5	50.8	24.6	24.6	210K	370K	Cubic $L2_1$
0.05	7.54	51.0	24.7	24.3	250K	357K	Cubic $L2_1$
0.1	7.58	52.8	22.5	24.7	280K	342K	Modulated*
0.13	7.6	53.9	21.5	24.6	300K	342K	Orthorhombic (5M/7M)
0.16	7.62	54.4	21.2	24.4	315K	337K	Orthorhombic (5M/7M)
0.19	7.64	54.6	20.8	24.6	334K	334K	Orthorhombic (NM)

* T_M being close to room temperature, the cubic structure is highly unstable.

the Ni content increases at the cost of Mn in the Ni-Mn-Ga system, there is an increase in the temperature of martensitic phase transformation. Accompanying this change is the variation in the TEP, thus making it a valued property for the phase transformation and the associated microstructural studies. Further, in metallic alloys, the value and the sign of the thermoelectric power coefficient depends on the features of the electronic bands in the vicinity of the Fermi level. Thus, TEP measurements of $Ni_{2+x}Mn_{1-x}Ga$ should be very interesting as it would reflect the changes in the band structure occurring due to structural transformation when x is varied. The measurement of other properties like magnetic susceptibility, electrical resistivity, the gross crystal structure and microstructure of this series would hint towards very interesting interpretations.

With this aim, we present a comprehensive report of the structure, magnetic and transport properties of $Ni_{2+x}Mn_{1-x}Ga$ alloys in the range $0 \leq x \leq 0.19$. The starting alloy compositions and the corresponding elemental distribution as determined by energy dispersive x-ray analysis (EDX) are presented in Table 4.1. The average temperature for phase

transformations and room temperature crystal structure are also mentioned. The valence electron concentration e/a (electron per atom), calculated as the concentration weighted sum of the number of $3d$ and $4s$ electrons of Ni and Mn and the $4s$ and $4p$ electrons of Ga, is seen to increase systematically with increasing Ni concentration.

4.2 Structural Properties

4.2.1 Surface Morphology

Martensitic transformation proceeds via deformation of the high symmetry cubic structure to a low symmetry structure. For a cube, all of its crystallographic directions being equivalent, there is no preference to the direction of deformation. Upon phase transformation, for minimizing the free energy of the system, the accommodation effects generate different martensitic variants that are separated by twin interface of the habit planes. Such different kinds of energy-release are usually visible on the sample surface and indicate the twinned relationship for different alloy compositions. Complex structural and microstructural changes are associated with martensitic transformation taking place in $Ni_{2+x}Mn_{1-x}Ga$ as the system evolves from $L2_1$ to 5M, to 7M and finally to NM structure with increasing Ni content. The simultaneous nucleation and the sequential growth of different martensitic bands across the length of the sample in different Ni-Mn-Ga alloys were observed using Optical Microscopy and Scanning Electron Microscopy.

The room temperature optical micrographs recorded on the highly polished wafer surface of different alloy compositions are presented in Fig. 4.1. As $x = 0$ sample is in the austenitic phase (T_M values given in Table 4.1), no surface effects are seen here. The $x = 0.1$ sample surface clearly shows the nucleation and growth of the martensitic variants. The images in

the lower panel of Fig. 4.1 represent the surface morphology of $x = 0.13$ and 0.19 alloys. These alloy compositions are in the martensitic phase as evident from the surface relief due to martensite variants. The preferentially oriented variants on the polished wafer of $x = 0.13$ sample is that of a 7M modulated structure. While the relief seen in $x = 0.19$ sample indicates that the modulations to tetragonal structure are complete at room temperature and the structure resembles to that of a non-modulated type.

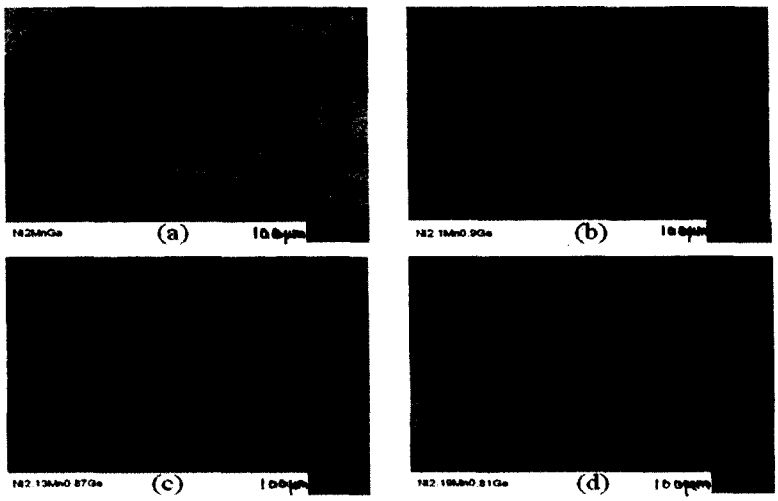

Figure 4.1: Optical microscopy images implicating different surface morphologies exhibited by (a) $x = 0$, (b) $x = 0.1$, (c) $x = 0.13$ and $x = 0.19$.

The microstructural transformations associated with evolution of martensitic structure change is best seen in $x = 0.1$ alloy. The T_M being very close to the room temperature, the austenitic phase is quite unstable in this alloy. The martensitic phase starts nucleating and there are regions where the two phases co-exist. Figure 4.2 shows these spatially distinct regions. The non-transformed region comprising of high temperature cubic phase can be seen on the right of the figure. While martensitic phase is seen to develop in the form of twinned plate-like structures. The martensitic structure itself is complex and two differently twinned

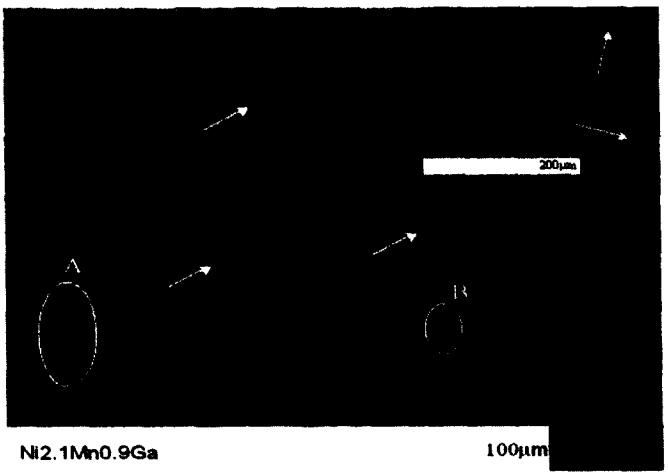

Figure 4.2: Optical microscopy image for $x = 0$ showing microstructural transformations associated with evolution of martensitic structure. The arrows indicate the magnetic Weiss domain boundaries and the regions marked A and B represents the 5M and 7M modulated structures respectively. The inset in the figure shows the magnified image shows the boundaries of twin domains.

modulated structures viz. 5M and 7M are seen as indicated in the figure. The magnetic Weiss domains for this class of alloys are usually 100-200 μm apart and run throughout the martensitic and austenitic regions without any break at the boundaries. Such magnetic domains are also seen clearly in Fig. 4.2, running across the sample and are indicated with arrows. As the martensitic transformation temperature is approached, different twin domains grow bigger in size. The growth of a particular twin domain is terminated by other twin domain with boundaries normal to each other. The inset of Fig. 4.2 shows a magnified image of $x = 0.1$ that clearly shows the boundaries of twin domains that are normal to each other. The SEM images are presented in Fig. 4.3. A similar inference as that obtained from optical micrograph can be made here. The apparent twin boundaries in the images with magnification contrast are interpreted as variants twinned on (110) and $(1\bar{1}0)$ planes. The surface morphology clearly shows the martensitic variants that can be attributed to the

differently modulated phases. The variants are of similar size and show a quite developed relief. The bright or the dark variants imply that they belong to a different twining system.

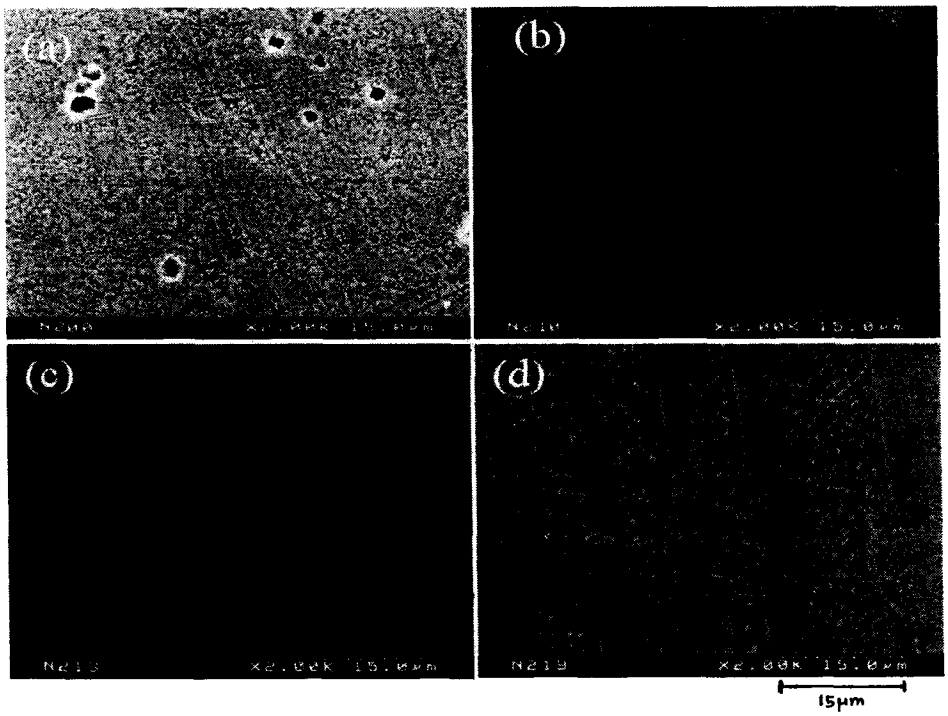

Figure 4.3: SEM images implicating different surface morphologies for (a) $x = 0$; (b) $x = 0.1$; (c) $x = 0.13$ and (d) $x = 0.19$.

It is seen that with increasing Ni replacing Mn in the series, the number of conduction electrons increases. The variation in the valence electron per atom ratio follows this trend.

4.2.2 X-ray Diffraction

Figure 4.4(a) shows the X-Ray diffraction profiles for Ni_2MnGa and $Ni_{2.19}Mn_{0.81}Ga$ taken at room temperature. The crystal structure for Ni_2MnGa is traditionally agreed to be that of the cubic $L2_1$ type in the austenitic phase with lattice parameter $a = 5.825$Å as determined from neutron diffraction studies by [1]. However, the $L2_1$ order is not clearly evident from the XRD profile due to similar atomic scattering factors for the constituent atoms; wherein

the reflections indicating the second neighbour ordering (characteristic of the $L2_1$ structure) is not found. For $Ni_{2.19}Mn_{0.81}Ga$, the (220) cubic reflection splits into two sharp and well separated peaks and the pattern can be indexed in tetragonal space group (I_4/mmm) with $a = 3.829$Å and $c = 6.523$Å .

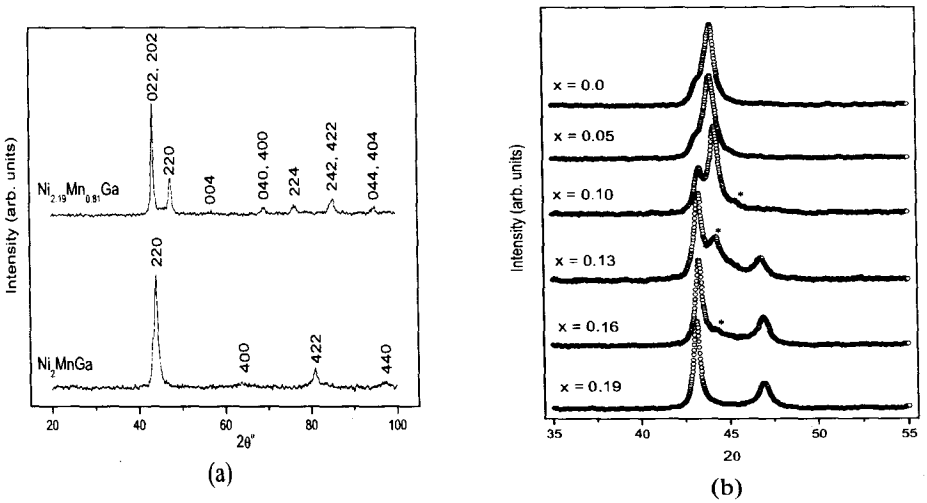

Figure 4.4: (a) XRD patterns of Ni_2MnGa and $Ni_{2.19}Mn_{0.81}Ga$. The pattern for Ni_2MnGa can be indexed to $L2_1$ structure while that of $Ni_{2.19}Mn_{0.81}Ga$ to a tetragonal structure. (b) XRD patterns scanned between 35° to 55°. The peaks marked with star-sign clearly indicates the modulated crystal structure of the corresponding composition.

Essentially, alloys with $x \leq 0.1$ are in the austenitic phase with T_M below room temperature, while those with $x \geq 0.13$ are present in the martensitic phase as T_M increasing systematically from 300 K to 334 K with increasing Ni content. The T_M and T_C and the crystal structure details are summarized in Table 4.1. With varying x, XRD profile for $Ni_{2+x}Mn_{1-x}Ga$ alloys show a systematic evolution from the cubic to modulated (5M/7M) to non-modulated (NM) martensitic structure. In order to closely observe these transformations, we focus on the main (220) cubic reflection of the $L2_1$ structure. The diffraction

pattern in this angular range (35° - 55°) were recorded at a slower scan speed of 0.5°/min. and are presented in Fig. 4.4(b). The XRD profiles indicate that the symmetry of the Ni-Mn-Ga structure is lowered with increase in x. As x increases from 0 to 0.1, a shoulder-like feature is seen to develop on the low angle side of (220) cubic reflection that grows in intensity. Such a feature can be attributed to be a signature of premartensitic phenomenon with unstable cubic structure. Upon martensitic transformation, this class of alloys undergo a tetragonal distortion of the type c/a < 1. For $x = 0.13$, there is a sudden rise in intensity of the shoulder peak (now forming the major peak) at the cost of the intensity of the peak corresponding to the (220) cubic reflection and a new peak emerges at $2\theta = 47°$. The peaks are quite broad and not well resolved that raises the possibility of some extra reflections between the two peaks. Such a pattern indicates that the martensitic transformation is not complete in this alloy and that the structure is of a modulated tetragonal type. Broad peak features are also evident for XRD pattern of $x = 0.16$ implying a modulated low temperature structure. The alloys with $x = 0.13$ to 0.19 can be indexed to c/a > 1 -type tetragonal structure.

4.3 Magnetic Properties: a.c. Susceptibility

Magnetic properties for the series were studied by carrying out the low field a.c. magnetic susceptibility (χ) measurements as a function of temperature in the warm-up cycle and the plots are shown in Fig. 4.5. The abrupt step-like features in χ are observed at phase transformation temperatures in all the samples. The onset of ferromagnetic transition is marked by a sharp rise in χ at T_C. The magnitude of χ remains constant with change in temperature until followed by a sharp fall at the martensitic transition temperature T_M.

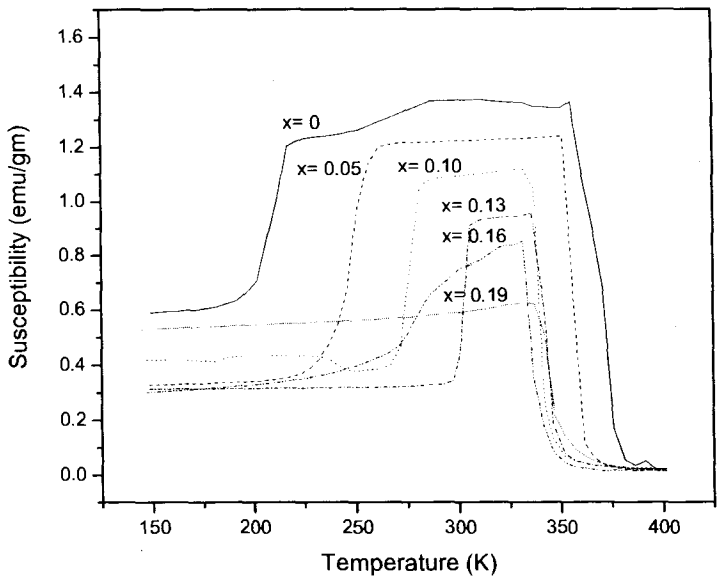

Figure 4.5: a.c. susceptibility as a function of temperature for $Ni_{2+x}Mn_{1-x}Ga$. The step-like features indicate the martensitic and ferromagnetic phase change at respective T_M and T_C for all the alloys. A premartensitic and intermartensitic transformations are evident for $x = 0$ and 0.1 alloys respectively.

As the Ni content increases across the series, the two transitions approach each other until they merge for $Ni_{2.19}Mn_{0.81}Ga$ at a temperature $\sim$ 330 K. A change in slope of χ at $\sim$ 270 K for the $x = 0$ sample is indicative of the premartensitic transition. These observations are in agreement with those reported in Ref.[3, 15]. In addition, a feature is observed in $x = 0.10$ at around T = 250 K. This feature occurs when the sample is in the martensitic phase (T_M = 285 K) hence can be interpreted to be due to intermartensitic transition from one crystallographically modulated structure to another [16]. The step-like feature in susceptibility for $x = 0.16$ is not very sharp as that for other members of the series. This can be due to the proximity of the two transition temperatures for this alloy.

4.4 Transport Properties

The X-ray diffraction patterns for Ni-Mn-Ga alloys showed that along with strong tetragonal reflections for $x = 0.19$, there were several unresolved additional peaks in the $x = 0.13$ and 0.16 samples that cause broadening of the XRD profiles. These observations are suggestive of modulated crystal structure for martensitic phase of these alloys. Further, studies in literature have established the existence of five- and seven-layered modulations of the martensitic phase for non-stoichiometric Ni_2MnGa alloys [5]. Besides, there exists temperature induced martensite -martensite phase change termed as *intermartensitic* transitions [4]. As compared to the martensitic transformation, these intermartensitic transitions have large (exceeding 100 K) temperature hysteresis and considerable difference in transport properties between the martensitic phases involved in the transition. Transport measurements of Ni-Mn-Ga alloys contain signatures indicative of the martensitic and ferromagnetic and intermartensitic transitions.

4.4.1 Four-Probe Resistivity

The four probe d.c. resistivity in the temperature range 100 - 375 K have been measured in the warming/cooling cycles and are presented in Fig. 4.6. At certain temperatures, a considerable change in slope with deviation in linear resistivity behaviour is evident from the plots. Further, there is a marked hysteresis between the warming/cooling runs. All these features carry information regarding the martensitic transitions. In $x = 0$, 0.05 and 0.1, the slope of R(T) changes at three different temperatures indicative of its martensitic, premartensitic and ferromagnetic transitions respectively. For $x = 0.13$ onwards, a pronounced jump in re-

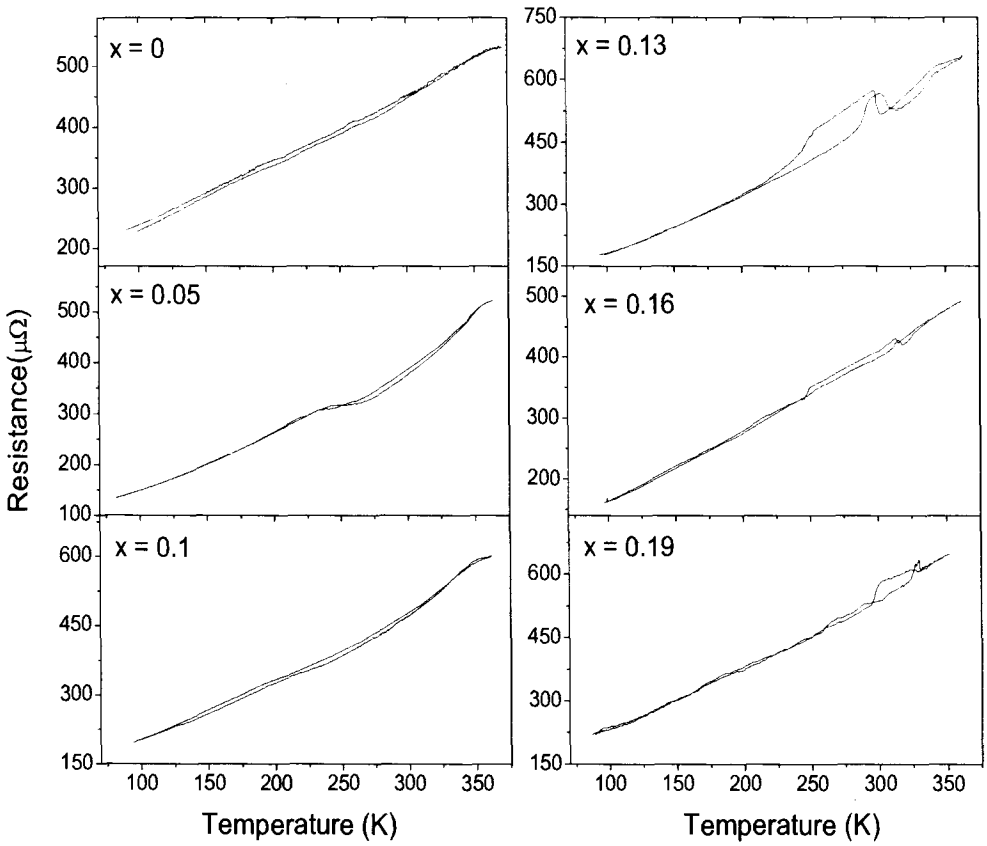

Figure 4.6: Resistance as a function of temperature for $Ni_{2+x}Mn_{1-x}Ga$.

sistance is seen at the T_M with huge hysteresis. The change in slope at higher temperature is indicative of ferromagnetic transition.

The peculiar difference in signatures attributed to martensitic transition in $x \leq 0.1$ and $x \geq 0.13$ alloys may be due to the occurrence of premartensitic transitions in the previous class of alloys. The softening of the TA_2 acoustic phonon mode that marks the occurrence of pre-martensitic phase, overrides the signatures due to martensitic transformation. Thus the anomaly at T_M is not as intense in $x \leq 0.1$ as compared to $x \geq 0.13$ alloys in which the

pre-martensitic transition is not observed.

The resistance variation for $x = 0.13$ is good example to illustrate the anomalies at the martensitic and ferromagnetic transformation with $T_M \sim 300$ K and $T_C \sim 340$ K. Another important feature in the resistance measurement is the hysteresis in the warming/cooling cycles that begins at temperature well above T_M and ends much after the martensitic transition has taken place. The origin of such difference can either be the changes in scattering probability or the changes in electronic structure. Since all the samples are known to show similar plate like morphology, the hysteresis cannot be accounted for by changes in scattering probability. Therefore the origin of such behaviour lies in the Fermi surface features. It is generally acknowledged that the long range ordering is associated with nesting properties of the Fermi surface as in case of spin- or charge- density wave [17]. As martensitic phases form with long-range ordering, it can be associated with the nesting properties of the Fermi surface with nesting vectors corresponding to the periodicity of the modulated crystal lattice. Thus martensitic phases with different modulations have different nesting vectors and hence share different fractions of the nested Fermi surface. Such a nesting considerably affects the transport properties of a metal due to the condensation of electrons in the nesting parts of the Fermi surface. An intermartensitic transformation means that there is a change in the modulation of the martensitic phase that affects the number of conduction electrons due to change in the Fermi surface available for conduction causing hysteresis in the martensitic phase.

4.4.2 Thermoelectric power

Phase transformation involves a change in the free energy and TEP being sensitive to such changes is expected to show signatures of martensitic as well as magnetic transition. Thermoelectric power of $Ni_{2+x}Mn_{1-x}Ga$ series was measured in the range 100 K to 350 K during warm-up and the data for all the samples is presented in Fig. 4.7(a) and (b).

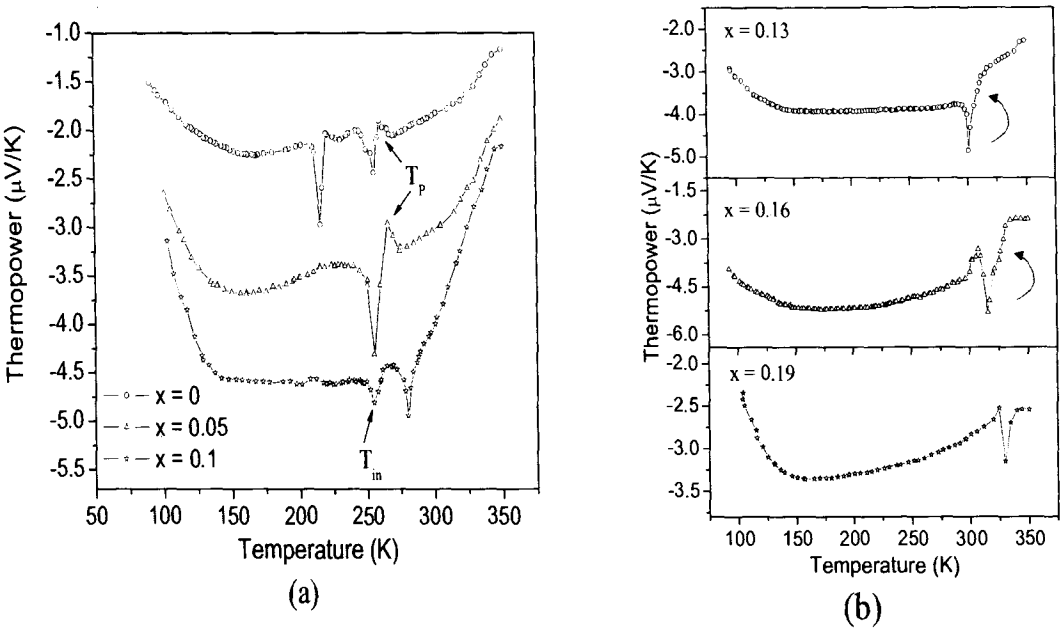

Figure 4.7: Thermopower as a function of temperature for $Ni_{2+x}Mn_{1-x}Ga$ with (a) $x = 0$, 0.05, 0.1 and (b) $x = 0.13$, 0.16, 0.19. The line connecting the points is guide to the eye. The features marked as T_P and T_{in} indicate the premartensitic and intermartensitic transitions respectively. The curved arrow points the drastic change in slope.

It has been shown in the past that the TEP for shape memory alloys show signatures corresponding to martensitic transition [18]. Indeed, as the sample is warmed a dip in TEP is obtained and can be associated with the strong phonon softening that is known to occur near the martensitic transition. On further warming a change in slope of TEP is seen due

to magnetic scattering of the charge carriers as T_C is approached. Thereafter, TEP attains almost a constant value that changes only slightly with temperature. This behaviour can be more clearly seen in $x \geq 0.13$. With prior knowledge of T_M and T_C for all the samples obtained from the magnetic susceptibility measurements, the anomalies seen in TEP data could be identified. As seen from Fig. 4.7(a), for $x = 0$ the first dip at $\sim$ 210 K is associated with its martensitic transformation. There is an additional anomaly occurring at $\sim$ 260 K marked as T_P in the figure. This feature is less intense to that occurring at T_M. A premartensitic transition is known to occur in Ni_2MnGa and its substitutional derivatives that have a martensitic transformation temperature below 260 K [12]. Hence, the anomaly marked as T_P in Fig. 4.7 is attributed to such premartensitic transition. For $x = 0.05$, a broad spike-like feature is obtained in TEP instead of a narrow dip. As the difference in T_M (= 250 K) and T_P (= 260 K) is about 10 K and the signatures due to these two anomalies are not well resolved in the TEP data. Two dips are also seen in $x = 0.1$, however, martensitic transformation occurs at 280 K in this sample. Hence the smaller dip at 250 K is an additional feature occurring in the martensitic regime. It may be noted that the susceptibility measurements for $x = 0.1$ also showed a signature at 250 K. Thus this anomaly can be related to intermartensitic transition. The TEP data for $x = 0.13$, 0.16 are presented in Fig. 4.7(b) and show huge dips in TEP at T_M followed by a steep rise indicative of magnetic scattering (shown by curved arrows in figure). The huge dips in TEP of these samples is expected due to stronger phonon softening than in the samples with lower martensitic transition temperature [8]. For the $x = 0.19$, martensitic and ferromagnetic transformations are known to occur at the same temperature. The TEP data for this sample

indeed reflects this scenario.

4.5 Discussion

The martensitic transformation temperatures obtained from the four probe resistivity and a.c. susceptibility measurements agree with the literature values and confirm that the $Ni_{2+x}Mn_{1-x}Ga$ with $0 \leq x \leq 0.19$ compositions are close to nominal. In addition, we observe a intermartensitic transition in the $x = 0.1$ sample at around T = 250 K in the susceptibility data. These observations are further supported by the anomalies seen at the similar temperatures in the TEP measurements.

The resistivity of all the samples in the warming/cooling cycles show hysteresis that begin well above the martensitic transition and end below T_M. Interestingly, on close inspection of the data, it is seen that much pronounced thermal hysteresis is seen only in $x \geq 0.13$ in comparison to the $x \leq 0.10$ samples. It is for the same concentration range that the lattice parameter ratio changes: from c/a > 1 for $x \geq 0.13$ to c/a < 1 for $x \leq 0.10$ samples. A difference in the hysteresis itself implies that there exists differently modulated structures that get transformed differently while warming and subsequent cooling. The XRD and optical microscopy images of different samples provide evidence for modulated structures. The connection of structural modulations and hysteresis in transport properties suggests that the underlying electron phonon coupling plays a crucial role in the intermartensitic transitions. It is argued that there are different nesting vectors formed due to differently modulated crystal structures in the martensitic phase. The conduction electrons get condensed differently in these changing nesting vectors. Such a process affects the overall transport properties due to changes in the available Fermi surface for conduction during the warming and cool-

ing process giving rise to hysteresis. The argument is convinciable as it is known from the inelastic neutron scattering measurements that premartensitic transition in Ni_2MnGa is due to electron phonon coupling which softens the TA_2 phonon mode. Such a phonon softening is believed to be due to contribution from electron-lattice coupling and nesting of the Fermi surface [6, 11]. This softening starts well above T_M and infact even above T_C. Further, the linear dependence of phonon frequency on temperature in the ferromagnetic state goes to zero much below T_M. This indicates that the modulations which begin in the premartensitic region well above T_M, continue across the martensitic transition and further down to region of intermartensitic transformations.

Thermoelectric power data brings out many interesting features of the $Ni_{2+x}Mn_{1-x}Ga$ series. Firstly, with increasing Ni replacing Mn atoms, the electron concentration increases and this is best reflected in the austenitic phase of all samples. In this region, a systematic increase in the magnitude of TEP is seen with increasing Ni content. This can be attributed to the electronic filling in the conduction band that takes place due to the electron transfer from nearly full $3d$ band of Ni to more than half filled $3d$ band of Mn. Further, TEP shows variations with changing concentration in the martensitic phase as well. For a typical ferromagnetic Heusler alloy, TEP goes through a minima at $\sim 0.4T_C$ at low temperature [19]. A minima in TEP with a smooth parabolic type of variation is clearly seen for $x = 0$, 0.05 samples in the low temperature region. While for $x = 0.1$ onwards, TEP does go through a minima but thereafter, does not show a typical T^2 type of dependence. A reduced $|S|$ in samples with $x \geq 0.1$ implies that the conduction electrons are getting scattered strongly after entering the martensitic phase. Such a change occurs probably as a result of different

nesting vectors formed due to differently modulated crystal structures in the martensitic phase. Thus the conduction electrons get condensed differently in these changing nesting vectors. Another important observation is the overall behaviour of TEP for $x = 0.19$. As seen from Fig. 4.7 the overall magnitude of TEP in the entire temperature range increases systematically on going from $x = 0$ to 0.16, while, $x = 0.19$ has lower value of TEP. This behavior of 0.19 to stand out in relation to others in the sequence is perhaps the consequence of its crystal structure. As stated earlier, the crystal structure of the martensitic phase of the Ni-Mn-Ga alloys depends on composition and temperature. Studies by Lanska *et.al* [20] brings out a correlation between the tetragonality (c/a) of the martensitic structure, T_M and average number of valence electrons per atom (e/a). It is shown that in the e/a range of 7.61 to 7.72, different crystal structures viz. 5M, 7M or non-modulated can be obtained upon undergoing martensitic transformation. Particularly, 5M or 7M transformations occur in samples with T_M below T_C. In the present study, the e/a values for samples range from 7.5 to 7.64 (refer Table 4.1) with $x \geq 0.13$ lying in the range 7.6 to 7.64. Also, the martensitic transition occurs in the ferromagnetic state expect for $x = 0.19$. Thus in the martensitic region, the crystal structure for $x = 0.13$, 0.16 is modulated and for $x = 0.19$ it could be non-modulated [5, 20]. Also, as per the band model, there is a change in the width of the energy bands due to deformation of crystal structure and the degree of overlap of the associated orbitals changes. The fact that $x = 0.19$ has a non-modulated structure leads to deviation in the overall behaviour of its TEP from the rest of the series.

According to simple semi-classical result for thermal diffusion in metals, the total TEP

for a ferromagnetic system can be expressed as,

$$S = S_m + S_s$$

where S_m is the magnetic contribution and

$$S_s = -\frac{1}{e\sigma T}\int(\epsilon - \mu)\frac{\partial f_0}{\partial \epsilon}\sigma(\epsilon)d\epsilon$$

where f_0 is the Fermi-Dirac distribution function, μ is the chemical potential and

$$\sigma = \int \sigma(\epsilon)\frac{\partial f_0}{\partial \epsilon}d\epsilon$$

It can be clearly seen that TEP is dependent on density of states (DOS) near the Fermi level. The above result has been used to explain the TEP of shape memory alloy, NiTi assuming a DOS with a peak near Fermi level [18].

The alloys in the present study are in the ferromagnetic state and hence the magnetic scattering can be assumed to be similar for all the samples. Thus change in TEP with respect to the concentration of alloys can be related only to changes in DOS at the Fermi level. Further, the band structure of Ni_2MnGa has been calculated and the composition of bands that are active at the Fermi surface have been identified [21, 22]. According to these calculation there is a peak in DOS just below the Fermi level comprising of minority spin Ni e_g band. A peak is indeed seen in the temperature derivative of TEP near the martensitic transition temperature. This is presented in Fig. 4.8(a) where temperature derivative of TEP with respect to normalized temperature (T/T_M) is plotted for three representative samples. In the range $0.86 \leq T/T_M \leq 1.02$ there lies an inflection point that shifts from 0.88 to 0.98 in going from Ni_2MnGa to $Ni_{2.19}Mn_{0.81}Ga$. Such a shift is an indication of changes

occurring in the DOS within the martensitic phase. Upon martensitic transformation, a structural change from cubic to orthorhombic leads to lifting of degeneracy of $3d$ levels. It is the splitting of energy sub-bands which are degenerate in the cubic phase that enables the electrons to redistribute themselves in order to lower the free energy. This is the well known band Jahn-Teller mechanism and has been observed in Ni_2MnGa using polarized neutron scattering [14]. For a martensitic transition to occur it is required that the peak in the DOS should have some asymmetry, whereby it has more weighting towards lower energies and that the Fermi level is situated very close to the peak. From the present TEP data, the shift of the inflection point from 0.88 to 0.98 with increasing Ni content can be attributed to the movement of the Ni e_g band towards Fermi level thereby leading to increase in T_M.

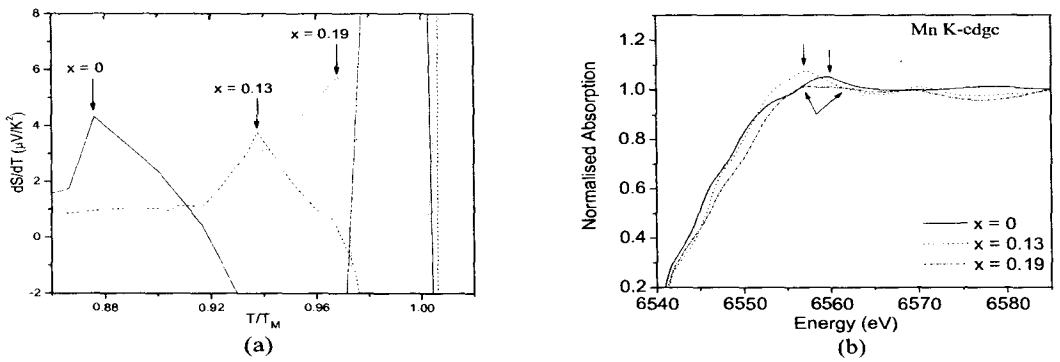

Figure 4.8: (a) Temperature derivative of thermopower versus normalized temperature in $Ni_{2+x}Mn_{1-x}Ga$ for representative concentrations. (b) Room temperature Mn K-edge XANES in $Ni_{2+x}Mn_{1-x}Ga$ for the same concentrations. The arrow indicates the peak position for the respective alloy composition.

The movement of the energy band towards Fermi level and existence of band Jahn-Teller effect is further verified by the features seen in X-ray Absorption Near Edge Structure (XANES) studies. The room temperature XANES at Mn and Ga K-edges were recorded for

the present series and the spectra for three nominal compositions spanning the austenitic to martensitic regimes are presented in Fig. 4.8(b). The near edge region can be considered as the region presumably containing the local chemical information. Especially in the case of metals, on applying the band structure approach, the absorption edge can be considered to correspond to the Fermi level and the higher energy region as the unoccupied density of states. Any feature associated with energy higher than that of the edge energy, then, would reflect the changes in DOS near Fermi level. It is seen from the Fig. 4.8(b) that the peak in $x = 0.13$ is at a lower energy value in comparison to the peak in $x = 0$. For $x = 0.19$, two distinct peaks are seen to occur at higher energy values. This observation can be inferred as the band that was degenerate in the austenitic state ($x = 0$), moves closer to Fermi level when martensitic transformation sets in ($x = 0.13$) and finally splits into two bands when the transformation is fully complete as for $x = 0.19$.

4.6 Conclusions

The structural studies are suggestive of modulated crystal structure for martensitic phase of these alloys as reflected from the broadened XRD peaks. It is also seen that the martensitic structure stabilizes with the ratio of lattice parameters $c/a < 1$ for compounds with $x \leq 0.1$ and $c/a > 1$ for those with $x > 0.1$. Optical microscopy and SEM images recorded at room temperature are in agreement with this observation of X-ray diffraction; with modulations quite evident in the micrographs. The changes in the transport scattering behaviour of the conduction electrons due to changing crystal structure are also reflected in the resistivity measurements. The trends in the resistivity in the $x = 0.1$ samples and that $x > 0.1$ samples are quite different. Resistivity and a.c. susceptibility also present signatures of premarten-

sitic, martensitic and intermartensitic transitions. The hysteresis observed in the warming /cooling cycles of transport measurements signifies the nesting of conduction electrons in the changing Fermi surface associated with increasing Ni content.

Thermoelectric power measurements on the $Ni_{2+x}Mn_{1-x}Ga$ with $0 \leq x \leq 0.19$ reflects the changes in the density of states consistent with the changes in the electronic structure due to band Jahn Teller effect. The increase in martensitic transformation temperatures with increasing Ni content can be related to the shifting of a peak in DOS at Fermi level closer to E_F. This is further verified by the XANES studies. The change in behaviour of TEP from that expected for a typical Heusler alloy, in the martensitic region can be related to the differently modulated crystal structures formed upon martensitic transformation.

References

[1] P. J. Webster, K. R. A. Ziebeck, S. L. Town and M. S. Peak, Philos. Mag **49**, 295 (1984).

[2] P. J. Brown, J. Crangle, T. Kanomata, M. Matsumoto, K-U Neumann, B. Ouladdiaf and K. R. Ziebeck, J. Phys.: Condens. Matter **14** 4715 (2002).

[3] A. N. Vasil'ev, A. D. Bozhko, V. V.Khovailo, I. E. Dikshtein, V. G. Shavrov, V. D. Buchelnikov, M. Matsumoto, S. Suzuki, T. Takagi and J. Tani, Phys. Rev. B **59**, 1113 (1999).

[4] V. V. Martynov and V. V. Kokorin, J. Phys. III **2**, 739 (1992).

[5] J. Pons, V. A. Chernenko, R. Santamarta and E. Cesari, Acta. Mater. **48** 3027 (2000).

[6] A. Zheludev, S. M. Shapiro, P. Wochner, A. Schwartz, M. Wall and L. E. Tanner, Phys. Rev. B **51**, 11310 (1995).

[7] U. Stuhr, P. Vorderwisch, V. V. Kokorin and P. A. Lindgard, Phys. Rev. B **56**, 14360 (1997).

[8] U. Stuhr, P. Vorderwisch and V. V. Kokorin, J. Phys.: Condens. Matter. **12**, 7541 (2000).

[9] L. Manõsa, A. González-Comas, E. Obrado, A. Planes, V. A. Chernenko, V. V. Kokorin and E. Cesari, Phys. Rev. B **55**, 11068, (1997).

[10] A. Planes, E. Obrado, A. González-Comas and L. Manõsa, Phys. Rev. Lett. **79**, 3926, (1997).

[11] S. B. Dugdale, R. J. Watts, J. Laverock, Zs. Major, M. A. Alam, M. Samsel-Czekala, G. Kontrym-Sznajd, Y. Sakurai, M. Itou and D. Fort, Phys. Rev. Lett. **96**, 046406 (2006).

[12] V. V. Khovailo, T. Takagi, A. D. Bozhko, M. Matsumoto, J. Tani and V. G. Shavrov, J. Phys.: Condens. Matter **13**, 9655 (2001).

[13] V. A. Chernenko, J. Pons, C. Segui and E. Cesari, Acta. Mater. **50**, 53 (2002).

[14] P. J. Brown, A. Y. Bargawi, J. Crangle, K-U. Neumann and K. R. Ziebeck, J. Phys.: Condens. Matter. **11**, 4715 (1999).

[15] V. V. Khovaylo, V. D. Buchelnikov, R. Kainuma, V. V. Koledov, M. Ohtsuka, V. G. Shavrov, T. Takagi, S. V. Taskev and A. N. Vasil'ev, Phys. Rev. B **72**, 224408 (2005).

[16] A. Sozinov, A. A. Likhachev, N. Lanska and K. Ullakko, Appl. Phys. Lett **80**, 1746 (2002).

[17] E. Fawcett, Rev. Mod. Phys. **60**, 209 (1988).

[18] J. Y. Lee, G. C. McIntosh, A. B. Kaiser, Y. W. Park, M. Kaach, J. Pelzl, Chul Koo Kim and Kyun Nahm, J. Appl. Phys. **89**, 6223 (2001).

[19] H. Hamzic, R. Asomoza and I. A. Campbell, J. Phys. F: Metal Phys. **11**, 1441 (1981).

[20] N. Lanska, O. Söderberg, A. Sozinov, Y. Ge, K. Ullakko and V. K. Lindroos, J. Appl. Phys. **95**, 8074 (2004).

[21] S. Fuji, S. Ishida and S. Asano, J. Phys. Soc. Japan. **58**, 3657 (1987).

[22] A. T. Zayak and P. Entel, J. Magn. Magn. Mater. **290-291**, 874 (2005).

Chapter 5

Local Atomic Structure of $Ni_{2+x}Mn_{1-x}Ga$: An EXAFS Study

5.1 Introduction

The martensitic phase transformation in Ni_2MnGa proceeds via periodic shuffling of the (110) planes along the $[1\bar{1}0]_P$ direction of the initial cubic system [1] with modulation period dependent on the composition as summarized in [2]. Studies in the past have attributed the structural transformations to the phonon anomalies occurring in the parent phase [3, 4]. In Ni_2MnGa, an incomplete softening of the TA_2 phonon mode at a wave vector $\zeta_0 \sim 0.33$ reciprocal lattice units takes place [5, 6, 7]. Such a phonon softening is believed to be due to contribution from electron-lattice coupling and nesting of the Fermi surface [8, 9, 10]. Extensive experimental studies [1, 11, 12, 13, 14, 15, 16] and theoretical efforts [17, 18, 19, 20, 21, 22, 23, 24, 25, 26] that reflect the Fermi surface character of Ni_2MnGa upon undergoing martensitic transformation have been carried out. Recent calculations by [23, 24] indicate the importance of modulated structure and the shuffling of atomic planes in stabilizing the martensitic structure in stoichiometric and non-stoichiometric alloys. The stability of the structure is associated with a dip in the minority-spin density of states (DOS) at the Fermi

level, related to the formation of hybrid states of Ni d and Ga p minority-spin orbitals [25. 26]. The shuffles in these alloys are believed to be due to two different effects - modulations and tetrahedral distortions [24]. Also it is predicted that the amplitude of modulations are different for Mn-Ga and Ni planes [23]. Therefore a precise knowledge of the changes occurring in the local structure of constituent atoms is fundamental in understanding the mechanism involved in martensitic phase transformation. X-ray absorption fine structure (XAFS) is an ideal tool to study such transformations by making a comparative study of the local structure in austenitic and martensitic phases. It is with this objective that the present investigation was undertaken.

In this Chapter we study the local atomic structure of $Ni_{2+x}Mn_{1-x}Ga$ inorder to understand the atomic re-arrangements that occur upon martensitic transformation. From the investigation of the structural properties we see that the martensitic structure is a distortion of the initial cubic lattice with modulations in the crystal planes. This modulated structures are seen to severely affect the magnetic and transport properties causing significant differences from normal metallic behaviour and giving rise to hysteresis in the measured properties. It is also evident from the study so far, that, there exists different intermartensitic transformations as the alloys are subjected to variation in temperature in the martensitic region. Thermoelectric power is also seen to be affected by the intermartensitic transformations causing systematic changes with increasing Ni content that can be associated with the changes in the DOS near Fermi surface.

The Mn and Ga K-edge XAFS were recorded at room temperature and liquid nitrogen temperature in the $Ni_{2+x}Mn_{1-x}Ga$ system to explore the changes in local environment

around these metal ions in the austenitic and martensitic phase. We have carried out the measurements on the alloy compositions: $Ni_{2+x}Mn_{1-x}Ga$ with x = 0, 0.1, 0.13, 0.16 and 0.19. The transformation temperature T_M in this series is known to increase systematically from 220 K to 330 K with increasing Ni content. Essentially, samples with x = 0, and 0.10 are in the austenitic phase at room temperature, whereas x = 0.13 undergoes a transition at $\sim$ 295 K and x = 0.16 represents the martensitic phase with T_M = 315 K. The x = 0.19 is special as the martensitic transformation and magnetic ordering takes place at the same temperature, i.e. $T_M = T_C \sim 330$ K. The coincidence of the structural and magnetic transitions in this alloy composition drastically affects its physical properties placing it apart from other members of the $Ni_{2+x}Mn_{1-x}Ga$ series. For example, it is known to exhibit a giant magnetocaloric effect - a property that can be exploited for immediate technological application as an alternative to conventional refrigeration [27]. The difference in its behaviour is also reflected in the XAFS measurements. Hence the analysis for this sample are presented separately.

At liquid Nitrogen temperature all the samples are in the martensitic phase. It may be noted that, although Mn content changes from 1 to 0.81, this change amounts to less than one atom per unit cell. Furthermore, the atomic number of Mn (Z = 25) and that of Ni (Z = 29) being similar, the X-ray scattering amplitudes and phase functions will not be drastically different and EXAFS would be insensitive to such a substitution. Therefore we have selected those alloy compositions that span the transformation from austenitic to martensitic region. Also, the substitution of Mn by Ni causes the dilution of the magnetic interactions and provides an opportunity to study the link, if any, between magnetism and

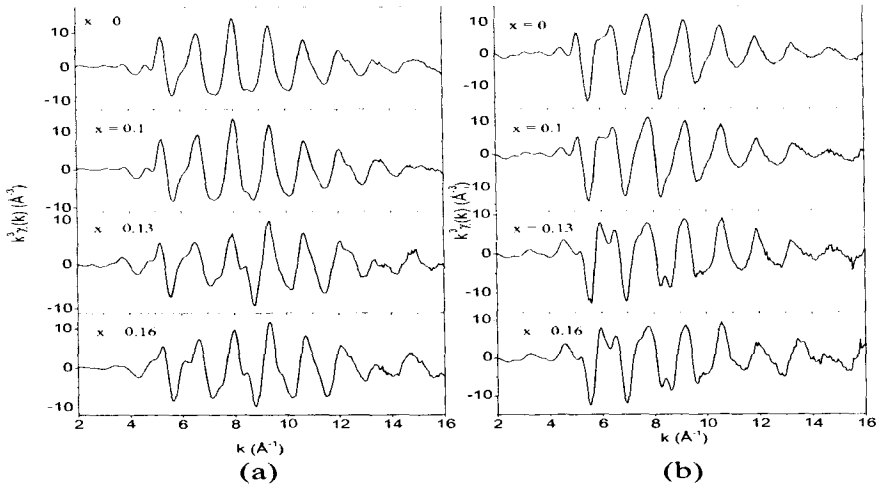

Figure 5.1: The room temperature k^3 weighted EXAFS at (a) Mn K edge (b) Ga K edge in samples with x = 0, 0.1, 0.13, 0.16. These data were Fourier transformed in the range (2-15) $Å^{-1}$ for analysis.

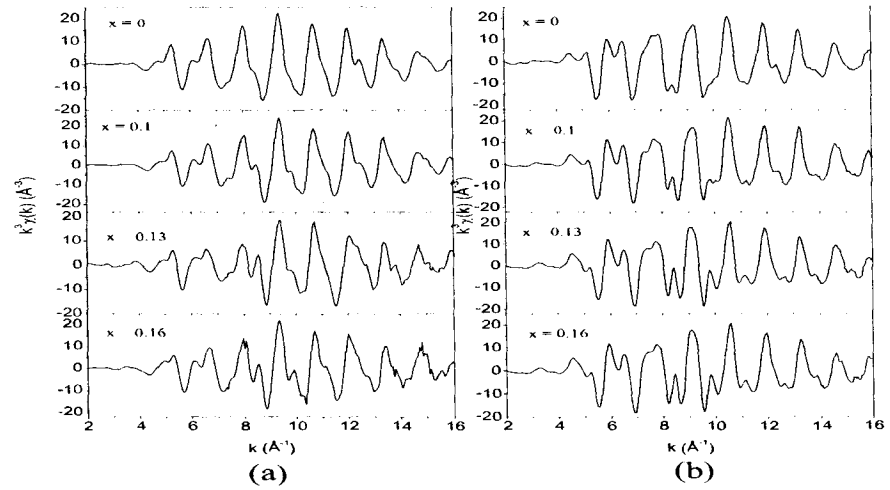

Figure 5.2: The low temperature k^3 weighted EXAFS in samples with x = 0, 0.1, 0.13, 0.16 samples obtained at (a) Mn K edge and (b) Ga K edge. The data in the range (2-15) $Å^{-1}$ was Fourier transformed for analysis.

martensitic transition.

The changes occurring in the $L2_1$ unit cell and the bond lengths obtained from the analyses enables us to determine the modulation amplitudes over which the constituent atoms move giving rise to shuffling of the atomic planes in the modulated structure. The EXAFS analysis also suggests the changes in hybridization of Ga-p and Ni-d orbitals associated with the local symmetry breaking upon undergoing martensitic transition. The k^3-weighted $\chi(k)$ spectra at Mn and Ga K-edges in all the samples at RT and LT are shown in Fig. 5.1 and Fig. 5.2 respectively. These spectra reflect the good quality of data up to 15Å^{-1}. The Fourier transform (FT) magnitude in R space of the k^3 weighted Mn K-edge EXAFS at RT and LT are shown in Fig. 5.3.

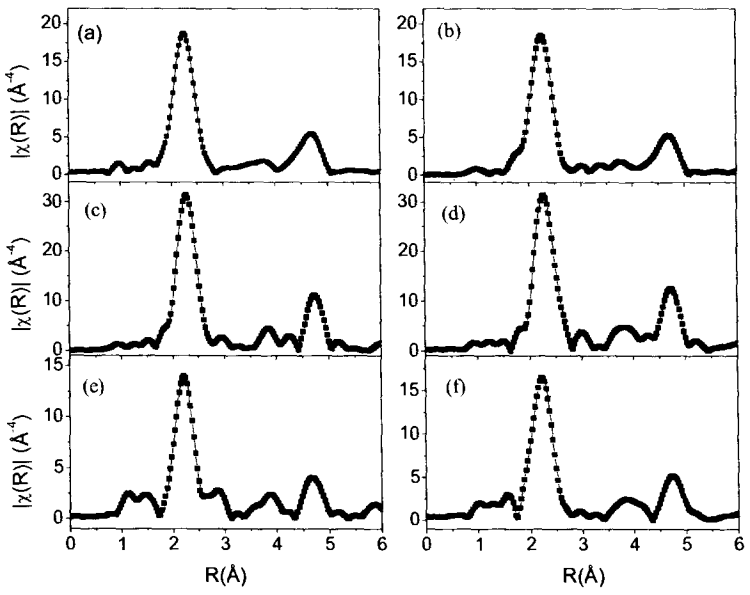

Figure 5.3: The magnitude of Fourier Transform spectra for Mn K-edge EXAFS in the austenitic phase of (a) $x = 0$ (b) $x = 0.1$ and in the martensitic phase of (c) $x = 0$, (d) $x = 0.1$, (e) $x = 0.13$ and (f) $x = 0.16$.

5.2 Results

5.2.1 Austenitic Phase

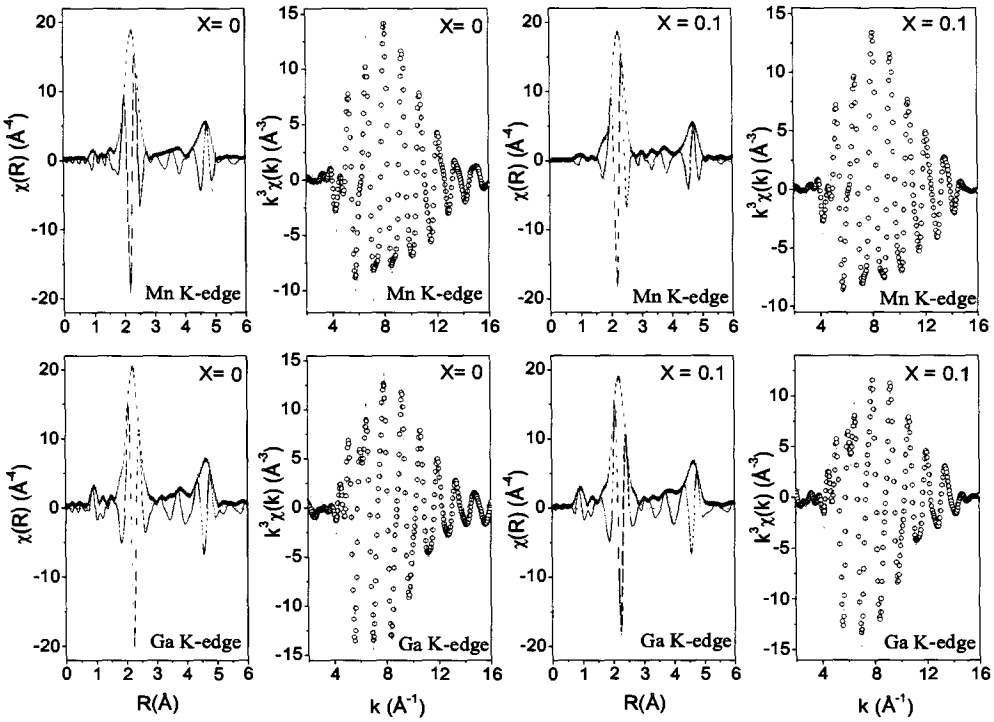

Figure 5.4: Magnitude and real component of FT of EXAFS spectra in R space and real component of FT in the back transformed k space for Mn and Ga K-edge in $x = 0$, 0.1 at room temperature. The fitting to the data are shown in coloured line.

At room temperature the samples with $x = 0$ and 0.1 are in the austenitic phase. Therefore, the EXAFS spectra of these samples recorded at Mn and Ga K-edges were fitted using common set of variable parameters with Fm3m space group and lattice constant 5.825Å. In this model, the correction to the path lengths was refined with a constraint,

$$\delta R = \delta r_1 \times \frac{R_{eff}}{R_{nn1}}$$

where R_{nn1} is the nearest neighbour distance, kept fixed to 2.5223Å obtained from the lattice constant, R_{eff} is the calculated bond length obtained from FEFF and δr_1 is the change in first neighbour distance. This approach reduces the number of variable parameters in the fit. The thermal mean-square variation in the bond lengths, σ^2 were varied independently for each path considered in the fit. The fitting was carried out in R-space in the range 1Å to 5Å using four single scattering (SS) paths and one linear multiple scattering (MS) path along the body diagonal of the initial cubic cell. The magnitude and real component of FT of $k^3\chi(k)$ for Mn and Ga edge data are shown in Fig. 5.4. As can be seen from the figure, the fits are quite satisfactory. The bond distances and the final fitted parameters obtained are presented in the Table 5.1.

Table 5.1: Results of the fits to the room temperature Mn and Ga edge data of x = 0, 0.10. R refers to the bond length and σ^2 is the thermal mean square variation in the bond length. The fittings were carried out in k range: (2- 15)Å^{-1} with k-weight: 3 and R range: (1-5)Å. Figures in parentheses indicate uncertainty in the last digit.

	$x = 0$		$x = 0.1$	
Atom and Coord. No.	R (Å)	σ^2 (Å^2)	R (Å)	σ^2 (Å^2)
		Mn K-edge		
Ni1 × 8	2.519(8)	0.0081(3)	2.518(2)	0.0080(2)
Ga1 × 6	2.909(3)	0.03(1)	2.795(8)	0.014(1)
Mn1 × 12	4.114(4)	0.029(9)	4.20(2)	0.021(3)
Ni2 × 24	4.824(5)	0.019(3)	4.85(1)	0.019(2)
Ga2 × 16	5.038(5)	0.007(1)	4.900(8)	0.008(1)
MS[a] × 8	5.038(5)	0.0097(6)	5.02(1)	0.018(2)
		Ga K-edge		
Ni1 × 8	2.512(2)	0.0077(2)	2.516(3)	0.0082(4)
Mn1 × 6	2.901(2)	0.030(6)	2.88(5)	0.026(7)
Ga1 × 12	4.103(3)	0.022(4)	4.23(4)	0.017(5)
Ni2 × 24	4.811(4)	0.015(1)	4.79(1)	0.016(2)
Mn2 × 16	5.025(3)	0.017(7)	4.90(1)	0.007(1)
MS[b] × 8	5.025(3)	0.014(1)	5.15(3)	0.023(4)

[a] Mn→Ga3→Ni1→Mn [b] Ga→Mn3→Ni1→Ga

It is seen that there is a discrepancy in the Mn-Ga and Ga-Mn bond distance for x

= 0.1 sample. The σ^2 values for this bond are also quite different. The reason for this anomaly could be the proximity of its martensitic transformation temperature (T_M = 285K) to the temperature of EXAFS measurement (295K). It is well known in literature that the martensitic transformations are preceded by a pre-transformation effects like softening of phonon modes and anomalies in elastic constants. Inelastic neutron scattering studies have evidenced such anomalies in Ni-Mn-Ga alloys [5, 6]. The T_M for x = 0.1 sample being only 10K below the room temperature, pre-transformational effects would be much intense here, giving rise to anomalies in σ^2 and causing discrepancies in bond distance of the near-neighbour atoms.

5.2.2 Martensitic Phase

Samples with composition x = 0, 0.1

Figures 5.3(c) and 5.3(d) demonstrates the low temperature EXAFS in R space at Mn edge for x = 0 and 0.10 samples present in their martensitic phase. In the range R = 2.5 - 5.0Å a difference in spectral signatures of the two alloys in the LT and RT data is quite evident. This can be attributed to the lowering of symmetry from the parent cubic structure upon undergoing the martensitic transition. Consequently, the EXAFS analysis was carried out using a tetragonal structure with c/a < 1 [1]. The σ^2 values obtained from the austenitic phase served as starting parameters and δR parameters were varied independently. The co-ordination number for each path was kept fixed to its crystallographic value. As per the model, with Mn as the absorbing atom, the first peak in the range R = 1.5 to 3.2 Å is due to the contribution from eight Ni atoms at 2.52Å, two Ga atoms at 2.78Å and four Ga atoms at 2.96Å. However, the σ^2s for Mn-Ga paths obtained from this fitting differ vastly from

each other with values of 0.003Å^2 and 0.03Å^2 respectively. Generally, at such close bond lengths, a large variation in σ^2 especially for the bonds involving same type of atoms is not expected. Therefore it indicates that there is a large spread in the bond distance of longer Ga neighbour and/or a different distribution of Ga atoms around Mn in the second and third shells. Thus the model was supplemented by carrying out fits with different combinations of six Ga neighbours distributed in the two shells. In each of these fits, σ^2 was varied keeping the coordination number fixed to a particular distribution. Best fit was obtained for four and two Ga atoms in the second and third shell respectively and the σ^2 obtained are presented in Table 5.2. Thereafter, such re-grouping of bond lengths had to be incorporated for all the subsequent SS paths. Here, the important aspect brought out by the analysis is the change in atomic coordinations leading to distribution of the bond lengths. This observation reflects the re-arrangement of atoms in different crystal planes in the martensitic phase. In other words, the constituent atoms have been displaced over varied distances giving rise to modulations in the crystal planes in trying to maintain volume conservation - an essential criteria for martensitic transition. Low temperature neutron diffraction studies on Ni_2MnGa by Brown *et.al* [28] have reported a modulated structure for Ni_2MnGa from which a similar grouping of bond length distribution of Ga atoms around Mn is obtained.

Refinement of Ga K-edge data also presents a similar situation. The parameters extracted from both the edges are presented in Table 5.2 and FT fittings in R space are shown in the Fig.5.5. The bond distribution with four and two coordination of Mn atoms are present around the central Ga atom at an average distance of 2.791Å and 3.065Å respectively. It is seen from the table that the third bond distance with Ga as central atom is larger by

Table 5.2: Results of the fits to the low temperature Mn and Ga edge data of $x = 0$, 0.10, 0.13 and 0.16. R refers to the bond length and σ^2 is the thermal mean square variation in the bond length. The fittings were carried out in k range: (2- 15)Å^{-1} with k-weight: 3 and R range: (1-5)Å. Figures in parentheses indicate uncertainty in the last digit.

	$x = 0$		$x = 0.1$		$x = 0.13$		$x = 0.16$	
Atom and Coord. No.	R (Å)	σ^2 (Å^2)	R (Å)	σ^2 (Å^2)	R (Å)	σ^2 (Å^2)	R (Å)	σ^2 (Å^2)
				Mn K-edge				
Ni1 × 8	2.518(3)	0.0057(4)	2.518(5)	0.0056(5)	2.528(2)	0.0060(2)	2.523(2)	0.0051(1)
Ga1 × 4	2.780(6)	0.0043(5)	2.768(8)	0.0037(7)	2.740(3)	0.0045(3)	2.739(5)	0.0054(4)
Ga2 × 2	2.96(3)	0.008(3)	2.95(2)	0.009(2)	3.12(2)	0.010(3)	3.23(4)	0.012(5)
Mn1 × 4	3.96(3)	0.009(3)	3.93(3)	0.009(3)	3.907(3)	0.012(4)	3.89(2)	0.008(2)
Mn2 × 8	4.19(1)	0.009(2)	4.19(1)	0.009(2)	4.22(1)	0.009(1)	4.23(2)	0.011(2)
Ni2 × 16	4.69(1)	0.011(1)	4.66(1)	0.009(1)	4.61(1)	0.013(2)	4.613(9)	0.009(1)
Ni3 × 8	4.90(1)	0.006(1)	4.905(8)	0.0040(7)	5.364(8)	0.0044(8)	5.327(8)	0.0044(8)
MS [a] × 16	5.068(6)	0.0095(7)	5.056(8)	0.0097(8)	5.088(4)	0.0078(4)	5.075(3)	0.0068(3)
				Ga K-edge				
Ni1 × 8	2.5111(8)	0.00431(8)	2.512(2)	0.0044(2)	2.512(1)	0.0039(1)	2.511(1)	0.0042(1)
Mn1 × 4	2.791(4)	0.0078(5)	2.776(8)	0.0062(5)	2.725(4)	0.0063(5)	2.722(5)	0.0067(6)
Mn2 × 2	3.065(2)	0.012(2)	3.06(2)	0.013(4)	3.0(2)	0.04(3)	3.0(1)	0.03(2)
Ga1 × 4	3.97(1)	0.009(2)	3.93(2)	0.008(2)	3.87(2)	0.008(2)	3.85(2)	0.009(2)
Ga2 × 8	4.215(8)	0.0076(8)	4.214(9)	0.0079(9)	4.25(1)	0.009(1)	4.248(7)	0.009(1)
Ni2 × 16	4.706(8)	0.0048(6)	4.676(6)	0.0081(7)	4.614(7)	0.0078(6)	4.619(7)	0.0083(7)
Ni3 × 8	4.889(3)	0.0047(3)	4.872(5)	0.0033(4)	5.313(8)	0.0026(5)	5.319(8)	0.0025(5)
MS[b] × 16	5.069(7)	0.0111(9)	5.111(5)	0.0089(6)	5.102(4)	0.0051(3)	5.106(2)	0.0047(2)

[a] Mn→Ga3→Ni1→Mn
[b] Ga→Mn3→Ni1→Ga

about 0.1Å as compared to that with Mn as the central atom. Also the σ^2 values obtained from Ga EXAFS for Ga-Mn bonds are higher than those obtained from Mn EXAFS (Table 5.2). The physical significance of these observations is that the Ga atoms have a smaller amplitude of displacement from its crystallographic position in comparison to Mn. In other words, Ga atoms are sluggish and do not get very displaced in undergoing a martensitic transition leading to a stronger hybridization between Ga-Ni in the martensitic phase.

Another important observation here is the discrepancy in the bond distance of the of the MS path described in Table 5.2. Being a linear path along the body diagonal of the initial cubic cell, the length of this path should be the sum of Mn-Ni and Ga-Ni bond lengths.

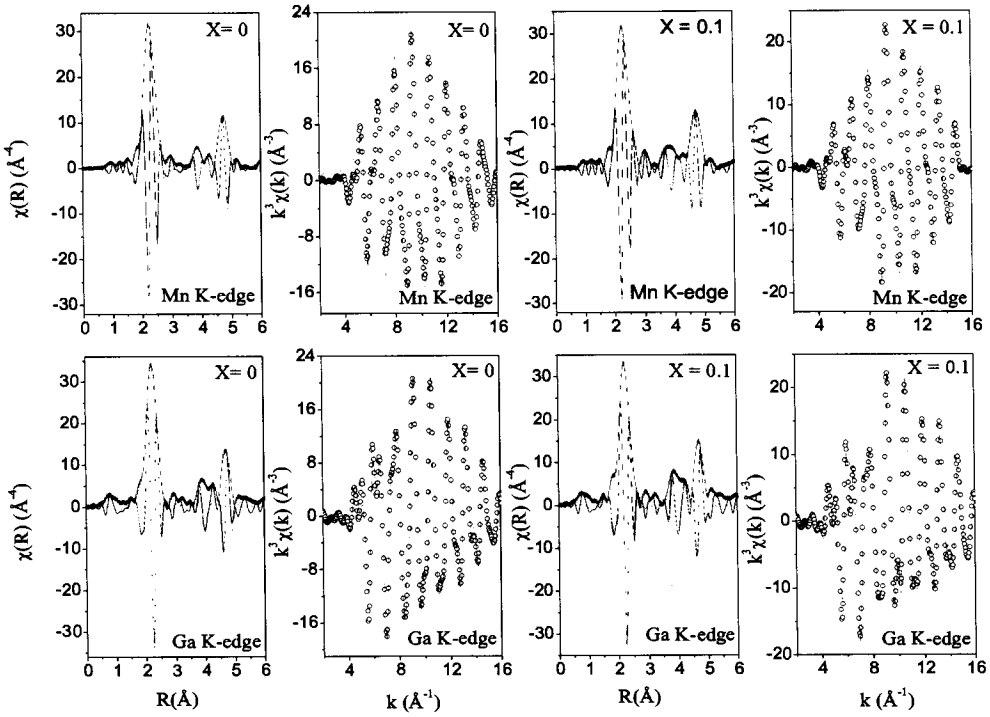

Figure 5.5: The low temperature Mn and Ga K-edge FT magnitude and real component of EXAFS spectra in R space and real component of FT in the back transformed k space $x = 0$, 0.1. The best fit to the data are shown as blue line.

Apparently, this condition is not satisfied in the LT data which implies that the MS path is no longer linear. It is this signature that once again brings in the prominence of movement of atoms in the martensitic phase. The distortions in atomic positions further results in "dimpling" of crystal planes as evidenced by non-linearity of the MS path giving rise to modulated structures. In short, it is seen from our RT and LT EXAFS analyses of $x = 0$, 0.10 samples that the martensitic transformation causes the atoms to displace from its initial positions by varied amplitudes with least displacement of Ga atoms causing local distortions. These local distortions gives rise to modulations and may eventually lead to

long-range ordering of unit cells over many atomic planes.

Samples with composition $x = 0.13$, 0.16

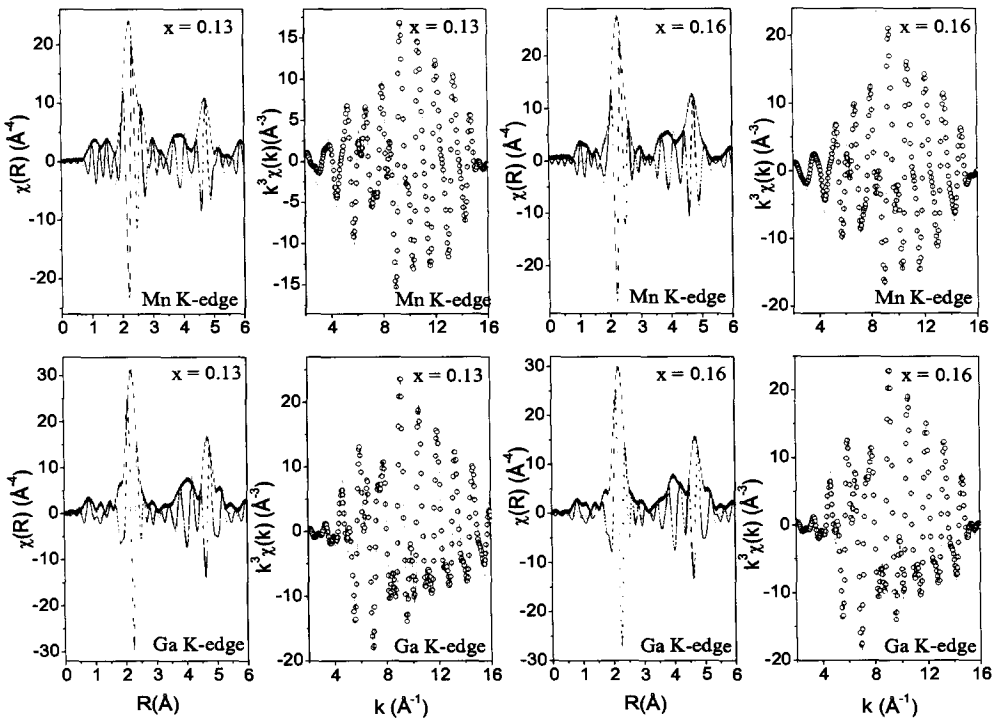

Figure 5.6: Low temperature, k^3 weighted, FT EXAFS spectra in R space and real component of FT in the back transformed k space for Mn and Ga K-edge for $x = 0.13$ and 0.16 samples. The blue line indicates best fit to the data.

The samples with $x = 0.13$, 0.16 are martensitic at room temperature. As can be seen from Fig. 5.3(e) and Fig. 5.3(f), the RT spectral signatures of these samples show subtle differences in comparison to the LT spectra for $x = 0$, 0.1. Thus a tetragonal structural model with $c/a > 1$ was employed for interpretation of the spectra [29]. In these samples, the RT and LT spectra are quite similar and hence the FT fittings in R space are presented for the low temperature data alone in Fig. 5.6. The bond distances obtained are presented

in Table 5.2. It is seen that the bond distances obtained from the two edges show notable difference, especially in the first shell. If one considers the difference between Mn-Ni and Ga-Ni bond distances alone, there is a change of about ~ 0.016Å. Both the central atoms, Mn and Ga can be viewed to be at the body centered position of a reduced tetragonal structure formed by eight Ni atoms. A non-uniformity in their bond distance with Ni of the order of 10^{-2}Å is unexpected and hints toward the microscopic changes influencing the formation of the macroscopic modulated phases. Also, the second and third shell distances obtained from the two edges are significantly different.

Furthermore, as can be seen from Table 5.2, Ga-Mn ($\sim$ 3Å) bond distance is shorter that the Mn-Ga ($\sim$ 3.2Å) bond distance. This is exactly opposite to the trend observed in LT spectra of $x = 0$, 0.1 where Ga-Mn = 3.06Å and Mn-Ga = 2.96Å. However, the σ^2 of Ga-Mn bond is much larger (0.03 Å^2 > 0.01 Å^2) than that of Mn-Ga bond. This typical behaviour of higher σ^2 for Ga-Mn bonds is prevalent in all the samples in martensitic phase. This result is critical because it is a direct indication of movement of constituent atoms from their crystallographic positions with Ga having the least amplitude of displacement. Thus, when viewed from Ga K-edge, the local structure seems to be much distorted with higher amplitudes of displacements for other constituent atoms and therefore a higher value of σ^2 for the respective bond.

Sample with composition $x = 0.19$

Here, the martensitic and magnetic transformations are coupled and occur at about 330 K. Thus the data at room temperature and low temperature contain information pertaining to martensitic phase alone. Accordingly, the EXAFS obtained from the Mn and Ga K-edge

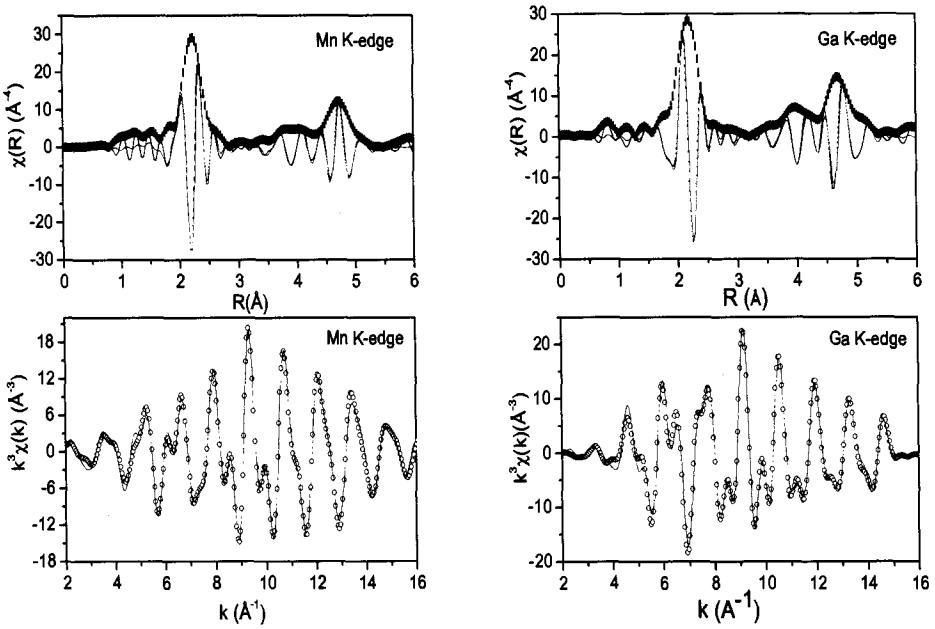

Figure 5.7: Low temperature, k^3 weighted, FT EXAFS spectra in R space and real component of FT in the back transformed k space for Mn and Ga K-edge for $x = 0.19$.

Table 5.3: Results of the fits to the low temperature Mn and Ga edge data of $x = 0.19$. R - bond length, σ^2 - thermal mean square variation in the bond length. Fit Details: k range (2- 15)Å^{-1} with k-weight = 3 and R range (1-5)Å. Figures in parentheses indicate uncertainty in the last digit.

Mn K-edge			Ga K-edge		
Atom and Coord. No.	R (Å)	σ^2 (Å^2)	Atom and Coord. No.	R (Å)	σ^2 (Å^2)
Ni1 × 8	2.519(5)	0.0049(1)	Ni1 × 8	2.512(1)	0.0044(1)
Ga1 × 4	2.73(2)	0.019(6)	Mn1 × 4	2.709(6)	0.0070(6)
Ga2 × 2	3.24(2)	0.016(11)	Mn2 × 2	3.27(3)	0.022(14)
Mn1 × 4	3.86(3)	0.016(5)	Ga1 × 4	3.86(2)	0.011(3)
Mn2 × 8	4.243(4)	0.010(2)	Ga2 × 8	4.251(7)	0.009(1)
Ni2 × 16	4.589(8)	0.011(1)	Ni2 × 16	4.608(6)	0.0084(6)
MS[a] × 16	5.07(4)	0.0073(3)	MS[b] × 16	5.108(3)	0.0053(2)
Ni3 × 8	5.32(7)	0.006(1)	Ni3 × 8	5.321(6)	0.0031(4)

[a] Mn→Ga3→Ni1→Mn

[b] Ga→Mn3→Ni1→Ga

were fitted with the tetragonal model ($c/a > 1$), same as that employed for $x = 0.13$, 0.16 samples. FT fittings in R space and back-transformed k-space for the low temperature data are presented at Fig. 5.7, while the corresponding bond distances and the σ^2 values are given in Table 5.3. Comparing these parameters to those in Table 5.2, it is seen that unlike for $x = 0.13$ and 0.16, there exists no discrepancy in the bond distances obtained from Mn and Ga edges. Especially the Mn-Ni, Ga-Ni bond distance and the corresponding σ^2 values match quite well within the error bars. Consequently, the obtained results suggest that the Mn-Ni, Ga-Ni tetrahedra are undistorted.

Moreover, the Mn-Ga, Ga-Mn bond distances (at ~ 3Å) are similar with no discrepancy in the corresponding σ^2 values. With respect to the $x = 0.13$, 0.16 martensitic systems, this result implies that there is no unequal movement of constituent atoms and hence no modulations should be present in $x = 0.19$. Indeed, the $x = 0.19$ system is known to undergo a structural transition to a non-modulated $L1_0$ unit cell with Ni atoms at the center and the corners sites occupied alternatively by Ga and Mn atoms.

5.3 Discussion

The local structural study of $Ni_{2+x}Mn_{1-x}Ga$ alloys in the austenitic and martensitic phases by EXAFS at Mn and Ga K-edge enable us to identify the microscopic changes influencing the formation of the macroscopic modulated structure. Based on our analyses the following results were obtained:

- Higher values of thermal mean square vibration, σ^2, for Ga K-edge analyses in comparison to Mn K-edge in the martensitic phase for $x = 0$, 0.10 samples.

- Different values of bond distances for the same pair of atoms (Ga-Mn) in the martensitic phase of all samples except $x = 0.19$.

- A difference of 0.016Å between Mn-Ni and Ga-Ni bond distance in $x = 0.13, 0.16$.

Firstly, the parameters obtained for the room temperature EXAFS data for $x = 0, 0.1$ are in line with those expected for the austenitic structure. The low temperature EXAFS spectra, for these samples have features different to those of the room temperature and carry information about the martensitic phase. The displacement of atoms occurring upon the structural change is reflected through higher values of σ^2. This argument is further supported by change in coordination numbers to 4+2 and re-grouping of the two Mn-Ga/Ga-Mn bonds. Thus the local symmetry breaking upon structural phase transition leads to the movement of constituent atoms. Such a modulated structure of Ni_2MnGa has been determined experimentally [28] and effect of shuffling of atoms on the physics of martensitic transformation has also been studied theoretically [30, 25]. On inspection of the parameters extracted from our analyses, it is seen that the σ^2 values are higher in case of Ga EXAFS than Mn EXAFS for the same Mn-Ga bond in the martensitic phase. This clearly indicates a spread or distribution of Mn-Ga bonds wherein Mn atoms moves more freely in comparison to Ga. This observation is further substantiated by a higher average bond length obtained with respect to Ga as central atom as compared to that obtained from Mn. Therefore there is a larger spread in Ga-Mn distance than Mn-Ga. In other words, Ga atoms are sluggish and have a smaller amplitude of displacement than other constituent atoms forming the alloy.

Thermal and stress induced martensitic transitions in Ni-Mn-Ga single crystals has been studied in the past [1] wherein, it was shown that the sample in martensitic phase undergoes

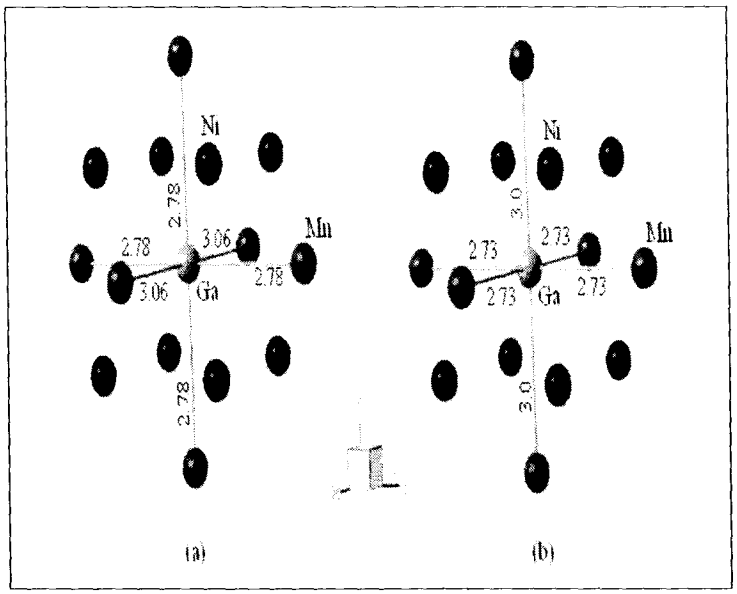

Figure 5.8: The local environment around the central Ga atom in martensitic phase (a) for $x = 0.1$ and (b) for $x = 0.13$.

another stress induced transition from a structure with $c/a < 1$ to that with $c/a > 1$. A similar transition is seen here in $Ni_{2+x}Mn_{1-x}Ga$ when x changes from 0.1 to 0.13. A simplistic view, as obtained from our EXAFS analyses, of local structure from Ga as central atom in the martensitic phase is as shown in Fig. 5.8. In the case of $x = 0.1$ wherein c/a is < 1, the effect of modulations is shown to be about the b axis. The shorter Mn-Ga bond lengths are therefore depicted along the b and c axes while the longer one is shown along the a axis. For $x = 0.13$, as described above, EXAFS can only be fitted to a structure with $c/a > 1$. Therefore in this case the longer Mn-Ga bond length is shown along the c axis and the shorter ones along a and b axes. A comparison of magnitudes of bond lengths clearly shows that in $x = 0.13$ a rotation about b axis transforms the structure similar to that of $x = 0.1$. Therefore the two martensitic structures are similar under rotation of Cartesian axes.

In order to further elucidate the local structure in Ni-Mn-Ga system, we look at the nearest neighbour interaction of the absorbing atoms. As mentioned in the previous section, there is a notable difference in the Mn-Ni and Ga-Ni bond lengths determined from the low temperature data for $x = 0.13, 0.16$. Comparing the estimates obtained, it is seen that Mn-Ni bond distance is higher than the Ga-Ni distance. The difference is greater than experimental resolution and demonstrates the locally distorted environment around Mn and Ga atoms leading to an electronic structure that is different in the austenitic and martensitic phases. Ni atoms reside inside the interlocking tetrahedral cages formed by Mn and Ga atoms. A shorter Ga-Ni bond means that Ga is more strongly bound to Ni than Mn. Thus the Ga tetrahedral is distorted in a way that allows more space for the movement of Mn atoms. Therefore Mn atoms have higher amplitude of displacement from its crystallographic position than Ga. These tetrahedral distortions lead to re-distribution of electrons and is perhaps the root cause of band Jahn-Teller transitions observed in such alloys [31, 32]. Such a Ni-Ga hybridization has also been anticipated theoretically [25]. These calculations yield energetically favorable hybrid states formed by Ga and Ni giving rise to a peak in the spin-down electronic density of states at the Fermi level.

Our interpretation of this EXAFS study, so far, is that the martensitic transformation in $Ni_{2+x}Mn_{1-x}Ga$ class of alloys results from the Ni-Ga hybridization that results from the distortion of Ni-Ga/ Ni-Mn tetrahedra. From the analysis for $x = 0.19$, it is seen that Ga-Mn and Mn-Ga bond distances are similar, suggesting that the martensitic structure is non-modulated. Further, the Ni-Mn bond distance is equal to that of Ni-Ga. This implies that there is no tetrahedral distortion and the hybridization of Ni with both, Mn and Ga

is of equal strength. On the other hand, it is known in literature that the magnetism in Heusler alloys is essentially confined to the Mn sublattice with the magnetic short-range X-Mn interaction being equally important for systems with sizeable magnetic moments on the X atoms such as Co and Ni [33, 34]. These interactions not only mediate the Mn-Mn interactions but they also participate in the formation of the magnetic state. For Ni-Mn-Ga alloys, the martensitic transformation and magnetic ordering mechanisms both can affect the density of states at E_F. Based on these arguments it can be stated that the equally strong Ni-Mn and Ni-Ga hybridization in $x = 0.19$ is perhaps responsible for the coupling of its magnetic and martensitic transition.

5.4 Conclusions

In this work, we have carried out a comparative analyses of changing local structures in $Ni_{2+x}Mn_{1-x}Ga$ alloys upon undergoing martensitic transition. EXAFS measurements at Mn K-edge and Ga K-edge at room temperature and liquid nitrogen temperature were carried out. The most significant feature of our analyses is the difference in the Mn-Ni and Ga-Ni bond length. A shorter Ga-Ni bond implies an increased Ga-Ni hybridization in comparison to Mn-Ni in the martensitic phase. The present study is a direct experimental evidence for such hybridization which is seen more clearly in $x = 0.13$ and 0.16 samples. The differences in the Mn-Ni and Ga-Ni bond lengths leads to the distortion of the two tetrahedra formed by Mn and Ga atoms with Ni atoms at the centre. The increased hybridization would probably lead to re-distribution of electrons causing a band Jahn-Teller effect. In addition, it is seen that the reason for coupling of magnetic and martensitic transition in $x = 0.19$ might be a manifestation of similar strength of Mn-Ni and Ga-Ni hybridization.

It is also seen that the constituent atoms of Ni-Mn-Ga system displace from their crystallographic positions by varying amplitudes in the martensitic phase. The Ga atoms seems to displace over very small amplitudes. The uneven movement of the constituent atoms gives rise to dimpling of atomic planes and may eventually lead to modulated structures.

References

[1] V. V. Martynov and V. V. Kokorin, J. Phys. III **2**, 739 (1992).

[2] J. Pons, V. A. Chernenko, R. Santamarta and E. Cesari, Acta. Mater. **48**, 3027 (2000) and references therein.

[3] S. M. Shapiro, Y. Noda, Y. Fujii and Y. Yamada, Phys. Rev. B **30**, 4314 (1984).

[4] S. M. Shapiro, B. X. Yang, Y. Noda, L. E. Tanner and D. Schryvers, Phys. Rev. B **44**, 9301 (1991).

[5] A. Zheludev, S. M. Shapiro and P. Wochner, Phys. Rev. B **51**, 11310 (1995).

[6] U. Stuhr, P. Vorderwisch, V. V. Kokorin, P.-A. Lindgard, Phys. Rev. B **56**, 14360 (1997).

[7] A. González-Comas, E. Obrado, L. Manõsa, A. Planes, V. A. Chernenko, B. J. Hattink and A. Labarta, Phys. Rev. B. **60**, 7085 (1999).

[8] G. L. Zhao and B. N. Harmon, Phys. Rev. B **45**, 2818 (1992).

[9] G. L. Zhao and B. N. Harmon, Phys. Rev. B **48**, 2031 (1993).

[10] S. B. Dugdale, R. J. Watts, J. Laverock, Zs. Major, M. A. Alam, M. Samsel-Czekala, G. Kontrym-Sznajd, Y. Sakurai, M. Itou and D. Fort, Phys. Rev. Lett **96**, 046406 (2006).

[11] K. Ooiwa, K. Endo and A. Shinogi, J. Magn. Magn. Mater. **104**, 2011 (1992).

[12] S. Wirth, A. Leithe-Jasper, A. N. Vasil'ev, J. M. D. Coey, J. Magn. Magn. Mater. **167**, L7 (1997).

[13] A. Sozinov, A. A. Likhachev, N. Lanska and K. Ullakko, Appl. Phys. Lett. **80**, 1746 (2002).

[14] A. N. Vasil'ev, V. D. Buchel'nikov, T. Takagi, V. V.Kholvailo and E. I. Estrin, Usp. Fiz. Nauk. **173**, 577 (2003) and references therein.

[15] K. R. Priolkar, P. A. Bhobe, S. D. Sapeco and R. Paudel, Phys. Rev. B **70**, 132408 (2004).

[16] Y. K. Kuo, K. M. Sivakumar, H. C. Chen, J. H. Su and C. S. Lue, Phys. Rev. B **72**, 054116 (2005).

[17] A. Ayuela, J. Enkovaara, K. Ullakko and R. M. Nieminen, J. Phys.: Condens. Matter. **11**, 2017 (1999).

[18] V. V. Godlevsky and K. M. Rabe, Phys. Rev. B **63**, 134407 (2001).

[19] A. Ayuela, J. Enkovaara and R. M. Nieminen, J. Phys.: Condens. Matter. **14**, 5325 (2002).

[20] J. M. MacLaren, J. Appl. Phys. **91**, 7801 (2002).

[21] Y. Lee, J. Y. Rhee and B. N. Harmon, Phys. Rev. B **66**, 054424 (2002).

[22] C. Bungaro, K. M. Rabe and A. Dal Corso, Phys. Rev. B **68**, 134104 (2003).

[23] A. T. Zayak, P. Entel, J. Enkovaara, A. Ayuela and R. M. Nieminen J. Phys.:Condens. Matter. **15**, 159 (2003).

[24] A. T. Zayak and P. Entel, Mater. Sci. Eng. A. **378**, 419 (2004).

[25] A. T. Zayak, P. Entel, K. M. Rabe, W. A. Adeagbo and M. Acet, Phys. Rev. B **72**, 054113 (2005).

[26] S. R. Barman, S. Banik and A. Chakrabarti, Phys. Rev. B **72**, 184410 (2005).

[27] L. Pareti, M. Solzi, F. Albertini and A. Paoluzi, Eur. Phys. J. B **32**, 303-307 (2003).

[28] P. J. Brown, J. Crangle, T. Kanomata, M. Matsumoto, K-U. Neumann, B. Ouladdiaf and K. R. A. Ziebeck, J. Phys.:Condens. Matter. **14**, 10159 (2002).

[29] B. Wedel, M. Suzuki, Y. Murakami, C. Wedel, T. Suzuki, D. Shindo and K. Itagaki, J. Alloys Compd. **290**, 137 (1999).

[30] A. T. Zayak, P. Entel, J. Enkovaara, A. Ayuela and R. M. Nieminen, Phys. Rev. B **68**, 132402 (2003).

[31] S. Fujii, S. Ishida and S. Asano, J. Phys. Soc. Japan **58**, 3657, (1987).

[32] P. J. Brown, A. Y. Bargawi, J. Crangle, K-U. Neumann and K. R. A. Ziebeck, J. Phys.:Condens. Matter. **11**, 4715 (1999).

[33] J. Kübler, A. R. Williams and C. B. Sommers, Phys. Rev. B **28**, 1745 (1983).

[34] P. J. Webster, J. Phys. Chem. Solids **32**, 1221 (1971).

Chapter 6

Factors influencing Martensitic interactions in $Ni_{50}Mn_{35}Sn_{15-x}In_x$

6.1 Introduction

Martensitic transformations and its pairing with ferromagnetism has been a central subject for investigation in the recent years. Especially, some intermetallics show simultaneous occurrence of martensitic and magnetic transitions, suggesting the possibility of controlling the structural transformation by magnetic field and could be exploited for practical applications. Among the variety of FSMA, Ni-Mn-Ga alloys are a recently synthesized class of alloys that have been studied extensively, hence serve as a reference in the development of new systems [1, 2, 3]. An interesting aspect of Ni-Mn-Ga alloys is the isothermal giant entropy change obtained when structural and magnetic transition temperatures nearly coincide, leading to a development of new materials exhibiting magnetocaloric effect [4]. The latest candidates in the field of FSMA has been alloys with composition $Ni_{50}Mn_{50-x}Z_x$ with Z = In, Sn, Sb [5]. Of particular interest are the Sn and In based alloys because of the properties like giant inverse magnetocaloric effect observed in $Ni_{50}Mn_{50-x}Sn_x$ ($0.13 \leq x \leq 0.15$) that is nearly three times larger in comparison to other alloys [6], and the large magnetoresistance (upto

60%) at moderate field values observed at room temperature in $Ni_{50}Mn_{50-x}In_x$ in the similar concentration range [7].

In particular, $Ni_{50}Mn_{36}Sn_{14}$ orders ferromagnetically at a Curie temperature $T_C \sim 320$ K while martensitic transition temperature $T_M \sim 220$ K [5]. Neutron diffraction experiments show that the cubic $L2_1$ structure in the austenitic phase transforms to orthorhombic $4O$ structure with *Pmma* space group in the martensitic phase [8]. $Ni_{50}Mn_{36}In_{14}$ on the other hand, orders ferromagnetically at about 309 K while martensitic transformation sets in at $\sim$ 290 K [5]. The structure in the austenitic phase is B2.

Studies show that despite structural similarity with Ni_2MnGa alloys, strong differences in the underlying martensitic and magnetic interactions are seen in Ni-Mn-Sn and Ni-Mn-In. While the martensitic transition is absent in the stoichiometric Ni_2MnSn and Ni_2MnIn, the Mn rich alloys undergo a phase change in the wide range of temperature [5]. Further, the magnetic moment of the Mn rich compositions, in the martensitic phase is lower by about 50% than that in cubic phase [9]. Even in the $L2_1$ phase, the Mn moments are significantly smaller than those reported for the stoichiometric Ni_2MnZ alloys [8, 10]. It is conjectured that apart from the ferromagnetic order, some antiparallel alignment of the excess Mn moments could exist in such systems [11]. Thus an understanding of the local structure in the martensitic and austenitic phases is vital in establishing a complete picture of the transformation mechanics. Further, following the empirical dependence of martensitic transition temperature on the e/a value, the T_M for Ni-Mn-Sn should be higher than that of Ni-Mn-In for the same stoichiometry as Sn has one electron in excess to In. However, as mentioned before, the T_M for Ni-Mn-Sn is $\sim$ 220 K which is much smaller that that

observed for Ni-Mn-In ($\sim$ 290 K). To resolve this issue of discrepancy in the e/a dependence, it would be interesting to progressively replace Sn by In in the solid solution of the form $Ni_{50}Mn_{35}Sn_{15-x}In_x$ with $0 \leq x \leq 15$ and understand the evolution of T_M with changing e/a. Other aspect that is related to this solid solution is the changing crystal structure: from $L2_1$ in Ni-Mn-Sn to B2 in Ni-Mn-In. Thus, a local structure study of the Ni-Mn-In-Sn solid solution becomes vital to gain insight into the mechanism of structural transformation. With this aim, we have carried out EXAFS measurements at Mn and Ni K-edges in $Ni_{50}Mn_{35}Sn_{15-x}In_x$ ($0 \leq x \leq 15$) at room temperature and liquid nitrogen temperature.

A comprehensive report of the local structure of Ni-Mn-Sn-In series along with its magnetic and transport properties is presented here. The starting alloy compositions and the corresponding elemental distribution as determined by energy dispersive X-ray analysis (EDX) are summarized in Table 6.1. In the following, we first present the results for $Ni_{50}Mn_{35}Sn_{15}$

Table 6.1: Elemental distribution in $Ni_{50}Mn_{35}Sn_{15-x}In_x$ series as determined from EDX analysis and the corresponding valence electron concentration.

Compositions		Ni	Mn	Sn	In	e/a
$Ni_{50}Mn_{35}Sn_{15}$	(Sn60)	50.40	34.60	15.00	—	8.05
$Ni_{50}Mn_{35}Sn_{11.25}In_{3.75}$	(Sn45)	50.87	33.49	12.02	3.62	8.0125
$Ni_{50}Mn_{35}Sn_{7.5}In_{7.5}$	(Sn30)	50.60	35.28	6.44	7.68	7.975
$Ni_{50}Mn_{35}Sn_{3.75}In_{11.25}$	(Sn15)	50.21	35.25	3.66	10.88	7.9375
$Ni_{50}Mn_{35}In_{15}$	(In60)	50.78	34.69	—	15.24	7.9

and $Ni_{50}Mn_{35}In_{15}$. The EXAFS studies for the Ni-Mn-Sn-In solid solution is presented in the next section.

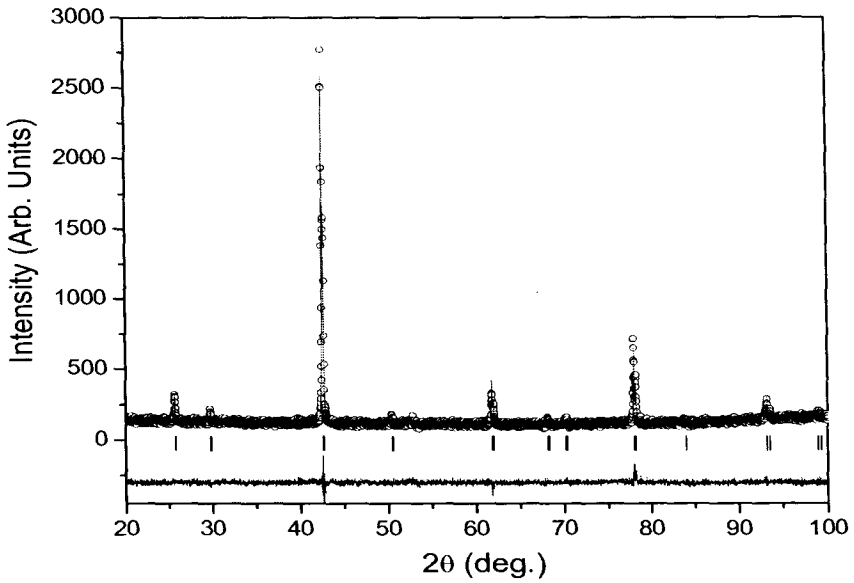

Figure 6.1: The X-ray powder diffraction pattern of $Ni_{50}Mn_{35}Sn_{15}$ at room temperature. The open circles show the observed counts and the continuous line passing through these counts is the calculated profile. The difference between the observed and calculated patterns is shown as a continuous line at the bottom of the two profiles. The calculated positions of the reflections are shown as vertical bars.

6.2 Results: $Ni_{50}Mn_{35}Sn_{15}$, $Ni_{50}Mn_{35}In_{15}$

The room temperature crystallographic structure was determined by X-ray powder diffraction (XRD) recorded on Rigaku D-MAX IIC diffractometer with Cu Kα radiation. Rietveld refinement of the room temperature XRD data confirms that the samples are single phase. Sn60 is highly ordered in the $L2_1$ Heusler structure with *Fm3m* space group and lattice parameters of 5.9941±0.0003 Å. The observed and calculated diffraction patterns together with the difference pattern are shown in Fig. 6.1. In the stoichiometric Heusler composition X_2YZ, $Ni_{50}Mn_{35}Sn_{15}$ (Sn60) can be described as X = Ni occupying the $(\frac{1}{4}\frac{1}{4}\frac{1}{4})$ site, Y = Mn occupying the (000) site and Z = (60% Sn + 40% Mn) occuping the $(\frac{1}{2}\frac{1}{2}\frac{1}{2})$ site. To distin-

guish between the Mn occupying the (0, 0, 0) position and the excess Mn that occupies the Z sites, it will henceforth be refered to as Y-Mn and Z-Mn respectively.

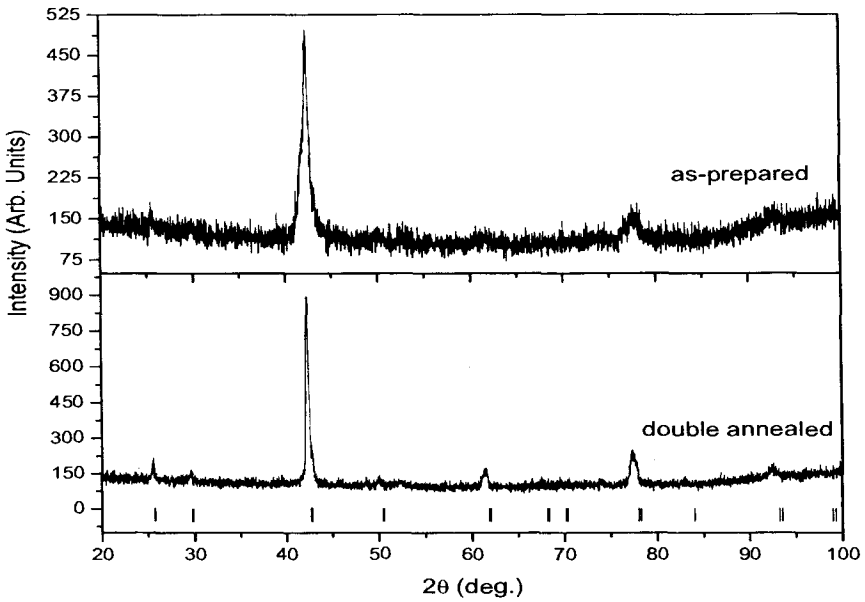

Figure 6.2: The X-ray powder diffraction pattern of as-prepared and double annealed $Ni_{50}Mn_{35}In_{15}$ recorded at room temperature. The as-prepared sample resembles a B2 structure. The superstructural peaks developed after double-annealing clearly indicates the $L2_1$ structure.The positions of reflections for the $L2_1$ structure are shown as vertical bars.

The XRD profile for In60 is presented at Fig. 6.2 and reflects a B2 crystal structure with lattice parameter 3.0196±0.0006 Å. The B2 crystal structure results from random occupation of the Y and Z sites by Mn and In atoms within the X_2YZ Heusler frame work. In addition to the annealing treatment given to all the samples at the time of sample preparation (method described in Chapter 2) the finely ground In60 powder used for XRD studies, was further annealed at 500° C for 24 hrs in an evacuated quartz ampoule and quenched in ice water. Such a heat treatment was given to improve the peak intensities and minimize

the structural strain in this sample. However, the XRD pattern recorded for such double-annealed sample showed some superstructural peaks reflecting structural order to be set in. These extra reflections resembles the $L2_1$ structure (see Fig. 6.2). Such a ordering of B2 $\rightarrow$ $L2_1$ structure, following a heat treatment, is common in Heusler alloys and has been observed in like-composition, Ni_2MnAl [12].

It is important to mention here that no further studies were carried out on such heat treated In60 powder. All the measurements including the EXAFS studies were carried out only on the pristine samples.

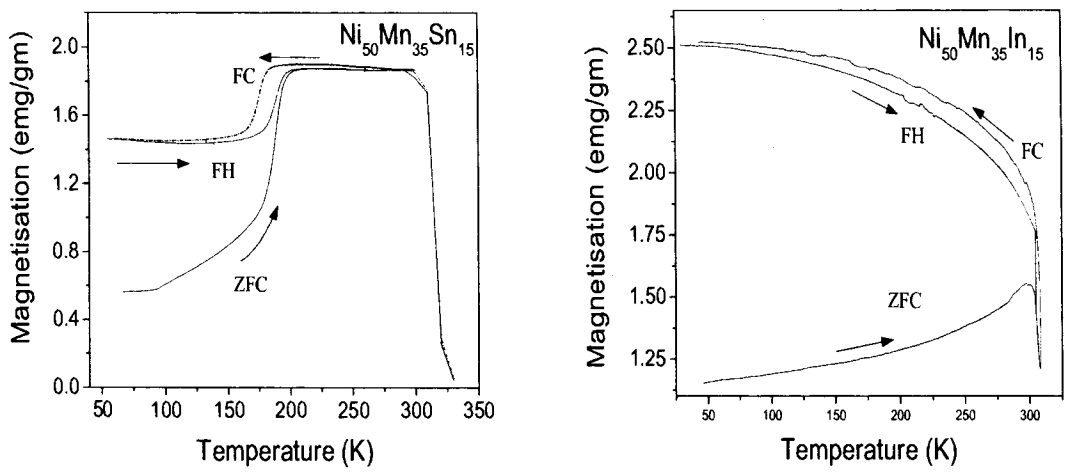

Figure 6.3: Temperature dependence of magnetization measured in an applied field of 50 Oe between 50 to 350 K. Measurements were carried out while heating (ZFC), cooling (FC) and re-heating (FH) the sample as indicated by the arrows. The structural and magnetic transition temperatures were determined from the differentials of magnetization with respect to temperature for FC and FH curves.

Magnetization was determined in a field of 50 Oe over the temperature range 50 - 350 K. Initially, the samples were cooled from room temperature to 50 K in the absence of magnetic field. An external field of 50 Oe was applied and magnetization was recorded with increasing

temperature upto 350 K (referred as ZFC). The measurements were made as the sample was subsequently cooled to 50 K without disturbing the magnetic field (FC) and finally the sample was field-heated (FH) upto 350 K. In Sn60 the ferromagnetic ordering sets in at Curie temperature T_C = 319 K. As the temperature is lowered, magnetization remains essentially constant until 200 K where an abrupt fall in M is observed. This behaviour corroborates with that reported for the martensitic phase transition in Ni-Mn-Sn alloys. The ZFC, FC and FH magnetization curves for Sn60 are shown in Fig. 6.3. The martensitic start (M_s = 182.7 K), martensitic finish (M_f = 164.3 K), reverse martensitic or austenitic start (A_s = 176.2 K) and austenitic finish (A_s = 195.6 K) temperatures are identified and the thermal hysteresis was calculated to be $\sim$ 12 K. Figure 6.3 includes the magnetization curves for the In60. The behaviour of M(T) is in close agreement with earlier reports [13]. The sudden upturn in M(T) observed at T_C = 309 K marks the ferromagnetic ordering temperature in this sample. With the decrease in temperature, the ZFC magnetization peaks around $\sim$ 290 K and starts to decrease thereafter. This feature marks the occurrence of martensitic transformation. No such decrease in M(T) is seen in the FC and FH curves. The hysteresis in the FC and FH curves for such samples is attributed to structural transformation while the splitting in the ZFC and FC curves just below T_C has been associated with competing magnetic interactions speculated in these systems [11]. In case of In60, the splitting between FC and FH curves extends right down to 50 K which can be attributed to multiple martensitic transitions as reported by [11] while a large splitting exists between the ZFC and FC curves of both samples. It is conjectured that the presence of excess Mn in such alloys may give rise to additional Mn-Mn interactions giving rise to some antiparallel alignment of moments.

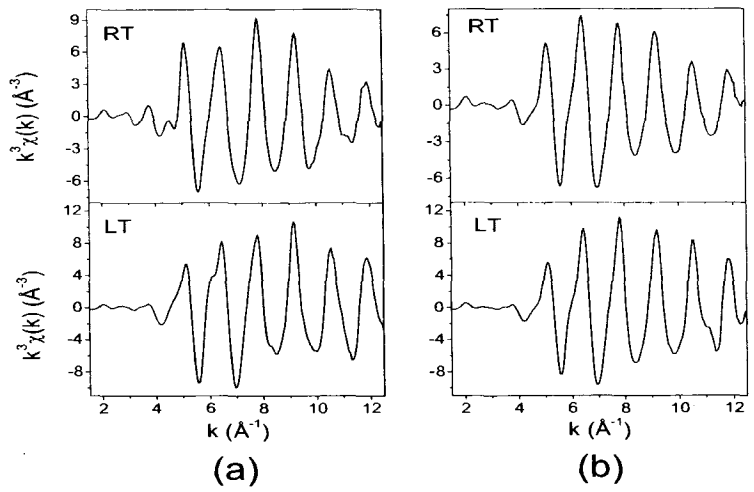

Figure 6.4: The k weighted $\chi(k)$ spectra at Mn K edge recorded at room temperature (RT) and low temperature (LT) in (a) $Ni_{50}Mn_{35}Sn_{15}$ (b) $Ni_{50}Mn_{35}In_{15}$. The data in the range (2-12) (Å^{-1}) was Fourier transformed for analysis.

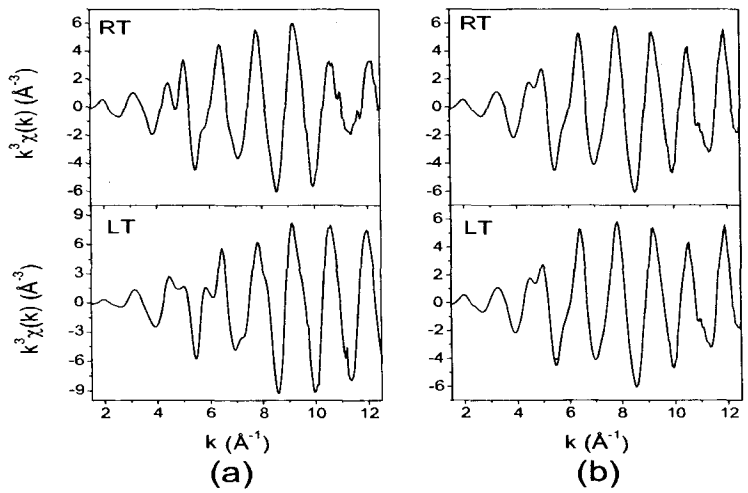

Figure 6.5: The k weighted $\chi(k)$ spectra at Ni K edge recorded at room temperature (RT) and low temperature (LT) in (a) $Ni_{50}Mn_{35}Sn_{15}$ (b) $Ni_{50}Mn_{35}In_{15}$. The data in the range (2-12) (Å^{-1}) was Fourier transformed for analysis.

The k-weighted $\chi(k)$ spectra at Mn and Ni K-edges at room temperature and liquid nitrogen temperature are shown in Fig.6.4 and Fig.6.5. The data in the k range of (2 - 12)Å^{-1} was used for analysis.

Room temperature Mn K-edge spectrum for Sn60 is shown at Fig. 6.4(a). With the knowledge of crystal structure from XRD, a model for data analysis for Sn60 was worked out. Fitting was carried out using four single scattering (SS) paths and one linear multiple scattering (MS) path along the body diagonal of the initial cubic cell. As per this model, the second SS path is due to scattering from Z atoms. Since this position is occupied by both Sn and Mn, the FEFF input file was suitably modified to include the contribution of Mn occupying the vacant Sn sites. For this, the fitting standards were calculated with Sn and Mn atoms entirely occupying the Z position. These were then introduced in the model with path coordination numbers as per their composition ratio. The structure being cubic at room temperature, the correction to the path lengths was refined with a constraint, $\delta R = \delta r_1 \times [R_{eff}/\ R_{nn1}]$ where R_{nn1} is the nearest neighbour distance, kept fixed to 2.5937Å (calculated from the lattice constant), R_{eff} is the calculated bond length obtained from FEFF and δr_1 is the change in first neighbour distance. The thermal mean-square variation in the bond lengths, σ^2 were varied independently for each path considered in the fit. This approach of data analysis has been successfully used for the EXAFS analysis of $Ni_{2+x}Mn_{1-x}Ga$ alloys [14]. In the Sn60 fit, the first neighbour, Mn-Ni distance obtained was 2.549Å which is much shorter than the value expected for the cubic cell. This points towards some disorder at the local level in the cubic structure. However, no structural disorder is seen either in the XRD profile (refer Fig. 6.1) or in the neutron diffraction study of $Ni_{50}Mn_{36}Sn_{14}$ by Brown

et.al [8].

In the case of Ni K-edge EXAFS the fitting for Sn60 was carried out in the R-range 1.0 - 3.0 Å . The peak in this range of the spectra comprises of Ni-Mn, Ni-Sn and Ni-Ni single scattering paths. The analysis similar to that of Mn EXAFS was carried out. However, this did not result in a good fit. To overcome this situation, δrs' for each of the three scattering paths were varied independently. A good fit was obtained for values listed in Table 6.2 as can be seen in Fig. 6.6.

Table 6.2: Parameters obtained from EXAFS analysis for the cubic phase of $Ni_{50}Mn_{35}Sn_{15}$ and $Ni_{50}Mn_{35}In_{15}$. The calculated distances from the lattice parameters of $L2_1$ and B2 cell are given. The analysis details are k range (2- 12)Å^{-1}; k-weight = 3; and R range (1-5)Å for Mn edge and (1-3)Å for Ni edge. Figures in parentheses indicate uncertainty in the last digit.

Sn60				In60			
Atom and Coord. No.	$L2_1$ Model $R_{calc.}$ (Å)	R (Å)	σ^2 (Å^2)	Atom and Coord. No.	B2 Model $R_{calc.}$ (Å)	R (Å)	σ^2 (Å^2)
			Mn K-edge				
Ni1 × 8	2.595	2.549(6)	0.0127(7)	Ni1 × 8	2.615	2.567(3)	0.0115(3)
Sn1 × 3.6	2.997	2.95(2)	0.012(2)	In1 × 1.8	3.020	2.886(5)	0.0058(5)
Mn× 2.4	2.997	2.93(1)	0.008(1)	Mn× 4.2	3.020	2.911(5)	0.0108(6)
Mn1 × 12	4.239	4.21(2)	0.021(3)	Mn1 × 12	4.270	4.27(4)	0.035(7)
Ni2 × 24	4.970	4.95(2)	0.019(2)	MS[b] × 4.8	5.230	5.10(3)	0.017(4)
MS[a] × 16	5.191	5.098(3)	0.014(1)	MS[c] × 11.2	5.230	5.175(6)	0.0129(7)
			Ni K-edge				
Mn1 × 5.6	2.595	2.550(7)	0.0132(9)	Mn1 × 5.6	2.615	2.580(4)	0.0128(5)
Sn1 × 2.4	2.595	2.601(7)	0.0072(6)	In1 × 2.4	2.615	2.634(4)	0.0070(4)
Ni1 × 6	2.997	2.98(3)	0.026(5)	Ni1 × 6	3.020	3.13(6)	0.038(9)

[a] Mn→Sn3→Ni1→Mn
[b] Mn→In3→Ni1→Mn
[c] Mn→Sn3→Ni1→Mn

It is interesting to note that bond lengths obtained are different for Ni-Mn and Ni-Sn bonds. In the cubic $L2_1$ structure, the Y-site(Mn) and Z-site(Sn) atoms form two interlocking tetrahedral cages with X-site(Ni) at the centre. Therefore Mn and Sn should be equidistant from Ni. The difference in the Ni-Mn and Ni-Sn bond lengths conclusively point towards structural disorder in the cubic phase that was anticipated from the Mn K-edge analysis.

Moreover, the Ni-Sn and Ni-Ni bond lengths match closely with the values calculated from the room temperature diffraction data, while a smaller value is obtained for Ni-Mn bond. The Ni-Mn bond length obtained from both, Mn and Ni EXAFS is actually the weighted average distance of Ni from the Y-Mn and the Z-Mn. Ideally, for a $L2_1$ structure, both these contributions should have been identical and equal to the Ni-Sn bond distance. A possible explanation for the discrepancy in the Ni-Mn bond length can be that the two contributions are not equal. That is, there is a slight difference in the bond distance of Y-Mn and the Z-Mn from Ni giving an average Ni-Mn distance shorter than that expected. In order to confirm this, Mn EXAFS data was fitted again with the δr's and σ^2 varied independently for each path. The final fitted parameters are listed in Table 6.2 and the magnitude and real component of EXAFS data and the fit are presented in Fig. 6.6. It can be clearly seen that the distances obtained from Mn EXAFS analysis are lower than the distances calculated from the diffraction data. Hence there exists a disorder in the position of Mn atoms even in the cubic $L2_1$ structure.

The cubic model described in the preceding paragraph was also used to fit In60 data collected at room temperature. Slight changes were incorporated in the model to accommodate the effects due to disorder in the occupancy of Y and Z site. For this, the coordination numbers of the second scattering path comprising of Mn and In were suitably altered. A good fit was obtained for the values of the parameters included in Table 6.2. The corresponding fittings are shown in Fig. 6.7. The values obtained from Mn edge indicate that for the second correlation, Mn-In bond distance at ~ 2.88Å is slightly different from the Mn-Mn bond distance. This difference in the Mn-In/Mn-Mn bond is reflected in the corresponding multiple

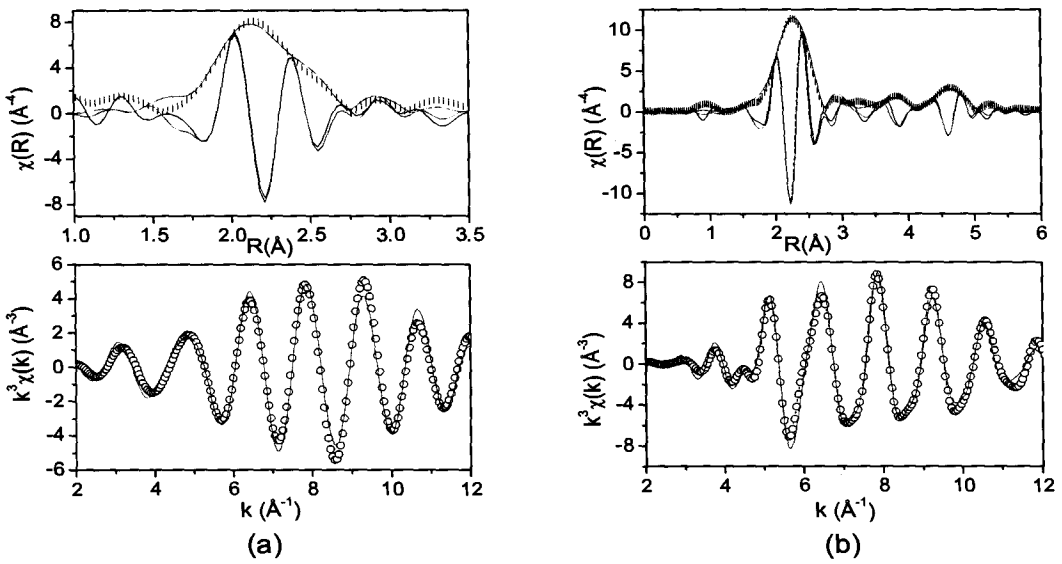

Figure 6.6: Magnitude and real component of FT of EXAFS spectra in R space and real component of FT in the back transformed k space for (a) Ni K-edge and (b) Mn K-edge in $Ni_{50}Mn_{35}Sn_{15}$ obtained at room temperature. The fitting to the data are shown as coloured lines.

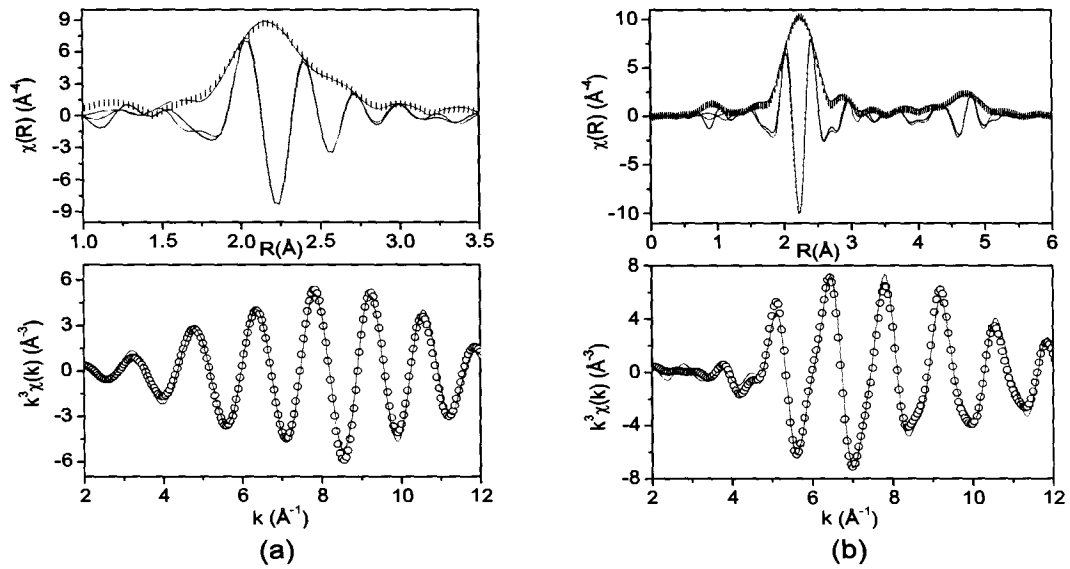

Figure 6.7: Magnitude and real component of FT of EXAFS spectra in R space and real component of FT in the back transformed k space for (a) Ni K-edge and (b) Mn K-edge in $Ni_{50}Mn_{35}In_{15}$ obtained at room temperature. The fitting to the data are shown as coloured lines.

scattering paths too. Moreover, the third correlation at 4.27Å comprising of yet another Mn-Mn bond has an exceptionally large σ^2 value. Such an anomaly indicates considerable movement of the Mn atoms in comparison to the other constituents of the alloy. Also, the unequal Mn-Ni bond lengths from Ni and Mn K-edge hints towards the fact that Mn atoms are indeed moving. Ni edge analysis also provide some interesting observations. The striking observation here is the difference in the Ni-Mn and Ni-In bond distance obtained from the Ni K-edge analysis. Similar observation was made from Ni K-edge analysis of Sn60 where such a difference was claimed to be the outcome of structural disorder in the cubic phase. However, difference in the Ni-Mn and Ni-In bond distance in In60 might be an outcome of not only structural disorder but also martensitic transformation. It may be noted that the martensitic transformation temperature of In60 ($T_M \sim 290$ K) is in close proximity to the temperature of EXAFS measurement (295 K). The pre-transformational effects get very intense as T_M is approached and any measurement in the narrow region of temperature around T_M are known to be affected. Such deficiency has also been observed for the EXAFS analysis of $Ni_{2.1}Mn_{0.89}Ga$ that has a $T_M \sim 285$ K. Thus the signatures related to structural transformation are expected to be very prominent in In60.

The martensitic transformation being in the vicinity of 200 K for Sn60, EXAFS measured at liquid nitrogen temperature ($\sim$ 77 K) contains no residual cubic component and was used to determine the local structure of the martensitic phase. The structural model for this low temperature phase was developed using an orthorhombic cell with *Pmma* space group and lattice parameters reported by Brown *et.al.* [8]. However, with Mn as the central atom, this structural model gives several closely spaced Mn-Ni, Mn-Sn and Mn-Mn bonds. EXAFS is

generally insensitive in resolving such scattering paths. Therefore, while fitting, these closely spaced scattering paths were grouped into one or two correlations. The coordination number for the Mn-[Sn/Mn] path was maintained in accordance with the composition ratio of Mn and Sn. The δrs' and σ^2s' for each of the scattering paths were varied independently without any constraint. Similar fitting procedure was also followed in case of Ni EXAFS. The values given in Table 6.3 were found to give a good fit to the experimental spectra as can be seen from Fig. 6.8. While an increase of 0.02Å is seen in the Mn-Ni bond distance, the first Mn-Sn and Mn-Mn distances shorten to 2.87Å from those obtained in the austenitic phase of Sn60. Likewise, the parameters obtained from the analysis of low temperature Ni EXAFS (refer Table 6.3) show that the Ni-Mn distance indeed increases and is in good agreement with the value obtained from Mn EXAFS. The most significant observation here is that the Ni-Sn distance remains unchanged from its room temperature value. This implies that the low temperature modulated structure is due to an unequal movement of constituent atoms with Mn moving with a largest amplitude.

The local structure of the martensitic phase of In60 was determined using the structural model similar to that of Sn60 with essential modification in the coordination numbers of the second scattering paths. The bond distances and σ^2 values obtained are included in Table 6.3 and the fitted spectra are shown in Fig. 6.9. The Mn-Ni bond distance remains unchanged from its room temperature value. While a decrease of 0.02Å is observed in the Ni-Mn bond, the Ni-In bond increases by almost 0.07Å. This implies that the Ni-Mn bonds grow stronger at the cost of Ni-In bonds. Furthermore, the comparison of the parameters for the two samples, Sn60 and In60, shows a difference of 0.02 Å between the Mn-Mn* bonds

Table 6.3: Parameters for the martensitic phase of $Ni_{50}Mn_{35}Sn_{15}$ and $Ni_{50}Mn_{35}In_{15}$ determined from the analysis of Mn and Ni K-edge EXAFS recorded at low temperature. The fittings were carried out in k range: (2- 12)Å^{-1} with k-weight: 3 and R range: (1-5)Å for Mn edge and (1-3)Å for Ni edge. Figures in parentheses indicate uncertainty in the last digit.

	Sn60			In60	
Atom and Coord. No.	R (Å)	σ^2 (Å^2)	Atom and Coord. No.	R (Å)	σ^2 (Å^2)
			Mn K-edge		
Ni1 × 8	2.568(1)	0.0077(1)	Ni1 × 8	2.568(3)	0.0079(3)
Sn1 × 3.6	2.873(3)	0.0069(3)	In1 × 1.8	2.879(6)	0.0046(6)
Mn* × 2.4	2.877(4)	0.0095(5)	Mn* × 4.2	2.896(6)	0.0094(7)
Mn1 × 8	4.17(2)	0.023(3)	Mn1 × 8	4.19(1)	0.016(2)
Mn2 × 4	4.291(9)	0.008(1)	Mn2 × 4	4.40(2)	0.012(2)
Ni2 × 8	4.753(6)	0.0088(7)	Ni2 × 8	4.736(7)	0.009(8)
Ni3 × 16	4.940(3)	0.0086(3)	Ni3 × 16	4.918(8)	0.0080(9)
			Ni K-edge		
Mn1 × 5.6	2.569(2)	0.0092(2)	Mn1 × 5.6	2.558(3)	0.0068(4)
Sn1 × 2.4	2.607(1)	0.0035(1)	In1 × 2.4	2.70(1)	0.009(1)
Ni1 × 2	2.83(1)	0.016(2)	Ni1 × 2	2.797(7)	0.0038(8)
Ni2 × 4	3.15(3)	0.027(5)	Ni2 × 4	3.13(8)	0.027(13)

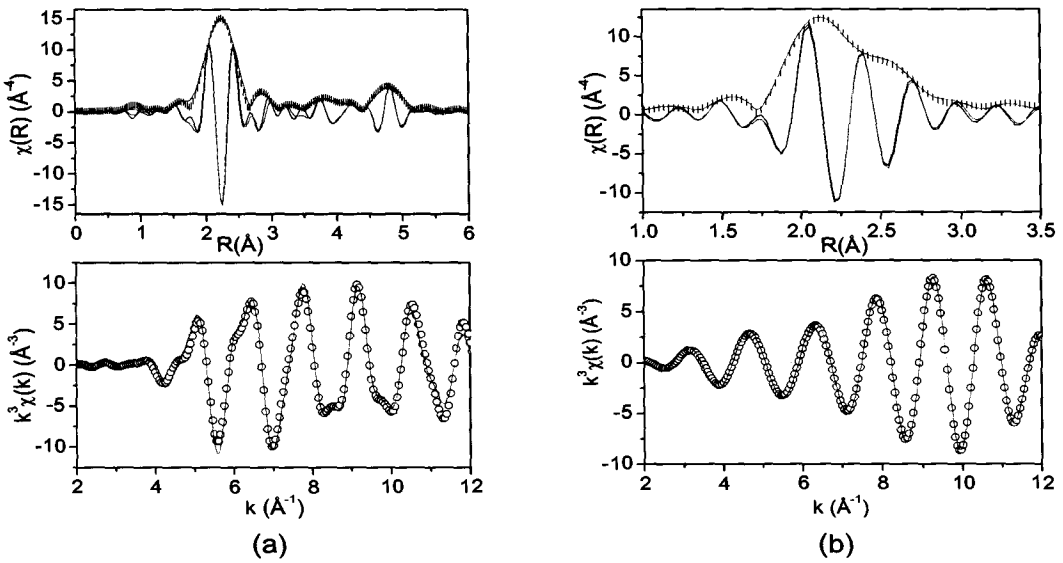

Figure 6.8: Magnitude and real component of FT of EXAFS spectra in R space and real component of FT in the back transformed k space for (a) Mn K-edge and (b) Ni K-edge in $Ni_{50}Mn_{35}Sn_{15}$ obtained at low temperature. Coloured lines represents the fit to the data.

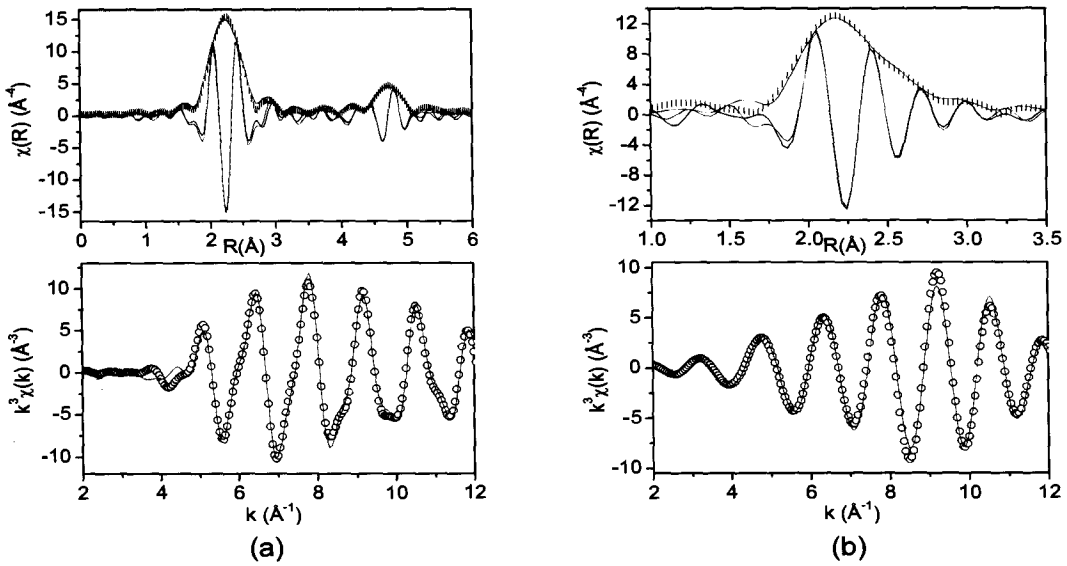

Figure 6.9: Magnitude and real component of FT of EXAFS spectra in R space and real component of FT in the back transformed k space for (a) Mn K-edge and (b) Ni K-edge in $Ni_{50}Mn_{35}In_{15}$ obtained at low temperature. Coloured lines represents the fit to the data.

of the second shell while the Mn-Mn bonds in the fourth shell differ by as much as $\sim$ 0.1 Å. The reason for this could be the structural disorder in In60 sample. The change in structure from $L2_1$ to B2 increases the number of Mn atoms occupying the Z-position in the X_2YZ Heusler structure. The increased disorder is well reflected in the XRD profile of the two alloys where In60 has much broader Bragg reflections than Sn60.

6.2.1 Discussion

EXAFS measurements in the cubic and martensitic phase of $Ni_{50}Mn_{35}Sn_{15}$ and $Ni_{50}Mn_{35}In_{15}$ bring out an important observation that influence the martensitic and magnetic interactions in these system. Essentially, these systems belong to the Ni-Mn based ternary Heusler intermetallics having generic formula X_2YZ. The stoichiometric Ni_2MnSn and Ni_2MnIn are

ferromagnets with Curie temperature $T_C \sim 360$K and 320 K respectively, and do not undergo any martensitic transformation [10]. The exchange interactions in such Heusler alloys is mainly due to the indirect RKKY interaction between Mn atoms mediated by the conduction electrons of the system [15]. As Mn concentration is increased in the system, martensitic phase transformation sets in and magnetism gets even more complex. The magnetization results reported in the previous section show that $Ni_{50}Mn_{35}Sn_{15}$ orders ferromagnetically at $T_C = 319$ K and undergoes a martensitic transformation ~ 200 K while T_C for $Ni_{50}Mn_{35}In_{15}$ is 309 K and the martensitic transition occurs around 290 K.

The important result of the room temperature EXAFS study of Sn60 is that the local distortions exist in the crystal structure within the cubic framework. These distortions reflect through a shorter Ni-Mn distance and distinctly different Ni-Sn and Ni-Mn bond lengths. The Ni-Mn distance obtained from EXAFS analysis is the average bond length of Ni-[Y-Mn] and Ni-[Z-Mn]. Since the atomic sizes of Sn and Mn are different, a local distortion can occur when excess Mn occupy the vacant Sn sites. This can lead to a shorter Ni-[Z-Mn] distance as compared to Ni-[Y-Mn] distance. This distortion in the $L2_1$ structure may probably be one of the factors that influence the martensitic transformation in $Ni_{50}Mn_{35}Sn_{15}$ which does not exist for the stoichiometric Ni_2MnSn. Further, a shorter Ni-[Z-Mn] bond implies stronger hybridization of Ni with Z-Mn. Such a hybridization is not possible in the stoichiometric Ni_2MnSn. The hybridization features between X and Z species of the X_2YZ metallic systems is known to influence the binding mechanism [16]. In the case of $Ni_{50}Mn_{35}Sn_{15}$, the stronger Ni-[Z-Mn] hybridization perhaps results in a peak in density of states at Fermi level that is absent in Ni_2MnSn, leading to a martensitic transition.

The martensitic phase change in shape memory alloys is a volume conserving transformation. Therefore the weighted averages of all bond distances obtained from EXAFS analysis in the martensitic phase should be nearly equal to those obtained in the austenitic phase. Indeed this is observed for all distances except for Mn-Sn and Mn-Mn bonds in Sn60 whose lengths shorten from 2.95Å to 2.87Å. This indicates that the observed modulated low temperature phase in Sn60 is mainly due to the movement of Mn atoms. The movement of Mn atoms implies that there is a redistribution of Ni-[Y-Mn] and Ni-[Z-Mn] bond distances that give an average Ni-Mn value that is different from that in the cubic phase. Such redistribution results in a scenario wherein the tetrahedral cage of Ni-[Y-Mn] expands giving room for the Ni-[Z-Mn] tetrahedron to shrink and form stronger hybrid states. This situation is analogous to that observed in $Ni_{2+x}Mn_{1-x}Ga$ alloys in the preceding Chapter. Here, upon undergoing martensitic transition, the Mn atoms occupying the Y-site move away from Ni while the Ga atoms that occupy the Z-site form stronger bonds with Ni. A picture obtained from analysis of In60 is no different. The anomalies observed in the room temperature EXAFS analysis of In60 are a clear manifestation of its martensitic transformation that lies just 5 K below above the temperature of EXAFS measurement. The unusually large σ^2 for the Mn-Mn bond and the distinctly different Ni-Mn, Mn-Ni bonds indicate the movement of Mn atoms from its crystallographic site that leads to modulations. The larger difference in Ni-Mn and Ni-In bond distances is also an indication of movement of Mn. Furthermore, here the structure being B2, there is a complete disorder in the positions of Mn and In. This results in a stronger Ni-Mn interaction than in case of Sn60. This is perhaps the reason for higher T_M in In60 inspite of it having a lower c/a ratio as compared to Sn60. The values

obtained at low temperature further strengthen the fact that the Mn atoms indeed move to come closer to Ni while the In atoms are pushed away providing space for Mn atoms to form strong hybridization with Ni.

Band structure calculations for X_2MnZ Heusler system [15] have shown that the spin-up *3d* states of Mn are fully occupied and hybridized with the *d* states of the X atoms, whereas the spin down *d* states are nearly empty and are almost completely excluded from the Mn site. This results in a localized magnetic moment of Mn. The Z atoms provide *p* electrons to form hybrid states with *d* electrons of transition metals and through their valence also determine the degree of occupation of hybrid *pd* orbitals. In the case of Ni_2MnGa, Zayak *et.al* [16] have shown that due to presence of large local magnetic moment of Mn, spin down *3d* electrons of Ni do not find symmetry allowed *d* states of Mn to hybridize with. This results in a electrostatic like repulsion between Mn and Ni atoms and leads to a attractive interaction between spin down *3d* electrons of Ni and *4p* electrons of Ga. Such *pd* hybridization gives rise to a peak in the density of states that is believed to be responsible for martensitic transformation in this alloy. In $Ni_{50}Mn_{35}Sn_{15}$ and $Ni_{50}Mn_{35}In_{15}$, our EXAFS study gives lower average Ni-Mn distances as compared to calculated ones in the austenitic as well as martensitic phase. The ordered $L2_1$ structure implies that the lower average Ni-Mn distance results from shorter Ni-[Z-Mn] bond. The *dd* hybridization that results from this shorter Ni-[Z-Mn] distance may lead to Jahn-Teller distortions that lower the total moment of Mn atoms. Lower Mn moments have also been obtained by Brown *et.al* [8] from neutron diffraction studies. The symmetry change upon martensitic transition further adds to this effect resulting in a total magnetization that is almost half its value in the austenitic phase.

Whereas in $Ni_{50}Mn_{35}In_{15}$, though the identification of Mn as Y-Mn or Z-Mn is not possible, the fact that there exists some *dd* hybridization is clear from the shorter Ni-Mn and longer Ni-In bonds. The structural disorder in the occupation of Y and Z sites also affects the magnetization in martensitic phase of $Ni_{50}Mn_{35}In_{15}$.

6.3 Results: $Ni_{50}Mn_{35}Sn_{15-x}In_x$ (x = 3.75, 7.5, 11.25)

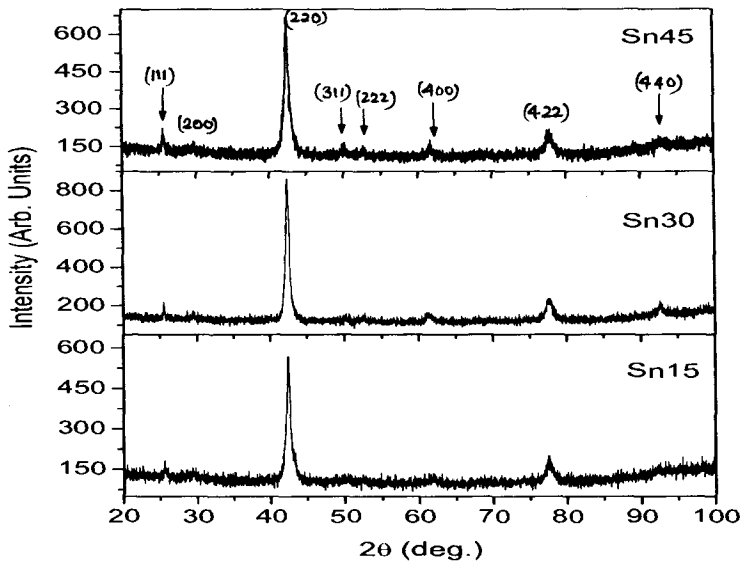

Figure 6.10: Room temperature X-ray powder diffraction pattern of $Ni_{50}Mn_{35}Sn_{11.25}In_{3.75}$ (Sn45), $Ni_{50}Mn_{35}Sn_{7.5}In_{7.5}$ (Sn30) and $Ni_{50}Mn_{35}Sn_{3.75}In_{11.25}$ (Sn15).

The room temperature XRD profiles for Sn45, Sn30 and Sn15 samples are shown in Fig. 6.10. It is clear from the positions of the high intensity peaks that the samples are mainly ordered in the B2 structure. Broad peak widths indicate that the underlying lattice might be strained. At the same time, small amount of structural order might be present with a $L2_1$ component, which is established through superlattice reflections. Such a $L2_1$ component is present in the Sn45 sample as evident from its XRD profile. The patterns for Sn30, Sn15

samples might also contain the $L2_1$ signatures but the superlattice peak intensities being very low may be considered to be small. The broad peak widths also suggest that some sort of modulation within the cubic frame work might be present. For this, it is important to have some estimate of the T_Ms for these alloys.

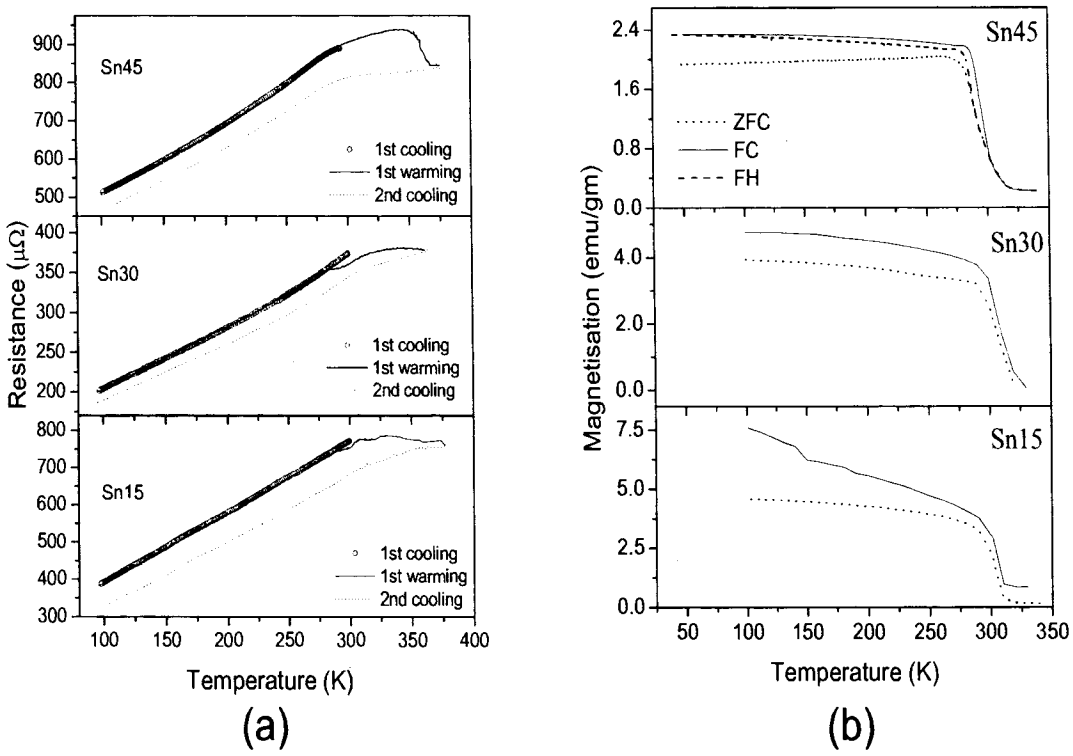

Figure 6.11: (a) Resistivity as a function of temperature measured in the range 77 K to 375 K in the warming/cooling cycles. (b) Magnetization as a function of temperature measured in a field of 50 Oe over the temperature range 50 - 350 K.

Thus, four probe resistance as a function of temperature was measured for Sn45, Sn30 and Sn15 samples. Measurements were carried out while cooling the sample from room temperature to 77 K and then warming upto 375 K followed by cooling back to 77 K. It may be noted that normally change in slope of resistivity (flattening) indicates magnetic transition

while a sharp jump or peak like structure is a signature of martensitic transformation. The resistivity plots for the present samples are presented in Fig. 6.11(a). It is clear from the plots that hysteresis between warming/cooling data extends over the entire range of temperature of measurement. The resistance profile during second cooling runs parallel to the first cooling curve with an overall magnitude lower to that of first cooling. The curves of first warming and subsequent cooling are well separated. The most striking feature is the considerable change of slope alongwith a hump-like feature observed in warming cycle of every sample. This broad hump is spread between 280 K to 350 K. Such a behaviour hints towards martensitic transformation being coupled to, or, in close vicinity to, the magnetic ordering temperature and both these transformations occurring in a broad range of temperature centered around RT.

Magnetization studies further support the inference drawn from the resistivity measurements. The FC and FH curves for the three samples determined in a field of 50 Oe over the temperature range 50 - 350 K are shown in Fig. 6.11(b). The step-like sudden rise in M(T) with decreasing temperature is a signature of magnetic ordering, while the hysteresis in FC and FH curves is an evidence for structural transformation. The plots seen in Fig. 6.11(b) indicate that the sudden rise in M(T) is followed immediately by a large separation of FC and FH curves suggest that the difference in martensitic and magnetic transition temperatures is very small. Further, it is seen that in Sn30 and Sn15, the M(T) keeps rising as the temperature is lowered indicating considerable magnetic inhomogeneity in these alloys.

The EXAFS recorded at Mn and Ni K-edges for these samples should provide an insight to the martensitic transformation mechanism and possible explanation for the magnetic be-

haviour. Trends in resistivity, magnetization and room temperature XRD profiles indicate that all the three alloys are unstable at room temperature. Therefore the XAFS data collected here can contain multiple contributions from the evolving magnetic and martensitic subsystems. To obtain a clear and useful information the data recorded at low temperature was used for the analysis. The crystal structure similar to that used for the analysis of low temperature In60 was employed to model the low temperature data of all the three samples. The bond distances and the corresponding σ^2 values are listed in Table. 6.4, while the fittings are presented at Fig. 6.12.

Table 6.4: Results of the fits to the low temperature Mn and Ni K-edge data of $x = 3.75$, 7.5 and 11.25. The fittings were carried out in k range: (2- 12)Å^{-1} with k-weight: 3 and R range: (1-5)Å for Mn edge and (1-3)Å for Ni edge. Figures in parentheses indicate uncertainty in the last digit.

	Sn45		Sn30		Sn15	
Atom and Coord. No.	R (Å)	σ^2 (Å^2)	R (Å)	σ^2 (Å^2)	R (Å)	σ^2 (Å^2)
			Mn K-edge			
Ni1 × 8	2.596(3)	0.0129(4)	2.573(3)	0.0106(4)	2.565(3)	0.0105(4)
Sn/In1 × 1.8	2.925(5)	0.0079(6)	2.91(1)	0.012(3)	2.93(4)	0.011(4)
Mn* × 4.2	2.951(4)	0.0104(6)	2.904(7)	0.006(2)	2.92(3)	0.008(4)
Mn1 × 8	4.09(3)	0.019(4)	4.20(2)	0.014(2)	4.14(3)	0.020(4)
Mn2 × 4	4.46(6)	0.017(8)	4.46(4)	0.015(5)	4.31(9)	0.020(12)
Ni2 × 8	4.80(2)	0.011(2)	4.73(1)	0.011(1)	4.74(1)	0.008(1)
Ni3 × 16	5.02(3)	0.010(3)	4.921(5)	0.0092(6)	4.910(6)	0.0079(6)
			Ni K-edge			
Mn1 × 5.6	2.566(2)	0.0075(2)	2.553(3)	0.0082(4)	2.555(2)	0.0059(2)
Sn/In1 × 2.4	2.620(6)	0.0099(7)	2.648(3)	0.0041(3)	2.635(7)	0.0090(7)
Ni1 × 2	2.815(6)	0.0072(6)	2.788(9)	0.008(1)	2.785(5)	0.0053(6)
Ni2 × 4	3.04(1)	0.016(1)	3.032(9)	0.012(1)	3.00(2)	0.171(2)

For each of the samples analysed, it is seen that the Mn-Ni bond distance is much different than the Ni-Mn bond distance. The corresponding σ^2 obtained from the Mn edge analysis are also higher than those obtained from Ni edge. As the same pair of atoms is involved, such discrepancy points towards structural modulation that results from unequal

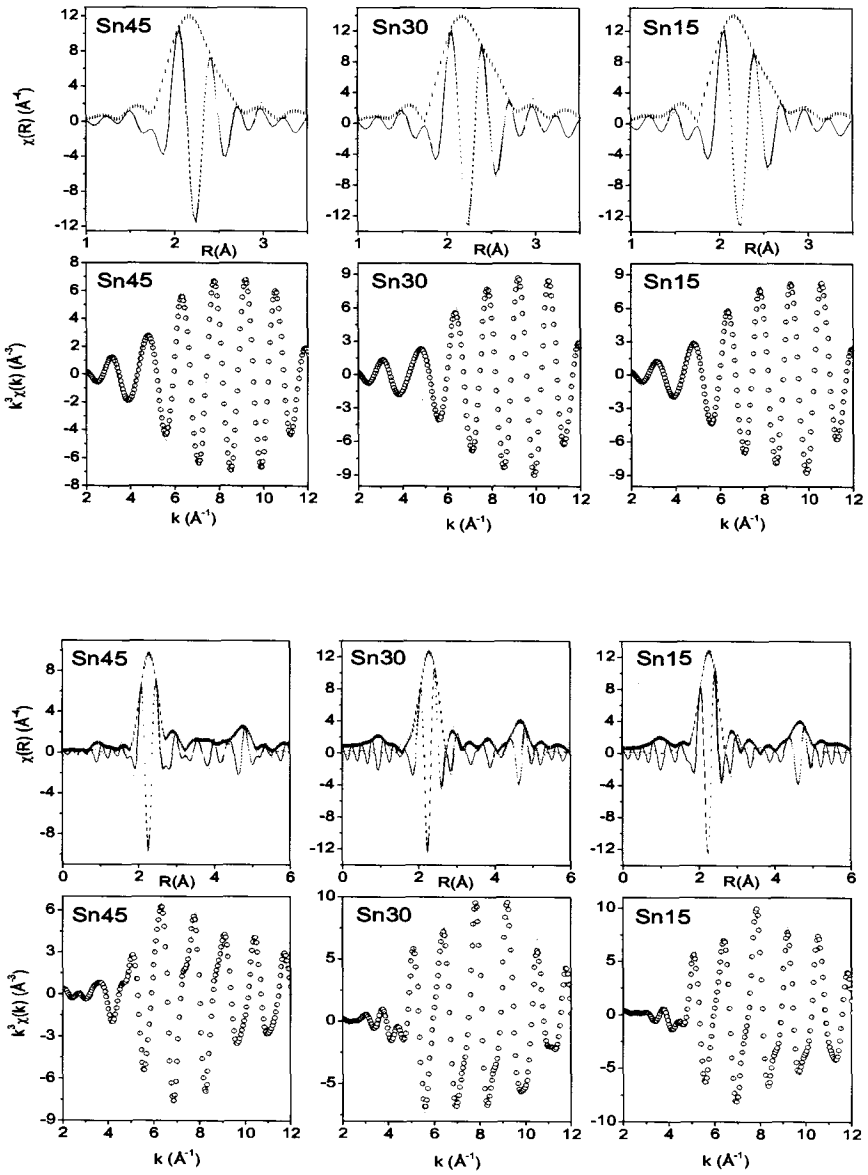

Figure 6.12: Magnitude and real component of FT of EXAFS spectra in R space and real component of FT in the back transformed k space for Ni K-edge in Sn45, Sn30 and Sn15 at low temperature. Coloured lines represents the fit to the data.

movement of constituent atoms forming the alloy. Moreover, the σ^2 obtained from Mn edge being large, it can be assumed that it is the Mn atoms that move with larger amplitude. Such structural modulations are present even in the case of In60. These modulations are perhaps responsible for the hysteresis seen in magnetization and resistivity measurements even at low temperatures. In In60 this hysteresis has been attributed to multiple martensitic transformations [13]. On comparing the values of bond distances and the corresponding σ^2 across the series, it is seen that as In concentration increases at the cost of Sn, the Ni-[Sn1/In1] bond increases systematically from 2.60Å in Sn60 to 2.70Å in In60. Furthermore it is also seen that Mn-Mn* and Mn-In/Sn distance in these three compounds are much longer that those in Sn60 or In60. The Mn-Mn* distance is very important with respect to magnetism of these alloys. It is known to give rise to some antiparallel alignment that reduces the Mn moment in these alloys. The larger Mn-Mn* distance could be the cause of changed magnetization behaviour in these compounds.

6.3.1 Discussion

The mixed series studied here present an opportunity to understand the martensitic and magnetic aspects in such Ni-Mn based alloys. It is seen from the resistivity and magnetization studies that these systems are highly unstable at temperatures close to RT. The magnetic and martensitic transition are expected in the broad range of temperature varying from 280 K to 350 K. The two phase transformations are either coupled or occur at very small temperature difference. It is difficult to say which one precedes the other. This feature is clearly brought out by the anomalous behaviour seen in every method of characterization employed.

From the local structural studies carried out on these mixed alloys, it is clear that there is a considerable movement of Mn atoms in comparison to the other constituents of the alloy. The uneven Mn-Ni/Ni-Mn bonds and the large σ^2 obtained for Mn edge for all the three samples are a clear indication of such a movement. The end members of this series, viz. Sn60 and In60 also show signatures of movement of Mn atoms. It has already known that such movement of constituent atoms is the cause for modulation in the structure [14]. A drastic affect of such modulations is seen on the transport properties of the alloys. The observed large hysteresis in resistivity can result from the conduction electrons being trapped in differently nested Fermi surfaces resulting from modulations. It is seen that the hysteresis in these alloys do not vanish even at temperatures much lower than T_M and the data during warming cycles and cooling cycles are well separated. This could to due to the fact that during the initial cooling that starts at RT, the system is unstable towards phase transformation. The subsequent warmup that extends to temperatures above 350 K drives the system to a stable state and cooling the system from this stage results in modulated structures different from those attained during initial cooling.

The anomalies seen in the magnetic subsystem and its relation with the martensitic structure can also be explained through EXAFS studies. We recall the EXAFS study of Ni-Mn-Ga wherein, the Ni-Ga bonds in the martensitic phase strengthen giving rise to a peak at E_F in the spin down density of states that drives the system to phase transition. Likewise, in the martensitic phase of Ni-Mn-Sn-In alloys, the Ni-Mn bonds shorten while the Ni-[In/Sn] bonds are stretched apart. Even-though these systems have excess Mn atoms occupying the Y and Z-sites, it is clear from the EXAFS study of Sn60 that it is the Mn atom

at Z site that hybridizes strongly with Ni giving rise to *dd* hybridization. The tetrahedral atomic cage enclosing Ni gets distorted leading to Jahn-Teller distortions that lower the total moment of Mn atoms. Also, magnetism in Heusler alloys is essentially confined to the Mn sublattice with the magnetic short-range X-Mn interaction being equally important for systems with sizeable magnetic moments on the X atoms such as Co and Ni [15, 17]. The *dd* hybridization that results from the shorter Ni-[Z-Mn] may further enhance the band Jahn-Teller distortions affecting the magnetic subsystem. The magnetic ordering here being RKKY type, the conduction electron density of states is quite important. The conduction electrons available for magnetic interactions may also get affected by the *dd* hybridization due to their trapping in the nesting part of the Fermi surface. The outcome of which is the unsaturated moments even at low temperatures seen in the mixed alloy systems.

6.4 Conclusions

The EXAFS studies in one more Ni-Mn based Heulser alloy series were carried out. The study unequivocally proves that the factor influencing the martensitic transformation is the hybridization between the X-Z species of the X_2YZ system.

In particular, the magnetism and martensitic transformation in $Ni_{50}Mn_{35}Sn_{15-x}In_{15}$ was understood. The martensitic transformation here results from an interaction between Ni and the excess Mn doped for Sn/In. This fact is very clear from (a) the shorter Ni-Mn bond distances as compared to Ni-Sn/In and (b) the absence of martensitic transformation in the stoichiometric Ni_2MnSn or Ni_2MnIn alloys. While the martensitic transformation here results from the Ni-Mn hybridization, the magnetic subsystem which is essentially confined to Mn sublattice also gets affected.

References

[1] A. N. Vasil'ev, V. D. Buchel'nikov, T. Takagi, V. V.Kholvailo and E. I. Estrin, *Phys-Usp.*, **46**, 559 (2003) and *Usp. Fiz. Nauk*, **173**, 577 (2003).

[2] O. Soderberg, Y. Ge, A. Sozinov, S-P. Hannula and V. K. Lindroos, Smart. Mater. Struct. **14**, S223 (2005).

[3] P. Entel, V. D. Buchelnikov, V. V. Khovailo, A. T. Zayak, W. A. Adeagdo, M. E. Gruner, H. C. Herper and E. F. Wassermann, J. Phys. D: Appl. Phys. **39**, 865 (2006).

[4] L. Pareti, M. Solzi, F. Albertini and A. Paoluzi, Eur. Phys. J. B. **32**, 303-307 (2003).

[5] Y. Sutou, Y. Imano, N. Koeda, T. Omori, R. Kainuma, K. Ishida and K. Oikawa, Appl. Phys. Lett. **85**, 4358-4360 (2004).

[6] T. Krenke, E. Duman, M. Acet, E. Wassermann, X. Moya, L. Manosa and A. Planes, Nat. Mater. **4**, 450 (2005).

[7] S. Y. Yu, Z. H. Liu, G. D. Liu, J. L. Chen, Z. X. Cao, G. H. Wu, B. Zhang and X. X. Zhang, Appl. Phys. Lett. **89**, 162503 (2006).

[8] P. J. Brown, A. P. Grandy, K. Ishida, R. Kainuma, T. Kanomata, K-U. Neumann, K. Oikawa, B. Ouladdiaf and K. R. A. Ziebeck, J. Phys.:Condens. Mater. **18**, 2249-2259 (2006).

[9] K. Koyama, K. Watanabe, T. Kanomata, R. Kainuma, K Oikawa and K Ishida, Appl. Phys. Lett. **88**, 132505 (2006).

[10] P. J. Webster and K. R. A. Ziebeck in *Alloys and Compounds of d-Elements with Main Group Elements*, Part 2, edited by H. R. J. Wijn, Landolt-Börnstein, New Series, Group III, **19/c**, Springer, Berlin, (1988).

[11] T. Krenke, M. Acet, E. Wassermann, X. Moya, L. Manosa and A. Planes, Phys. Rev. B **72**, 014412 (2005).

[12] F. Gejima, Y. Sutou, R. Kainuma and K. Ishida, Mater. Trans. A. **30**, 2721 (1999).

[13] T. Krenke, M. Acet, E. Wassermann, X. Moya, L. Manosa and A. Planes, Phys. Rev. B **73**, 174413 (2006).

[14] P. A. Bhobe, K. R. Priolkar, P. R. Sarode, Phys. Rev. B **78**, 224425 (2006).

[15] J. Klüber, A. R. Williams and C. B. Sommers, Phys. Rev. B **28**, 1745 (1983).

[16] A. T. Zayak, P. Entel, K. M. Rabe, W. A. Adeagbo, and M. Acet, Phys. Rev. B **72**, 054113 (2005)

[17] P. J. Webster, J. Phys. Chem. Solids **32**, 1221 (1971).

Chapter 7

Summary and Conclusions

This thesis describes in detail the structural analysis of the two alloys series: $Ni_{2+x}Mn_{1-x}Ga$ and $Ni_{50}Mn_{35}Sn_{15-x}In_x$, through their magnetic and martensitic transitions using X-ray Absorption Fine Structure (XAFS) as the major technique. This work presents new evidence for the crucial hybridization component that influences and leads to structural transitions in these Ni-Mn based Heusler alloys.

In this Chapter, the results of the entire investigation carried out on $Ni_{2+x}Mn_{1-x}Ga$ and $Ni_{50}Mn_{35}Sn_{15-x}In_x$ and its implications to our understanding of the phenomenon of "Martensitic Transition" in Ni-Mn based Heusler alloys are summarized. The role XAFS measurements can play in further understanding martensitic transitions in other materials is also discussed. In conclusion, the possibility of advancement of the work presented and scope for future work are mentioned.

7.1 Implications of this work

Ni_2MnGa undergoes martensitic transition in the ferromagnetic state with $T_M \approx 220$ K and $T_C \approx 380$ K. Increasing Ni content in $Ni_{2+x}Mn_{1-x}Ga$, raises the T_M and lowers the T_C until they coincide in the narrow range of $x = 0.18$ - 0.27. With further increase in x, T_M increases

sharply while T_C continues to decrease at a much smaller rate. In the austenitic phase, all the samples show a $L2_1$ cubic structure. While in the martensitic phase depending upon the composition, differently modulated intermediate structures viz. *5M, 7M, NM-tetragonal* are obtained. The lattice distortion upon structural transformation leads to a redistribution of the electrons in the bands at the Fermi level. We have studied this change in density of states (DOS) at the Fermi level of the $Ni_{2+x}Mn_{1-x}Ga$ ($0 \leq x \leq 0.19$) alloys employing the temperature dependent Thermoelectric power (TEP) and XANES studies. Theoretical calculations indicated the stability of martensitic phase to be due to modulated structure and the shuffling of atomic planes that gives rise to wave-like pattern of atomic displacements. It was anticipated that the structural transformation is governed by the formation of a dip in the minority-spin DOS at the Fermi level, resulting from the hybrid states of Ni *d* and Ga *p* minority-spin orbitals. Therefore a precise knowledge of the changes occurring in the local structure of constituent atoms was fundamental in understanding the mechanism involved in martensitic transformation. EXAFS was thus employed to study this mechanism by making a comparative study of the local structure in austenitic and martensitic phases of $Ni_{2+x}Mn_{1-x}Ga$ alloys.

While our results clearly demonstrate the presence of local distortions in the martensitic phase of $Ni_{2+x}Mn_{1-x}Ga$ and explain the hybridization feature that leads to the martensitic transition in these alloys, it becomes mandatory to examine the applicability of this results to other Ni-Mn based Heusler FSMAs. Towards this goal, we investigated the alloy series $Ni_{50}Mn_{35}Sn_{15-x}In_x$ for the origin of the martensitic transformation. The key question addressed was, whether the hybridization component identified through the XAFS study of

Ni-Mn-Ga, also responsible for the martensitic transition in Ni-Mn-Sn-In series? The Mn content in this series being 40% higher than the stoichiometric Heusler ratio, the crystal structure of the austenitic phase is not always same as $Ni_{2+x}Mn_{1-x}Ga$ alloys. The disorder in site occupancy by different atomic species forming the alloy results in crystal structures different from the basic $L2_1$. However, aging or repeated annealing at lower temperatures might eventually cause the crystal to order in the $L2_1$ fashion. Magnetism of this series is also very intriguing with the intermediate alloy compositions having T_M coupled to T_C. It was also important to consider this aspect and understand the influence of magnetic ordering on the hybridization features dominant at E_F.

Based on the XAFS analysis that maps the transition region of Ni-Mn based Heusler systems, it was found that the transition mechanism is strengthened by the hybridization component between the X-Z species of the Heusler composition, X_2YZ. This hybridization feature influences its magnetic ordering as well. The next two paragraphs summarize the results obtained for the two systems studied here.

Ni-Mn-Ga system:

From the various techniques like XRD, SEM, optical microscopy, four probe resistivity, a.c. susceptibility, employed for the characterization of the $Ni_{2+x}Mn_{1-x}Ga$ with $0 \leq x \leq 0.19$, the signatures of premartensitic, martensitic and intermartensitic transitions are quite evident. The martensitic crystal structure is found to be modulated with lattice parameters $c/a < 1$ for compositions with $x \leq 0.1$ and $c/a > 1$ for $0.1 < x \leq 0.16$ and non-modulated for $x = 0.19$. The hysteresis observed in the warming /cooling cycles of transport measurements signifies the nesting of conduction electrons in the changing Fermi surface associated with

increasing Ni content. Thermoelectric power measurements reflects the signature of band Jahn Teller effect that exhibits through the shifting of a peak in density of states at Fermi level closer to E_F upon undergoing martensitic transition. The deviation in the behaviour of TEP from that expected for a typical Heusler alloy in the martensitic phase can be related to the differently modulated crystal structures formed upon phase transformation. The inference drawn from the XANES plots is in agreement with the results obtained from TEP.

Lastly, the comparative analysis of changing local structures in $Ni_{2+x}Mn_{1-x}Ga$ alloys upon undergoing MT reflect an important aspect that leads to such a structural change in these alloys. The most significant feature of our analysis is the Ga-Ni hybridization that strengthens in comparison to the Mn-Ni hybridization, in the martensitic phase. The local tetrahedral cages of Ga and Mn atoms that envelop the Ni atoms, get distorted due to relative increase in the Mn-Ni bonds. The transition to martensitic phase is thus due to a distortion of the local tetrahedral units within the $L1_0$ sub-cell that forms a part of the larger $L2_1$ cell. The stronger hybridization component between Ga-Ni that results from such a distortion leads to a peak in the minority spin DOS at the Fermi level E_F, that has been anticipated theoretically. In other words, all this leads to a re-distribution of electrons causing a band Jahn-Teller effect. It is also seen that the constituent atoms of Ni-Mn-Ga system displace from their crystallographic positions by varying amplitudes in the martensitic phase with Ga atoms being displaced the least. The uneven movement of the constituent atoms gives rise to dimpling of atomic planes and eventually lead to modulated structures. While, the observed coupling of magnetic and martensitic transitions in $Ni_{2.19}Mn_{0.81}Ga$ can be related to the equal strength of the Ni-Mn and Ni-Ga hybridization states that result from a non-

modulated martensitic structure.

Ni-Mn-Sn-In system:

Here, the alloy composition $Ni_{50}Mn_{35}Sn_{15-x}In_x$ for five different Sn/In concentrations in the range $0 \leq x \leq 15$ are studied. This alloy-series is particularly interesting in relation to structural and magnetic properties due to the presence of excess Mn as compared to basic Heusler intermetallics with generic formula X_2YZ. The room temperature XRD, magnetization, and four probe resistivity served as basic characterization techniques. $Ni_{50}Mn_{35}Sn_{15}$ alone crystallizes in a $L2_1$ structure while disorder in the Y-Z site occupancy is found in $Ni_{50}Mn_{35}In_{15}$ resulting in a B2 structure. The XRD profiles of the in-between concentrations show B2 as a major phase with some superlattice reflections corresponding to the $L2_1$ phase. Distinct signatures of martensitic and magnetic transitions can be obtained from the magnetization studies of $Ni_{50}Mn_{35}Sn_{15}$ and $Ni_{50}Mn_{35}In_{15}$. While, the magnetization and resisitivity for the mixed compositions show that the martensitic transformation is coupled to, or, in close vicinity to, the magnetic ordering temperature and both these transformations occur in a broad range of temperature centered around room temperature.

EXAFS measurements at room temperature and low temperature carried out at Mn and Ni K-edges reveal the most essential component involved in the MT and magnetic ordering in this series. The major inference can be based on the nearest neighbour distance alone, obtained from the two edges. In particular, the analysis of EXAFS data gives shorter Ni-Mn bond distance as compared to Ni-Sn/In distance in martensitic phase of all the alloy compositions. This suggests that martensitic transformation here results from an interaction between Ni and Mn. Further, with the refinement of $Ni_{50}Mn_{35}Sn_{15}$ data, it can be clearly

understood that such interaction is due to the excess Mn doped for Sn/In. This answers the absence of martensitic transformation in the stoichiometric Ni_2MnSn or Ni_2MnIn alloys where such Ni-Mn interaction does not exists. While the martensitic transformation here results from the Ni-Mn hybridization, the magnetic subsystem which is essentially confined to Mn sublattice also gets affected due to some antiparallel interactions of excess Mn atoms. The EXAFS studies unequivocally proves that the factor influencing the martensitic transformation is the hybridization between the X-Z species of the X_2YZ system.

7.2 Future work

In this concluding segment, we mention a few fields that can be pursued in relation to ferromagnetic shape memory alloys (FSMAs) and Heusler alloys in the coming years. The area of shape memory mechanism and martensitic transformations is very vast and ever growing. The commercial potential of these materials is determined and the effort has opened up new classes of ferromagnetic as well as non-magnetic alloys for exploration of shape memory mechanism. Most of the research in this field is application oriented with emphasis on material-properties like magnetic field induced strains (MIFS), giant magnetocaloric effect (MCE) and large magnetoresistance (MR). For any FSMA to exhibit such phenomena, the martensitic transformation and magnetic ordering have to occur at similar temperatures and for immediate application, both these transitions should be close to the room temperature. The design of the physical form that preserves the exotic properties of the FSMA yet comes handy for applications, is equally important. Hence the development of samples in the form of laser-ablated thin films is growing. Thin films prepared by sputtering or other methods are an increasing subject world-wide due to the possible applications for MEMS.

Also, ribbons have been under severe investigations with issues like the suitability of the matrix polymer, possible chemical reactions during the manufacturing and service, activation of the composite, etc. This is one of the challenging field that can be pursued in coming years.

Another property as regards to Mn-based Heusler alloys that makes it particularly interesting is the half-metallic ferromagnetism. These materials have unusual electronic structure where the electronic states for one spin projection have a metallic character with a non-zero density of states at the Fermi level E_F, while the states with the other spin projection demonstrate a band gap around E_F. As a result, half metals can in principle conduct a fully spin-polarized current, and therefore attract much attention due to potential applications in the field of spintronics. Better known as the half-Heusler systems, these alloys form with XYZ composition in the $C1_b$ structure. The classical examples have been PtMnSb and NiMnSb. More recently, several substances with composition X_2MnZ full-Heusler alloys and $L2_1$ crystal lattice have been proposed to be half-metals. Amongst these are the compounds of the type CoMnZ, where Z stands for Si or Ge. Such Mn-based Heusler alloys are particularly interesting because of their compatibility with existing semiconductor technology. The electronic structure of the half-metallic ferromagnets and related materials allows them to be efficiently applied as a source of spin-polarized charge carriers. The influence of the type of magnetic ordering has been predicted to affect the minority-spin electrons. In particular, to make these electrons lose their semiconducting character, while the majority-spin electrons keep to stay metallic. Thereby it is important to understand the interplay between the electronic structure of Mn and magnetic characteristics of Heusler alloys searching for relation

between the formation of the strong, almost 100% spin-polarized structure of the conduction electrons and the chemical type of the X and Z element. The ability of the XAFS technique to extract element selective information would provide opportunity to gain insight about the local structure and detect the type of hybridization that are most influencing the magnetic and electronic character of such alloys.

In the phenomenon of martensitic transformation the electronic states of the system can be easily manipulated by external parameters, making it a very promising issue of intense fundamental research. On this front, there are several leads to be expressed. With the development of newer and rapidly growing systems, many of the basic concepts are challenged. The foremost being the valence electron concentration, or the e/a ratio, the importance of which is documented by the set of rules describing the Hume-Rothery alloys. It has long been known that in Hume-Rothery alloys, the electron concentration per atom is extremely important in determining which structure is stable. In general, change in the number of valence electrons causes an alteration of the Brillouin zone boundary and can be considered as the primary driving force for the occurrence of structural instabilities in the alloys. The importance of the electronic structure has been emphasized by experiments that show the drastic reconstruction of the Fermi surface that takes place upon martensitic transformation. The significant changes in the Fermi surface results in nesting of conduction electrons and alters the physical properties of such systems. However, based on the value of e/a parameter alone, it is not possible to predict whether the system will undergo a phase transformation or not. For example, Ni_2MnGa that has an e/a value of 7.9 undergoes martensitic transformation while Ni_2MnIn with the same values of e/a is not known to

structurally transform to other phase. Moreover, we observe an empirical dependence of T_M on e/a in the Ni-Mn-Ga alloys while little or no such effect is seen on properties of Ni-Mn-Sn-In. Our work thus suggests that while electronic concentration at Fermi level in Ni-Mn based Heulser alloys is found to influence the transport properties, the changing e/a effects across the Ni-Mn-Ga series are much smaller in comparison to the X-Z hybridization component. Thus e/a parameter is of rather qualitative nature and can be useful in the development of the conceptual macroscopic view on the stability of Heusler structures.

The question whether X-Z hybridization states, responsible for martensitic transformation in Ni-Mn based Heusler alloys are system specific or not, has not been studied in the present work, and will be the subject of our future research. In this respect, ferromagnetic shape memory alloys with Heusler composition based on other transition metal species has to be developed and studied. Recently, new materials like Co-Ni-Al, Co-Ni-Ga are known to undergo martensitic transformation. The local structure study of such materials and newer Ni/Mn free FSMAs using XAFS would help in forming a holistic picture of the different hybridization effects dominant at E_F.

VITA

PERSONAL DETAILS

Name	Preeti Anand Bhobe
Date of Birth:	May 27, 1979
Place of Birth:	Panaji, Goa.
Father's name:	Anand Bhobe
Mother's name:	Amita Bhobe

EDUCATIONAL QUALIFICATION

In 1999, B.Sc.(Physics) with *Distinction*
Goa University

In 2001, M.Sc.(Physics) with *O -Grade* (Outstanding)
Goa University

Publications

- Journals:

1. Factors influencing the martensitic properties in $Ni_{50}Mn_{35}Sn_{15}$: An EXAFS Study

   P. A. Bhobe, K. R. Priolkar and P. R. Sarode

   Phys. Rev. B, (2007) *communicated.*

2. Local Atomic Structure of Martensitic $Ni_{2+x}Mn_{1-x}Ga$: An EXAFS Study

   P. A. Bhobe, K. R. Priolkar and P. R. Sarode

   Phys. Rev. B, 74, 224425, (2006).

3. Composition and temperature dependence of the thermoelectric power of

   $Ni_{2+x}Mn_{1-x}Ga$ alloys

   P A Bhobe, J H Monteiro, J C Cascalheira, S K Mendiratta, K R Priolkar and

P R Sarode

J. Phys.: Condens. Mater. 18, 10843, (2006).

4. Low Temperature Neutron Diffraction Study of MnTe

   J. B. C. Efrem D'Sa, **P. A. Bhobe**, K. R. Priolkar, A. Das, S. K. Paranjpe, R. B. Prabhu and P. R. Sarode

   J. Magn. Magn. Mater. 285, 267, (2005).

5. Resistivity and Thermopower of $Ni_{2.19}Mn_{0.81}Ga$ Alloy

   K. R. Priolkar, **P. A. Bhobe**, Shannol Sapieo Dias and Rajkumar Paudel.

   Phys. Rev. B, 70, 132408, (2004).

6. Low temperature Neutron diffraction study of MnSe

   J. B. C. Efrem D'Sa, **P. A. Bhobe**, K. R. Priolkar, A. Das, S. K. Paranjpe, R. B. Prabhu, and P. R. Sarode

   Pramana, 63, 227, (2004).

- Conference Proceedings:

1. Intermartensitic Transitions in Ni-Mn-Ga

   P. A. Bhobe, K. R. Priolkar and P. R. Sarode

   Proc. DAE Solid State Physics Symposium, Vol. 50C, 833 (2005).

2. Structural and Magnetic Phase Diagram of $MnTe_xSe_{1-x}$

   K. R. Priolkar, **P. A. Bhobe**, J. B. C. Efrem D'Sa, A. Das, P. S. R. Krishna and P. R. Sarode

   Proc. DAE Solid State Physics Symposium, Vol. 50C, 87 (2005).

3. Low temperature Neutron diffraction study of MnSe

   J. B. C. Efrem D'Sa, **P. A. Bhobe**, K. R. Priolkar, A. Das, S. K. Paranjpe, R. B. Prabhu, and P. R. Sarode

   International Conference on Neutron Scattering (CNS'04), BARC Mumbai January 2004.

4. Neutron Diffraction Study of MnTe

   J. B. C. Efrem D'Sa, **P. A. Bhobe**, K. R. Priolkar, A. Das, S. K. Paranjpe, R. B. Prabhu, and P. R. Sarode

   Proc. DAE Solid State Physics Symposium, Vol. 44, 435 (2001).

- Conference Presentations:

1. Effect of Composition on the Temperature Variation (10K-300K) of Electrical Resistivity and Magnetoresistance of Ni-Mn-Ga Shape Memory Alloys

   P. A. Bhobe, K. R. Priolkar, P. R. Sarode, S. K. Mendiratta, J. Monteiro and M. F. Carrasco

   Presented at III International Materials Symposium- Material 2005 held at University of Aveiro, Aveiro, Portugal during March 20-23, 2005.

2. Effect of excess Ni on intermartensitic transitions in Ni_2MnGa

   P. A. Bhobe, K. R. Priolkar, P. R. Sarode

   Presented at Third National Conference on Thermo Physics held in Goa, India during January 19, 2005.